

DESIGN OF CHEMICALLY TREATED ACTIVATED CARBON FIBERS FOR  
MERCURY REMOVAL AND ADVANCED MEMBRANES FOR WATER  
PURIFICATION

BY

YAXUAN YAO

DISSERTATION

Submitted in partial fulfillment of the requirements  
for the degree of Doctor of Philosophy in Materials Science and Engineering  
in the Graduate College of the  
University of Illinois at Urbana-Champaign, 2013

Urbana, Illinois

Doctoral Committee:

Professor James Economy, Chair  
Professor Jian-min (Jim) Zuo  
Associate Professor Jianjun Cheng  
Associate Professor Jian Ku Shang

## ABSTRACT

There are mainly two projects in this thesis, one is to develop chemically treated activated carbon fibers for mercury removal from power plant effluents, and the other one is to design advanced nanofiltration membranes for water purification with specific features, i.e. solvent resistance and antifouling properties.

The current technologies for mercury removal involve the use of chemically treated activated carbon powder has had limited success. These systems present practical problems in dealing with the large amount of absorbents required to insure quantitative removal of the Hg. The system we developed depends on using a chemically treated high surface area activated carbon fibers (50~600 m<sup>2</sup>/g), which provides very effective contact efficiency with the power plant effluent.

For chemical modifications of activated carbon fibers, sulfur and bromine containing groups were introduced into the carbon matrix. Generally, sulfur impregnations decrease surface area and pore volume but increase the Hg uptake capacities when compared to untreated activated carbon fibers. For our sulfur-treated samples, sulfur atoms were incorporated into the carbon matrix in the form of sulfide and sulfate. The sulfide groups appeared to be more effective for mercury removal than sulfate, which was probably because the lone pairs of sulfide groups could act as the interaction site for Hg adsorption, or at least the initial point of attachment.

Three approaches were explored for bromination; namely, 1) bromination using Br<sub>2</sub> vapor, 2) bromine deposition by an electrochemical reaction and 3) impregnation of bromine using KBr solution. Both static and dynamic tests were carried out to measure the mercury adsorption performances of these brominated samples. For the brominated

samples treated by Br<sub>2</sub> vapor and electrochemical method, they showed stable mercury adsorption performance (30% to 33% removal) up to 3 months, which showed great potential promising for commercialization. A possible mechanism for mercury adsorption, which was likely to involve the formation of oxidized mercury complexes (e.g. [HgBr]<sup>+</sup>, [HgBr<sub>2</sub>] and [HgBr<sub>4</sub>]<sup>2-</sup>), was also discussed.

Besides the chemical structures, pore properties also play an important role on mercury adsorption performance at room temperature. Usually, micropores are mainly responsible for mercury adsorption while mesopores may serve as transportation channels. However, physical adsorption capability decreases due to desorption at high temperatures.

Nanofiltration membranes can be used to separate salts and small molecules from the solution by applying a pressure. By far the most processes is dealing with aqueous solutions, however, with the emerging of membranes usage in food applications, petrochemical applications and pharmaceutical areas, the membranes suited for applications in organic media are required. To address this problem, the crosslinking of polyimide membranes is a commonly known method to prepare membranes suitable for solvent resistant nanofiltration. In this work, preparation of crosslinked membranes of P84 copolyimide asymmetric membranes using branched polyethylenimine (PEI) at different reaction temperatures was studied. The rejection sequence of CaCl<sub>2</sub> > NaCl > Na<sub>2</sub>SO<sub>4</sub> indicated a positively charged membrane surface. Additionally, the resultant membranes were very stable in dimethyl formamide (DMF), a harsh aprotic solvent. Even after soaking in DMF for 1 month, there were no significant changes in membrane performance or membrane structure.

Fouling caused by organic impurities such as proteins, humic substances and

polysaccharides is another concern for membrane processes. Polyelectrolyte multilayer (PEM) films consisting of sulfonated poly (ether ether ketone) sPEEK alternating with selected anionic layers were developed for fouling resistant properties. Two novel variables were introduced in our approach, a) the use of pressure and b) organic solvents, during the alternating physisorption of oppositely charged polyelectrolytes on porous supports through the electrostatic self-assembly. It was shown that the use of pressure and/or organic solvent systems could increase the salt rejection of the PEMs by several times while still remaining a high water flux. The PEMs also had a better antifouling property in comparison with NTR 7450, a commercial NF membrane with a sulfonated surface.

*To those I love and those who love me...*

## ACKNOWLEDGEMENTS

I would like to express my sincere thanks to my advisor, Professor James Economy. During my Ph.D. study, he not only provided guidance, inspiration, support and encouragement, but also gave me trust and freedom to carry out the research. His vision, optimistic attitude, enthusiasm and continual pursuing for scientific and industrial challenges are very beneficial for my life. It is a great experience and excellent opportunity to pursue my Ph.D. study in Professor James Economy's group.

I am so grateful to Prof. Jian-Min (Jim) Zuo, Prof. Jianjun Cheng and Prof. Jian-Ku Shang in my thesis committee for sparing their time, reading my thesis and providing comments in their busy schedule.

Deep thanks need to be given to Dr. Velpari for conducting the mercury static tests and proposing helpful suggestions during the Hg removal project. This project was funded by PPG Industries, Inc. This research would not be possible without Dr. Velpari's help and the funding from PPG Industries, Inc.

I would also like to extend my appreciation to the past and current members of Prof. Economy's group for being a friendly team and providing helpful discussions, including Dr. Zhongren Yue, Dr. Jinwen Wang, Dr. Chaoyi Ba, Dr. James L. Langer, Dr. Zeba Farheen Abdul Samada, Dr. Gordon Nangmenyi, Dr. Xuan Li, Dr. Jing Zhang, Prof. Zhen Zheng, Prof. Shouhai Zhang, Prof. Yi Zhang, Prof. Jun Qun, Samantha Elaine Bender, Jacob Lee Meyer, Weihua Zheng, Mengxi Guo and Shanshan Zhao.

I would like to express my gratitude to the business office personnel, Jay Menacher, Debbie Kluge, Judy Brewer, Michelle Malloch and Bryan Kieft for all their help through all these years.

I would like to thank Jim Mabon, Vania Petrova, Rich Haasch, and Julio Soares for the training of facilities in Frederick Seitz Materials Research Laboratory. I would also like to thank Dr. Dr. Alexander Ulanov in Metabolomics Center at University of Illinois for performing Gas Chromatography. The Scanning Tunneling Microscopy was measured under the help of Ms. Pam Martin in Prof. Joseph Lyding's research group at the University of Illinois at Urbana-Champaign. I would also like to thank Marie Keel and Rudiger Lauffhutte in the Microanalysis Laboratory in the University of Illinois for conducting the elemental analysis.

The membrane work was funded by WaterCAMPWS, a Science and Technology Center of Advanced Materials for the Purification of Water with Systems under the National Science Foundation agreement number CTS-0120978.

Lastly, I would like to thank my parents for their unconditional love, support, understanding and encouragement since I was born. They made me believe that the world was full of love and sunshine. Without them, I couldn't have accomplished the things I have today.

## TABLE OF CONTENTS

LIST OF FIGURES .....	ix
LIST OF TABLES.....	xi
CHAPTER 1 INTRODUCTION .....	1
1.1 Introduction.....	1
1.2 Design of chemically treated activated carbon fibers for mercury removal from power plant effluents.....	1
1.3 Design of advanced nanofiltration membranes for water purification and desalination .....	4
1.4 References.....	5
CHAPTER 2 DESIGN OF CHEMICALLY ACTIVATED CARBON FIBERS FOR MERCURY REMOVAL FROM POWER PLANT EFFLUENTS.....	8
2.1 Background.....	8
2.2 Design of sulfur treated activated carbon fibers (ACFs) for mercury removal.....	18
2.3 Design of brominated activated carbon fibers (ACFs) for mercury removal ....	35
2.4 Design of chemically activated carbon fibers (CAFs) for mercury removal.....	53
2.5 References.....	66
CHAPTER 3 DESIGN OF ADVANCED NANOFILTRATION MEMBRANES FOR WATER PURIFICATION AND DESALINATION .....	72
3.1 Background.....	72
3.2 Design of polyethylenimine crosslinked P84 membranes for solvent resistance.....	81
3.3 Preparation of polyelectrolyte multilayer membranes for anti-fouling properties.....	98
3.4 References.....	120
CHAPTER 4 CONCLUSIONS.....	126



## LIST OF FIGURES

Figure 2.1 Mercury cycle .....	9
Figure 2.2 Sources of mercury emission from human activities .....	12
Figure 2.3 A diagram of power plant.....	13
Figure 2.4 A description of different pore sizes in activated carbons .....	16
Figure 2.5 Mercury uptake capacities with sulfur-treated samples based on the mass of coating.....	25
Figure 2.6 Derivative TGA (dTGA) traces of sulfur treated ACFs.....	26
Figure 2.7 High-resolution S 2p spectra of Na <sub>2</sub> S <sub>4</sub> -ACF .....	27
Figure 2.8 A possible structure of sulfur treated ACFs .....	27
Figure 2.9 A possible mechanism for Hg adsorption by a sulfide group .....	30
Figure 2.10 SEM images of ACF (A, C, D) and DMSO-ACF (B).....	34
Figure 2.11 TG curves of brominated ACFs. ....	42
Figure 2.12 XPS spectra of brominated ACFs.....	43
Figure 2.13 Static mercury uptake capacities of brominated samples.....	46
Figure 2.14 A possible mechanism for Hg adsorption using Br-containing group. ....	51
Figure 2.15 STM image of original ACF.....	52
Figure 2.16 XPS of Nov-CAF before and after washing by HCl .....	60
Figure 2.17 C 1s of Nov-CAF .....	61
Figure 2.18 High resolution C 1s and N 1s spectra of PAN-CAF.....	63
Figure 3.1 Nominal pore diameter of different membranes .....	74
Figure 3.2 Schematic of thin-film-composite (TFC) RO membrane and the chemical structure of the aromatic polyamide thin-film layer .....	80
Figure 3.3 Salt rejections and permeation flux of the membranes prepared at different temperatures.....	88
Figure 3.4 MWCO of the membranes prepared at different reaction temperatures .....	90

Figure 3.5 Derivative TGA curves for the membranes prepared using PEI at various reaction temperatures .....	91
Figure 3.6 Surface (left) and cross-sectional (right) morphologies of P84 membranes prepared at different temperatures .....	93
Figure 3.7 Separation performance of selected dyes in methanol solution using the membranes prepared at 70°C .....	95
Figure 3.8 Effect of DMF treatment on membrane performance. ....	96
Figure 3.9 Surface (left) and cross-sectional (right) morphologies of PEI modified P84 membranes prepared at 70°C before and after soaking in DMF for 1 month.....	97
Figure 3.10 Schematic description of the adsorption of a charged homopolymer at a solid surface. Effects of (a) surface charge, (b) electrostatic screening and (c) charge density of the polymer on the amount and the structure of the adsorbed polyelectrolyte.....	99
Figure 3.11 Layer-by-Layer electrostatic assembly of sPEEK and PEI.....	102
Figure 3.12 Salt rejection (■) and flux (◆) of PEMs prepared at different pressures ....	107
Figure 3.13 Effect of ionic strength on PEM performance.....	108
Figure 3.14 Performance of PEMs from (a) branched PEI ( $M_w=25,000$ ) and (b) low $M_w$ PEI ( $M_w=800$ ) with sPEEK in water .....	109
Figure 3.15 Dead-end filtration of model protein solution (bovine serum albumin, 1.0 g/L, 13.79 bars) with our membrane (3 bilayers on PAN200 hydrolyzed 24 hours) and NTR7450.....	116
Figure 3.16 Dead-end filtration of model NOM solution (humic acid 1.0 g/L, 1mM $CaCl_2$ , 13.79 bars) with our membrane (3 bilayers on PAN200 hydrolyzed 24 hours) and NTR7450.....	116
Figure 3.17 Dead-end filtration of model polysaccharide solution (sodium alginate, 1.0 g/L, 13.79 bars) with our membrane (3 bilayers on PAN200 hydrolyzed 24 hours) and NTR7450.....	117
Figure 3.18 ATR-FTIR spectra of the deposition of PEM membranes .....	118
Figure 3.19 SEM micrographs of the transformation of PEM membrane surfaces during deposition (a) hydrolyzed PAN substrate membrane, (b) hydrolyzed PAN membrane deposited with one layer PEI, and (c) hydrolyzed PAN membrane deposited with PEI and sPEEK .....	119

## LIST OF TABLES

Table 2.1 Typical flue gas composition from a coal-fired utility .....	11
Table 2.2 Average mercury capture by coal rank and APCD configuration .....	14
Table 2.3 Ratio of sulfate to sulfide groups in sulfur-treated samples derived from XPS.....	29
Table 2.4 Sulfur content in sulfate and sulfide forms based on carbon materials .....	31
Table 2.5 Porous structure characteristics of sulfur impregnated samples .....	32
Table 2.6 Porous structure characteristics of brominated samples .....	45
Table 2.7 Elemental analysis results of brominated samples .....	47
Table 2.8 Chemical structures of low temperature chemically activated carbon fibers . .	55
Table 2.9 Mercury uptake capacities for CAFs .....	59
Table 2.10 Percentages of functional groups derived from XPS for ACF and Nov-CAF .....	62
Table 2.11 Physical pore properties of CAF samples.....	64
Table 2.12 pH values of CAF samples .....	65
Table 3.1 Principle characteristic of the selected dyes .....	86
Table 3.2 Gel contents of the membranes prepared at various reaction temperatures .....	92
Table 3.3 Performance of PEMs from sPEEK with different sulfonation.....	110
Table 3.4 Properties of different PAN UF membranes.....	113
Table 3.5 Performance of PEMs with various PAN substrates .....	113
Table 3.6 Performance of PEMs with various number of bilayers.....	114

# CHAPTER 1

## INTRODUCTION

### 1.1 Introduction

Environmental pollution has always accompanied development of civilizations. The first trace of pollution dates back to prehistoric times when human beings started to use fires [1]. However, during that period the pollution was comparatively low and could be purified by nature. It was the industrial revolution that gave birth to the accompanying environmental pollution as we know it today [2]. The emergence of large manufacturers gave rise to unprecedented pollution caused by industrial chemical discharges as well as untreated human waste. In the past five years of my research, I have been focusing on the developments of novel materials systems for use in air and water purification. These include,

- 1) Design of chemically treated activated carbon fibers for mercury removal from power plant effluents and
- 2) Design of advanced nanofiltration membranes for water purification and desalination.

### 1.2 Design of chemically treated activated carbon fibers for mercury removal from power plant effluents

Mercury is considered one of the most toxic metals due to its volatility, persistence, bioaccumulation and health impacts on human beings [3,4]. In the USA alone, approximately 50 tons of mercury is released into the atmosphere annually from coal-fired power plants, and this contributes to nearly one third of the U.S. anthropologic mercury emissions [5]. Therefore, mercury control from coal-fired power plants has become an issue of pressing need.

For state of the art control of mercury, one promising technology being studied is sorbent injection [6,7]. However, such systems present practical problems in dealing with the large amount of absorbents required to insure quantitative removal of the Hg. Hence, we have sought to find another system which may solve the problems of carbon injection technology but without changing the whole configuration of current air pollution control devices. As a bag house is often made from fabric filters of glass fiber, we have found that we can successfully prepare activated carbon fibers (ACFs) by coating carbonaceous material made from Novolac precursor on a glass fabric substrate according to the previous work in the Economy group [8,9]. This combined system may adsorb Hg and fly ash simultaneously while still remaining competitive cost to the carbon injection technology. In this thesis, we mainly used this combined system for achieving mercury control down to the range of parts per billion (ppb).

To enhance mercury removal efficiency, various chemically treated carbons were developed including sulfur impregnation [10,11], chloride impregnation [12,13] and bromination [14,15].

In Chapter 2, first we discuss the details about mercury concerns in power plant effluents. Then several methods have been used to introduce sulfur containing groups in ACFs for mercury removal. The chemical and physical properties of these sulfur treated ACFs have been evaluated to determine their mercury adsorption capacities. Although sulfur impregnations decreased surface area and pore volume of ACFs, Hg uptake capacities increased when compared to raw ACF samples. For our sulfur-treated samples, sulfur atoms were incorporated into the carbon matrix in the form of sulfide and sulfate. The sulfide groups appeared to be more effective for mercury removal than sulfate. A

possible mechanism for mercury adsorption, which is likely to involve the oxidation process of  $\text{Hg}^0$ , is also discussed. Besides the effects of chemical structure on mercury adsorption, the effects of pore properties associated with adsorbents have also been studied.

Besides sulfur impregnations, three approaches for bromination to enhance mercury removal were explored; namely, 1) bromination using  $\text{Br}_2$  vapor, 2) bromine deposition by an electrochemical reaction and 3) impregnation of bromine using  $\text{KBr}$  aqueous solution. Both static and dynamic tests were carried out to measure the mercury adsorption performances of these brominated samples. The chemical and physical properties of these brominated ACFs have also been evaluated. For our brominated samples, bromine atoms were incorporated into the carbon matrix which increased Hg uptake capacities when compared to raw ACF samples. A possible mechanism for mercury adsorption likely involves the formation of oxidized mercury complexes (e.g.  $[\text{HgBr}]^+$ ,  $[\text{HgBr}_2]$  and  $[\text{HgBr}_4]^{2-}$ ), is discussed. For the brominated samples treated by  $\text{Br}_2$  vapor and electrochemical method, they showed stable mercury adsorption performance (30% to 33% removal) up to 3 months, which are very promising for commercialization.

Chemically activated carbon fibers (CAFs) were also found to be very effective for mercury removal. Compared with the manufacturing process of ACF, the reacting temperatures of CAF were relatively low, ranging from  $250^\circ\text{C}$  to  $400^\circ\text{C}$ . The CAF samples also showed a higher carbon yield and a more controlled pore size distribution. Additionally, the manufacture process could be done in one step rather than two steps of chemically treated ACFs with synthesis of ACF first followed by chemical treatments. The chemical and physical properties of polyacrylonitrile (PAN) and novolac based

CAFs, and their effects on mercury removal properties are also described in Chapter 2.

### **1.3 Design of advanced nanofiltration membranes for water purification and desalination**

Nanofiltration membranes can be used to separate salts and small molecules from the solution by applying pressure [16]. To be useful in water purification or desalination process, membranes must exhibit a number of characteristics such as high water flux, high salt rejection, mechanical stability, resistance to fouling, and low cost. A number of polymer materials such as cellulose acetates [17], polyamides [18,19,20], crosslinked poly (furfuryl alcohol) [21] and sulfonated polyethersulfone [22] have been investigated for water purification and desalination. Of these, cellulose acetate and polyamide based membranes have been the most successful products. However, they have problems such as low resistance to fouling, limited oxidant tolerance and chemical instabilities [23].

By far most of these processes have dealt with aqueous solutions, however, with the emergence of membranes for use in food applications, petrochemical applications and pharmaceutical areas, the membranes suited for applications in organic media are required [24]. To address this problem, the crosslinking of polyimide membranes is a commonly known method to prepare membranes suitable for solvent resistant nanofiltration. In Chapter 3, preparation of crosslinked membranes of P84 copolyimide asymmetric membranes using branched polyethylenimine (PEI) at different reaction temperatures was studied. The membranes prepared at 70°C showed an optimized performance, with a molecular weight cut off (MWCO) of 226 Da. The rejection sequence of  $\text{CaCl}_2 > \text{NaCl} > \text{Na}_2\text{SO}_4$  indicated a positively charged membrane surface. The rejection of selected dyes including Methyl Orange, Disperse Red and Safranine O ranged from 92% to 98%. Additionally, the resultant membranes were very stable in

dimethyl formamide (DMF), a harsh aprotic solvent. Even after soaking in DMF for 1 month, there were no significant changes in membrane performance or membrane structure. Thus, our membranes have the possibilities to be used in even harsher solvent environments.

Fouling caused by organic impurities such as proteins, humic substances and polysaccharides is another concern for membrane processes [25]. In Chapter 3, we also prepared polyelectrolyte multilayer (PEM) films consisting of sulfonated poly (ether ether ketone) (sPEEK) alternating with polyethyleneimine (PEI) on polyacrylonitrile (PAN) substrate for fouling resistant properties. Two novel variables were introduced in our approach, a) the use of pressure and b) organic solvents, during the alternating physisorption of oppositely charged polyelectrolytes on porous supports through the electrostatic self-assembly. It was shown that the use of pressure could increase the salt rejection of the PEMs by one to two times. The effect of polymer charge density on membrane performance, e.g. sulfonation degree of sPEEK, was also studied. The rejection of the PEMs could be further improved by using methanol as the dip solution and the optimized rejection could reach as high as 89%, which is pretty close to that of a commercially available polyamide membrane (96%). The PEMs also had a better antifouling property in comparison with NTR 7450, a commercial NF membrane with a sulfonated surface.

#### **1.4 References**

- [1] J.D. Spengler, K.A. Sexton, Indoor air pollution: a public health perspective, *Science* 221 (1983) 9–17.
- [2] S. Ross, *The industrial revolution*, Evans Brothers Limited, London, 2008.



- [3] G. Liu, Y. Cai, N. O'Driscoll, *Environmental Chemistry and Toxicology of Mercury*, John Wiley and Sons, Inc., New Jersey, 2010.
- [4] T.W. Clarkson, L. Magos, The toxicology of mercury and its chemical compounds, *Crit. Rev. Toxicol.* 36 (2006) 609-662.
- [5] E.G. Pacyna, J.M. Pacyna, K. Sundseth, J. Munthe, K. Kindbom, S. Wilson, F. Steenhuisen, P. Maxson, Global emission of mercury to the atmosphere from anthropogenic sources in 2005 and projections to 2020, *Atmos. Environ.* 44 (2010) 2487-2499.
- [6] H. Yang, Z. Xu, M. Fan, A.E. Bland, R.R. Judkins, Adsorbents for capturing mercury in coal-fired boiler flue gas, *J. Hazard. Mater.* 146 (2007) 1-11.
- [7] J.H. Pavlish, E.A. Sondreal, M.D. Mann, E.S. Olson, K.C. Galbreath, D.L. Laudal, S.A. Benson, Status review of mercury control options for coal-fired power plants, *Fuel Process. Technol.* 82 (2003) 89-165.
- [8] C.L. Mangun, Z. Yue, J. Economy, Adsorption of organic contaminants from water using tailored ACFs, *Chem. Mater.* 13 (2000) 2356-2360.
- [9] J. Economy, M. Daley, Coated adsorbent fibers, US Patent 5834114, 1998.
- [10] W. Liu, R.D. Vidic, T.D. Brown, Optimization of sulfur impregnation protocol for fixed-bed application of activated carbon-based sorbents for gas-phase mercury removal, *Environ. Sci. Technol.* 32 (1998) 531-538.
- [11] H. Hsi, M.J. Rood, Effects of sulfur impregnation temperature on the properties and mercury adsorption capacities of activated carbon fibers (ACFs), *Environ. Sci. Technol.* 35 (2001) 2785-2791.
- [12] H. Zeng, F. Jin, J. Guo, Removal of elemental mercury from coal combustion flue gas by chloride-impregnated activated carbon, *Fuel* 83 (2004) 143-146.
- [13] S.B. Ghorishi, R.M. Keeney, S.D. Serre, Development of a Cl-impregnated activated carbon for enhanced-flow capture of elemental mercury, *Environ. Sci. Technol.* 36 (2002) 4454-4459.
- [14] R. Patton, Assessment of Low Cost Novel Sorbents for Coal-Fired Power Plant Mercury Control, Apogee Scientific Inc. DE-FC26-01NT41180, 2004.
- [15] J. Wu, J. Chen, S. Zhang, P. He, J. Fang, Y. Wu, Removal of gas-phase elemental mercury by bromine-impregnated activated carbon, *Adv. Mater. Res.* 356-360 (2012) 1660-1663.

- [16] A.I. Schärer, A.G. Fane, T.D. Waite (Eds.), *Nanofiltration—Principles and Applications*, Elsevier Ltd., 2005.
- [17] S. Loeb, S. Sourirajan, Sea water demineralization by means of an osmotic membrane, in *Saline Water Conversion II*, R.F. Gould (ed.)<sup>o</sup>, *Advances in Chemistry Series Number 38*, American Chemical Society, Washington, DC, 1963.
- [18] J.E. Cadotte, Evaluation of composite reverse osmosis membrane, in *Materials Science of Synthetic Membranes*, D.R.Lloyd (ed.), *ACS Symposium Series Number 269*, American Chemical Society, Washington, DC, 1985.
- [19] R.E. Larson, J.E. Cadotte, R.J. Petersen, The FT-30 seawater reverse osmosis membrane-element test results, *Desalination* 38 (1981) 473-483.
- [20] J.E. Cadotte, Interfacially synthesized reverse osmosis membrane, US Patents 4277344, 1981.
- [21] M. Kurihara, N. Harumiya, N. Kannamaru, T. Tonomura, M. Nakasatomi, Development of the PEC-1000 composite membrane for single stage sea water desalination and the concentration of dilute aqueous solutions containing valuable materials, *Desalination* 38 (1981) 449-460.
- [22] K. Ikeda, T. Nakano, H. Ito, T. Kubota, S. Yamamoto, New composite charged membrane, *Desalination* 68 (1986) 109-119.
- [23] J. Glater, S. Hong, M. Elimelech, The search for a chlorine-resistant reverse osmosis membrane, *Desalination* 95 (1994) 325-345.
- [24] P. Vandezande, L. Gevers, I. Vankelecom, Solvent resistant nanofiltration: separating on a molecular level, *Chem. Soc. Rev.* 37 (2008) 365-405.
- [25] M.F.A. Goosen, S.S. Sablani, H. Al-Hinai, S. Al-Obeidani, R. Al-Belushi, D. Jackson, Fouling of reverse osmosis and ultrafiltration membranes: a critical review, *Sep. Sci. Technol.* 39 (2004) 2261-2297.

## CHAPTER 2

### DESIGN OF CHEMICALLY ACTIVATED CARBON FIBERS FOR MERCURY REMOVAL FROM POWER PLANT EFFLUENTS

#### 2.1 Background

Mercury is considered one of the most toxic metals due to its volatility, persistence, bioaccumulation and health impacts on human beings [1,2]. In this Section, we will mainly discuss the backgrounds about mercury concerns from power plant effluents including mercury cycle, mercury in the flue gas, state of the art and mercury measurement method.

##### 2.1.1 Mercury cycle and its toxicity

Mercury in the environment is constantly cycled and recycled through a biogeochemical cycle as shown in Figure 2.1 [3]. By degassing of mercury compounds from sediment and surface waters, or emissions from both natural and anthropogenic activities, gaseous mercury can be formed. Generally, gaseous mercury can travel thousands of miles before it is deposited into the lakes and oceans by precipitation, where it may be transformed into other forms such as an organic form (methylmercury) or an insoluble compound (HgS) and reentry into the atmosphere or bioaccumulation in food chains.

During the mercury cycle process, the formation of methylmercury by bacteria in water is very important due to the toxicity and bioaccumulation of methylmercury [4]. Species like fish and shellfish have a tendency to accumulate and concentrate mercury in their bodies. According to a survey conducted by U.S. Geological Survey and U.S. Department of the Interior, mercury was found in every single fish tested, even in fish of isolated rural waterways [5,6]. The presence of mercury in fish can be a health issues

since methylmercury can accumulate up the food chain. For songbirds and bats who mainly feed on fish, they started to show abnormal incubation and feeding behaviors [7,8]. Excessive accumulation of mercury can also cause neurological damages for human beings such as visual, auditory and walking difficulties. One of the biggest disasters due to mercury poisoning happened in Minamata, Japan, in the 1950s, causing the death of thousands of people [9]. Therefore, mercury poisoning is a serious problem requiring immediate attention. That is why the U.S. National Research Council and Environmental Protection Agency (EPA) set the reference dose for mercury consumption in 2000, at  $0.1 \mu\text{g} \cdot \text{kg body weight}^{-1} \cdot \text{day}^{-1}$  [10].

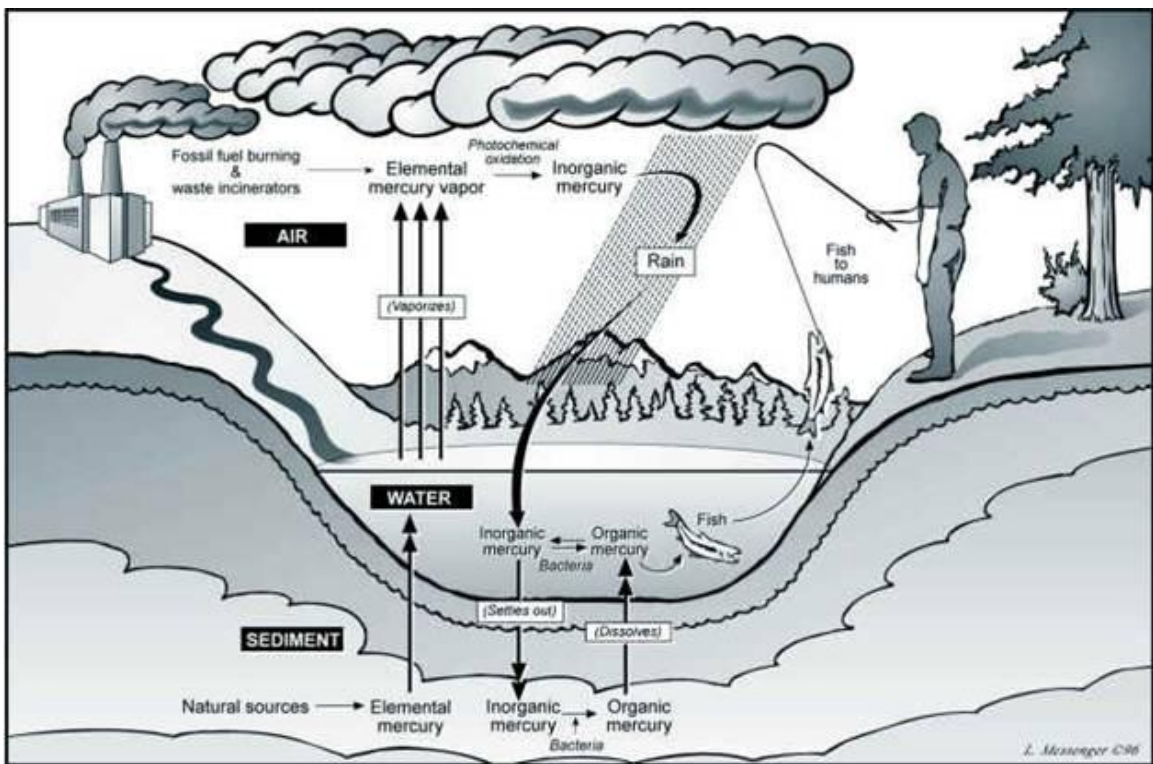


**Figure 2.1 Mercury Cycle [11]**

### 2.1.2 Mercury in the flue gas

There are three main forms of mercury present in the flue gas: particulate-bound, oxidized (primarily mercuric chloride), and elemental mercury [12,13]. Particulate-bound

mercury refers to the mercury adsorbed on to residential particulates (e.g. fly ash), it can be collected using current air pollution control devices such as electrostatic precipitator (ESP) and fabric filter (FF). Oxidized mercury can be captured efficiently using wet scrubbers since it is water-soluble. Conversely, elemental mercury is very difficult to remove because of its high vapor pressure and low water solubility. Thus, control of elemental mercury has been the focus of mercury emissions from coal-fired power plants since it is the most difficult species to be eliminated. In this thesis, we mainly work on the removal of elemental mercury.

The amounts of these three species in flue gas vary from coal to coal [13]. For example, there are 85% of elemental mercury, 10% of oxidized mercury and 5% of particulate-bound mercury for lignite coals. For subbituminous coals, the flue gas consists of 65% of elemental form, 20% of oxidized form and 15% of particulate-bound form.

Besides the presence of different forms of mercury, the mercury concentration in the flue gas can also differ from coal to coal. However, the concentration of mercury in the flue gas is mainly on the order of 1 ppb, as shown in Table 2.1 [14]. Compared with other toxic gases such as NO<sub>x</sub> and SO<sub>x</sub>, the concentration of mercury is much lower, which makes it very difficult to be removed. Selectivity is also a concern for mercury adsorption due to the competitive ingredients in the flue gas, acid gases for example. Additionally, the short residence time (usually less than 1 second) may cause the large surface area within the pores of the adsorbents to be more inaccessible, resulting in a less efficient interaction between adsorbents and mercury. Hence, the mercury is difficult to

be removed from power plant effluents and can not be addressed in a straightforward manner.

**Table 2.1 Typical flue gas composition from a coal-fired utility [14]**

H <sub>2</sub> O	5-6%
O <sub>2</sub>	3-4%
CO <sub>2</sub>	15-16%
CO	25 ppm
Fly ash	10~25%
Total Hg	1 ppb
Hydrocarbons	10 ppm
HCl	100 ppm
SO <sub>2</sub>	1000 ppm
SO <sub>3</sub>	20 ppm
NO <sub>x</sub>	500 ppm
N <sub>2</sub>	Balance

---

Although the mercury concentration in the flue gas is relatively low, mercury emissions from power plant effluents can add up to a large amount and contribute nearly one third to all anthropogenic mercury emissions (Figure 2.2) [15]. In the USA alone, approximately 75 tons of mercury is released from coal-fired power plants each year, and about two thirds of this mercury is emitted into the atmosphere, resulting in an annual emission of around 50 tons. The mercury emission is not localized but a global problem. Asian countries contributed about 67% to the global mercury emissions from anthropogenic sources in 2005, even higher than North America and Europe combined (around 16%) [16]. Therefore, mercury control is an issue of pressing need. On Dec. 21, 2011, the US EPA proposed a new rule regarding mercury emissions, aiming for a 91% reduction of mercury emissions from coal-fired power plants within the following five years [17].

Sources of Human-Made Mercury in the U.S. (1998)

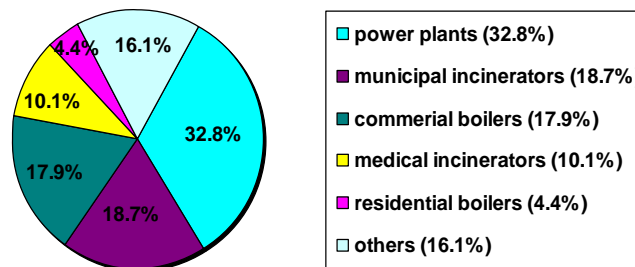


**Figure 2.2 Sources of mercury emission from human activities [15]**

### 2.1.3 State of the art for mercury control

Generally, the current power plant is equipped with air pollution control devices (APCD) such as electrostatic precipitators (ESP) or fabric filters (FF) for particulate

matters and flue gas desulfurization (FGD) for SO<sub>x</sub> as shown in Figure 2.3 [18].

Fortunately, current APCDs can capture some amounts of mercury. Table 2.2 shows the co-benefit of mercury control by current APCDs [19]. Generally, mercury control is also related to coal types. The plants burning bituminous coals show better performance than similarly equipped plants burning subbituminous and lignite due to higher chlorine content in bituminous coals. Additionally, systems equipped with wet FGD devices show better mercury control compared with those without FGD. However, in USA, only 25% of the coal-fired power plants are equipped with wet FGD. Hence, other methods and technologies need to be explored to provide the desired mercury adsorption performance.

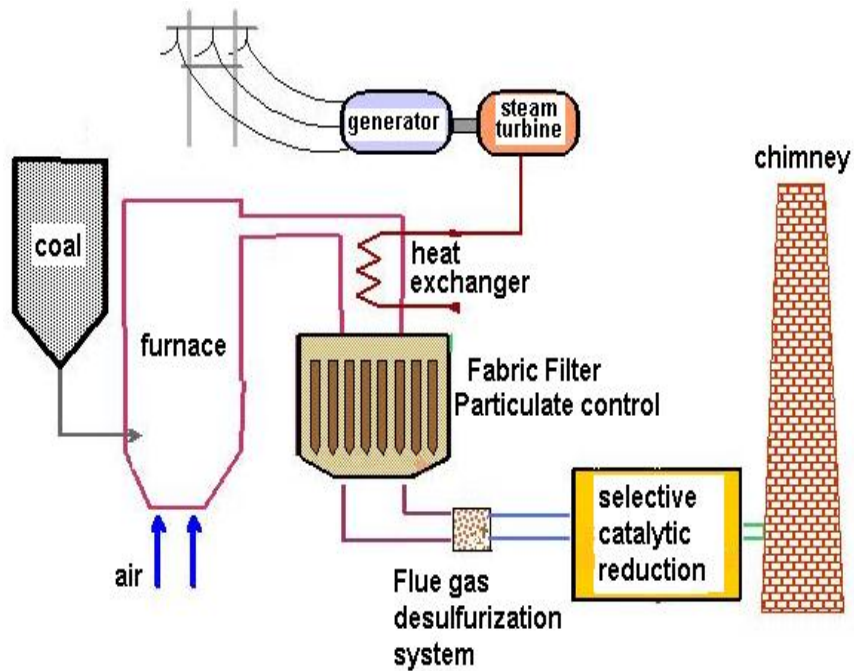


**Figure 2.3 A diagram of power plant**



**Table 2.2 Average mercury capture by coal rank and APCD configuration [19]**

APCD configurations	Average percentage of mercury capture (%)		
	Bituminous	Subbituminous	Lignite
CS-ESP	36	3	-4
HS-ESP	9	6	NA
FF	90	72	NA
PS	NA	9	NA
SDA + ESP	NA	35	NA
SDA + FF	98	24	0
SDA + FF + SCR	98	NA	NA
PS + Wet FGD	12	-8	33
CS-ESP + Wet FGD	74	29	44
HS-ESP + Wet FGD	50	29	NA
FF + Wet FGD	98	NA	NA

CS-ESP: cold-side ESP; HS-ESP: hot-side ESP; PS: particulate scrubber; SDA: spray dryer adsorber.

Many researchers have been studying mercury removal methods and related technologies. One promising technology being studied is sorbent injection [13,20]. Typically the sorbents are injected in the power plant effluent, travel with flue gas, adsorb mercury from flue gas and then are captured along with fly ash using current air pollution control devices such as electrostatic precipitator (ESP) or fabric filter (FF).

Sorbent injection technologies have been relatively successful; however, they suffer from potential problems [20]. For example, since fresh sorbents are needed for each injection, the costs are relatively high. Besides, as a useful byproduct for construction industries, the disposal costs of fly ash are increased since the sorbents tend to contaminate the fly ash. Additionally, excessive loading of particulates may lead to filter bag failure.

Many sorbents have been studied for this kind of technology, including the use of activated carbon [19,21], zeolites [22], fly ash [23,24] and calcium-based adsorbents [25]. Among these sorbents, the overall performance of activated carbon is more effective than

that of other sorbents. Therefore, we will only introduce information about activated carbon in this Section.

#### **2.1.4 Activated carbon and its chemical modifications for mercury removal**

Activated carbons have been used extensively for both air and water purifications [26,27]. It can be produced from carbonaceous source materials with a high char yield such as coal, nutshells, or certain polymers. In most commercial activated carbons, a material is typically carbonized at temperatures above 500°C to form an amorphous or disordered graphitic structure. It is then activated in an oxidant environment to create porosity.

The resultant activated carbons have a highly porous structure with a high surface area. A number of different shapes have been described in literature including slit-shaped, cylindrical, spherical, oval, ellipsoidal etc. Although without direct evidence; a slit-shaped pore is the most commonly accepted for activated carbons [28,29].

Pores are most often characterized by their relative sizes. The International Union of Pure and Applied Chemistry (IUPAC) defines micropore, mesopore and macropore as follows:

Micropore – less than 2 nm pore diameter;

Mesopore – 2 nm to 50 nm pore diameter;

Macropore – larger than 50 nm diameter.

Figure 2.4 shows a description of the different types of pores sizes in activated carbons. Generally, micropores are mainly responsible for adsorption due to the higher overlap in potential from the van der Waals forces of opposite wall size. On the other

hand, mesopores may serve as transportation channels due to their larger pore size [30,31].

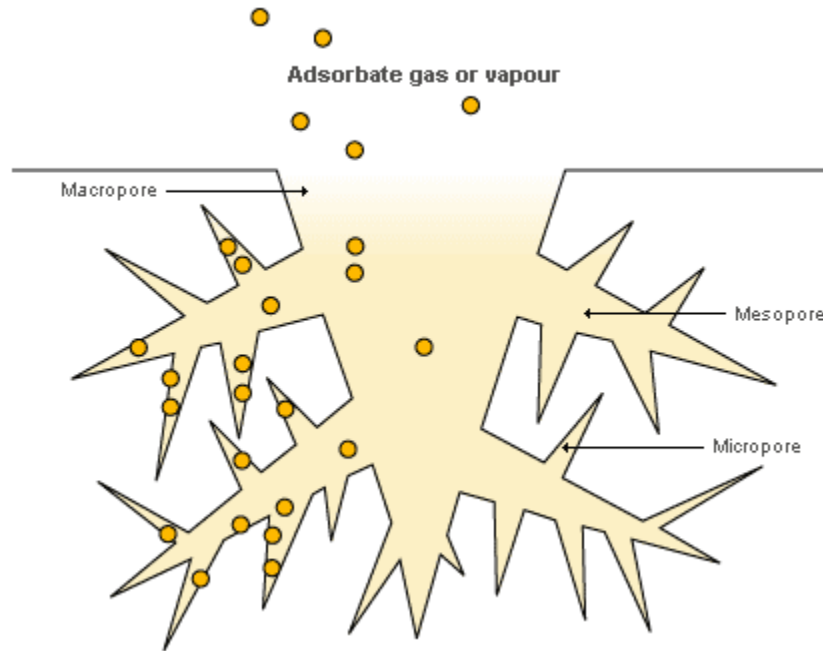


**Figure 2.4 A description of different pore sizes in activated carbons**

Physical adsorption is the primary means by which activated carbons work to remove contaminants. However, at higher temperatures in excess of 150°C, the adsorbed contaminants will be desorbed causing a decrease in physical adsorption capability [30,32]. Hence, various chemically treated carbons were developed to enhance the mercury removal efficiency including sulfur impregnation [33,34], chloride impregnation [35,36] and bromination [32,37].

### **2.1.5 Activated carbon fibers and our objectives**

We sought to find another system which may solve the problems of carbon injection technology but without changing the whole configuration of current air pollution control devices. As a bag house is often made from fabric filters of glass fiber felts, instead of injecting the carbon into the flue gas, we decided to coat the carbonaceous materials on

the fabric filter. Previously done in the Economy group [38,39], we have found that we can successfully prepare activated carbon fibers (ACFs) by coating carbonaceous material made from Novolac precursor on a glass fiber substrate. This combined system may adsorb Hg using the activated carbon coating while capture the fly ash using the appropriate form of glass fiber.

Compared with carbon injection technology, this combined system has several advantages. For example, the sorbent costs would be relatively low. Assuming the combined system could collect all the emitted mercury, since bag houses only need to be replaced every two to three years, sorbent costs of this combined system would compares favorably to that of carbon injection technology which requires large amounts of activated carbon powders to be injected continuously to insure removal of Hg. Additionally, the quality of the fly ash should remain unaffected since fly ash is collected by shaking the fabric filter while Hg is adsorbed on the carbon coating on the fabric filter and would not be shaken off. As proposed by PPG baghouse experts, the carbon coated fabric filter containing Hg would be sent back to the coal mine of origin to be buried underground after usage.

Similar to activated carbon, virgin ACFs can only capture small amounts of mercury. To enhance the mercury uptake capacities, several approached were tried as listed below:

- 1) sulfur treated ACFs (Section 2.2)
- 2) brominated ACFs (Section 2.3)
- 3) chemically activated carbon fibers (Section 2.4).

### **2.1.6 Mercury measurement method**

A detection system for mercury is necessary in order to determine the mercury uptake capacity. The most common technique used for mercury determination involves the use of ultraviolet spectrophotometry [40], including atomic absorption spectrophotometry (AAS) and atomic fluorescence spectrophotometry (AFS). This kind of technique is based on the absorption line of 253.7 nm for elemental mercury.

Another approach to test the amount of elemental mercury is based on a resistivity method [41]. For a thin gold film, in the presence of mercury vapor, the electric resistance will be proportional to the mass of mercury adsorbed in the sample. A Jerome analyzer will be used for this technique.

A mass spectrometer can also be used as a continuous detector for mercury. However, the 1 ppb concentration of mercury in the flue gas is near the limit of many mass spectrometers [40,42].

For our experiment, we used a mass spectrometer to screen out the samples since this method is simple, straightforward and provides ease of access. Then, for samples with relatively good mercury adsorption performance, another test which involves the use of radioactive mercury will be performed. By counting the gamma rays from radioactive mercury disintegration, mercury concentration down to ppt level can be detected.

## **2.2 Design of sulfur treated activated carbon fibers (ACFs) for mercury removal**

### **2.2.1 Overview**

The most common form of mercury in sediment is known as cinnabar (mercuric sulfide) [43]. In cases of mercury spills (such as thermometers or fluorescent light bulbs),

fine sulfur can be spread over the area before being collected and properly disposed of [44]. Due to the fact that the reaction between sulfur and mercury happens readily at ordinary temperatures, sulfur is considered as an effective promoter for mercury removal.

Sulfur-impregnated activated carbons (AC) have been studied extensively at the University of Pittsburgh [33,45,46]. By reacting with H<sub>2</sub>S, several sulfur forms are introduced into activated carbons, including sulfide, sulfoxide, elemental sulfur, sulfone, thiophene and sulfate. By comparing the relationship between Hg uptake and different sulfur forms, Vidic concluded that elemental sulfur, thiophene, and sulfate groups were likely responsible for mercury uptake. Hsi et al. at the Geological Survey at UIUC have also studied mercury adsorption using an impregnated sulfur deposited on activated carbons [34,47,48]. By varying the sulfur impregnation temperature from 250 °C to 650 °C, the authors reported the equilibrium Hg<sup>0</sup> adsorption capacity ranging from 2.2 mg/g C to 11.3 mg/g C.

For the use of activated carbons, sulfur powder can be simply mixed with carbon powders followed by high temperature treatments. In our case, ACFs are used in the mat form, hence they cannot be ground to powder form before treatments. Also the advantages of ACF to AC such as improved contact efficiency will be lost. We tried several methods to introduce sulfur containing groups in ACFs. In this Chapter, the chemical and physical properties of these sulfur treated ACFs have been evaluated to determine their mercury adsorption capacities. Although sulfur impregnations decreased surface area and pore volume of ACFs, Hg uptake capacities increased when compared to raw ACF samples. For our sulfur-treated samples, sulfur atoms were incorporated into the carbon matrix in the form of sulfide and sulfate. The sulfide groups appeared to be more

effective for mercury removal than sulfate. A possible mechanism for mercury adsorption, which is likely to involve the oxidation process of  $\text{Hg}^0$ , is also discussed. Besides the effects of chemical structure on mercury adsorption, the effects of pore properties associated with adsorbents have also been studied.

## **2.2.2 Experimental**

### *2.2.2.1 Materials*

Glass fibers were provided by PPG Industrial. Novolac resin 2074 was obtained from Georgia Pacific.  $\text{CO}_2$ ,  $\text{N}_2$ ,  $\text{O}_2$  gases are lab grade from S.J. Smith Welding, Inc.  $\text{Na}_2\text{S}_4$  (28 -30 wt% solution) was supplied by Tessnederlo Kerley, Inc. Other chemicals used were all from Sigma-Aldrich unless indicated.

### *2.2.2.2 Preparation of activated carbon fibers (ACFs)*

Based on previous work in the Economy group, ACFs were made from Novolac precursor coated on a glass fiber [38,39]. This synthetic process not only lowered the cost but also simplified the manufacture. Compared with activated carbon granules, ACF coated on a glass fiber substrate showed improved wear resistance and contact efficiency. The glass fibers were impregnated with a Novolac precursor (Novolac 4.17 g, hexamethylenetetramine 0.28 g, ethanol 100 ml) and placed in the hood overnight to be dried. The coated glass fibers were partially cured first by heating to  $100\text{ }^\circ\text{C}$  for 20 minutes to further remove solvent, then heated to  $170\text{ }^\circ\text{C}$  and kept at  $170\text{ }^\circ\text{C}$  for 3 hours. The cured samples were activated in flowing  $\text{N}_2$  by heating to  $600\text{ }^\circ\text{C}$  ( $\sim 10\text{ }^\circ\text{C}/\text{min}$ ) and then switching to  $\text{CO}_2/\text{H}_2\text{O}$  and holding for 5 hours. (The activation gas was generated by bubbling  $\text{CO}_2$  through liquid water.) After activation, the ACFs were cooled in flowing

N<sub>2</sub>. The samples were washed with deionized water and dried under vacuum at 120 °C for at least 12 hours before using.

### 2.2.2.3 Preparation of sulfur impregnated ACFs

Several sulfur impregnation methods were tried to introduce sulfur on ACFs. DMSO-ACF was made from DMSO (dimethyl sulfoxide) according to the Durante et al approach [49], where ACF was soaked in DMSO for 30 min and placed in the hood to be dried. The sample was then heated to 200°C for 30 min, and air was used to decompose a portion of the sulfur compound but not to decompose it to elemental sulfur. The sample was washed with deionized water and dried in a vacuum oven at 80 °C overnight before use.

Na<sub>2</sub>S<sub>4</sub> is also noted to be very effective for Hg capture [50]. In our method, sulfur was introduced to ACF by Na<sub>2</sub>S<sub>4</sub> decomposition (Na<sub>2</sub>S<sub>4</sub>-ACF). Thus, ACF was soaked in 10 wt% Na<sub>2</sub>S<sub>4</sub> in a sodium hydroxide (NaOH) aqueous solution (pH=10~12) for 30 min and placed in the hood to be dried. Then the sample was heated to 400°C for 6 hours. N<sub>2</sub> was used to maintain an oxygen free condition. After the heating, the sample was washed with D. I. water and dried in the hood.

Another sulfur impregnation method developed by ourselves used NaSH. The samples were identified as NaSH-ACF. Thus, ACF was soaked in 10 wt% NaSH solution for 30 min and placed in the hood to dry. Then the sample was heated to 400°C for 3 hours. N<sub>2</sub> was used to maintain an oxygen free condition. After heating, the sample was washed with D. I. water and dried in the hood.



The samples made from sulfur vapor were labeled as S(v)-ACF. This method was inspired by Hsi et al approach [34,47,48], in their papers carbon powder is mixed with sulfur powder and reacted at high temperatures (250 °C to 650°C). In our process, a combustion boat containing approximately 6 g of sulfur was placed in the furnace, followed by three boats containing ACF (the weight of the three pieces of ACF with glass fibers totaled 12 g). The samples were heated to 400°C for 5 hours. N<sub>2</sub> was used to blow off the excess sulfur and to maintain an oxygen free condition. After heating, the samples were washed with D. I. water and dried in the hood.

Na<sub>2</sub>S<sub>4</sub>-HSO<sub>3</sub>-ACF was made by two steps of sulfur impregnations; a method also developed by ourselves. ACFs were functionalized in concentrated sulfuric acid for 4 hours at 140°C. After sulfonation, the samples were rinsed with 0.1 M NaHCO<sub>3</sub> solution to neutralize any residual acid, then rinsed with distilled water, and dried in the hood. After the sulfonation process, the sulfonated samples were impregnated with 10 wt% Na<sub>2</sub>S<sub>4</sub> in NaOH solution for 30 minutes and placed in the hood. Then the samples were heated to 200°C for 30 minutes. N<sub>2</sub> was used to maintain an oxygen free condition. After heating, the samples were washed with D. I. water and dried in the hood. The intent was that Na ions would attach to the negatively charged sulfonated samples, leaving S ions being active.

#### *2.2.2.4 Static mercury uptake test*

Static mercury capacity test was run by PPG Inc. The sample (8 cm\*8 cm) was suspended in a saturated mercury vapor in air at room temperature (~21 ng/mL). After

two weeks, the weight change was measured assuming all the increased weight was attributed to Hg adsorption.

#### 2.2.2.5 *Characterization techniques*

All the samples were heated at 120°C in a vacuum oven overnight to remove moisture and other adsorbed contaminants.

The amount of the carbonaceous material coated on glass fiber mat was measured using a Hi-Res TA instrument 2950 thermogravimetric analyzer (TGA) by burning off the coating in air at 750°C. The samples (10-20 mg) were heated at 10°C/min to 750°C, and then held at that temperature for 30 min.

A Model CE440 elemental analyzer (EA) was used to determine the C, H, S, and N weight percentages in the samples. The oxygen contents were calculated by mass difference after combining the results of TGA and assuming the glass weight remained unchanged after burn-off and that there were no other elements in the samples.

X-ray photoelectron spectroscopy (XPS) experiments were performed on a Kratos Axis ULTRA. XPS spectra were obtained using an X-ray source operated at 13 kV and 10 mA. Survey scans were collected from 0-1100 eV with a pass energy of 160 eV. High-resolution scans were performed with the pass energy adjusted to 40 eV. The pressure inside the vacuum system was maintained at approximately  $10^{-9}$  Torr during all XPS experiments. XPS spectra were analysed using a software called CasaXPS (Version 2.3.14). The carbon 1s electron binding energy was referenced at 284.5 eV for calibration [51].

The analysis of surface area and average pore size was carried out with an Autosorb-1 apparatus (Quantachrome). All samples were outgassed at 150°C until the test of outgas pressure rise was passed by 5 µg Hg/min prior to their analysis. Nitrogen isotherm at 77K was used for further calculation. Nitrogen surface area was determined using the standard Brunauer-Emmett-Teller (BET) equation [52]. Average pore size and micropore volume were determined using the Dubinin-Radushkevich (DR) equations [53]. The volume of mesopores of the samples was calculated by subtracting the volume of micropores from the total pore volume at a relative pressure of 0.95.

A commercial Hitachi S-4800 scanning electron microscope (SEM) was used for high resolution examination of the surface of our samples. The accelerating voltage used for all runs was 1.0 kV. The image size varied with samples.

### **2.2.3 Results and discussions**

#### *2.2.3.1 Mercury uptake capacities of sulfur-treated ACFs*

All sulfur-treated samples increase the mercury uptake capacities compared with the original ACF as shown in Figure 2.5. Comparing the mercury uptake capacities with the sulfur contents in the samples, our samples can be roughly divided into two groups depending on their effectiveness for mercury adsorption. One group (Type I) includes DMSO-ACF, Na<sub>2</sub>S<sub>4</sub>-ACF and Na<sub>2</sub>S<sub>4</sub>-HSO<sub>3</sub>-ACF; all these samples show little mercury uptake (less than 8 times increase compared with raw ACF) even with a large amount of sulfur (over 20 wt%). The other group (Type II) includes NaSH-ACF and S(v)-ACF; both samples increase mercury uptake capacity dramatically (over 10 times compared to the virgin ACF) with only a small amount of sulfur having been impregnated (i.e.,

approximately 6 to 7 wt%). In order to determine why Type II samples capture Hg more effectively than Type I samples, chemical structures and pore properties of all sulfur-treated samples will be discussed in more detail in this Section.

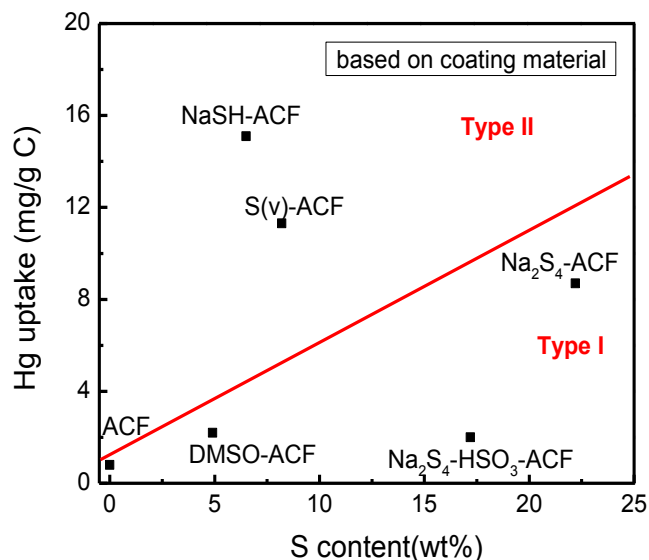


**Figure 2.5 Mercury uptake capacities with sulfur-treated samples based on the mass of coating**

### 2.2.3.2 Chemical structures of sulfur-treated ACFs

During the activation process, CO<sub>2</sub>/H<sub>2</sub>O etches the edges of the carbonaceous material, creating a random (but locally semi-organized) number of graphite platelets [26]. Our samples consist of around 10 wt% carbon on glass fiber substrates. As seen in Figure 2.6, the peak around 525°C for ACF is attributed to the burn-out of carbonaceous material. All the sulfur treated ACFs have similar weight loss peaks between 500°C to 550°C, this may suggest that sulfur atoms have been incorporated into the surface carbon matrix. One exception is Na<sub>2</sub>S<sub>4</sub>-HSO<sub>3</sub>-ACF, besides the carbon burn-out peak, there is another peak around 300°C. Since Na<sub>2</sub>S<sub>4</sub>-HSO<sub>3</sub>-ACF is made by two steps of sulfur

impregnation,  $\text{Na}_2\text{S}_4$  is introduced onto the samples after sulfonation; the sample is not thermally stable. At higher temperature, around  $300^\circ\text{C}$  in this case,  $\text{Na}_2\text{S}_4$  is decomposed into  $\text{Na}_2\text{S}$  and  $\text{S}$ , while  $\text{Na}_2\text{S}$  may still connect to the negatively charged sulfonated groups by electrostatic force,  $\text{S}$  can react with  $\text{O}_2$  to form  $\text{SO}_x$ , resulting in another weight loss peak.

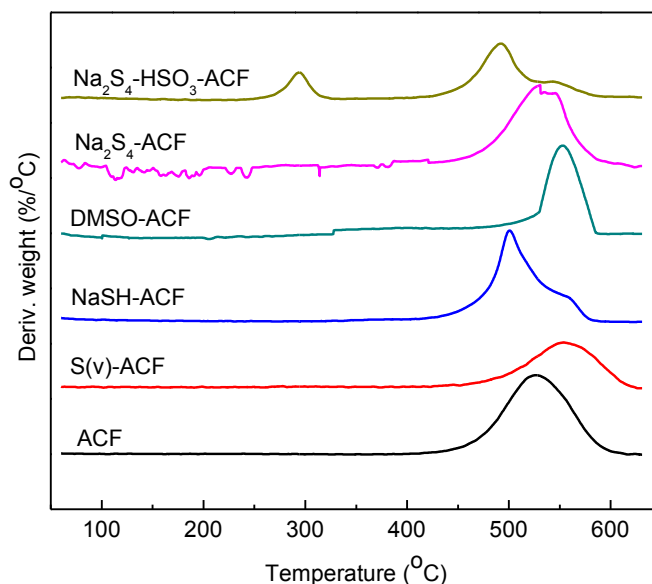


**Figure 2.6 Derivative TGA (dTGA) traces of sulfur treated ACFs**

Based on XPS, the functional groups in all the sulfur treated samples are sulfide and sulfate groups. Figure 2.7 shows the high-resolution S 2p spectra of  $\text{Na}_2\text{S}_4$ -ACF, representing one of the sulfur treated samples. Two peaks appear in the spectra, one corresponds to the sulfide groups (161 – 165 eV), while the other one belongs to the sulfate groups (168 – 172 eV) [51]. All the other sulfur-treated ACFs have similar S 2p spectra with  $\text{Na}_2\text{S}_4$ -ACF; consisting of two peaks corresponding to sulfide and sulfate groups. Based on the results from TGA and XPS, a possible structure of sulfur-treated

samples is shown in Figure 2.8. Except for Na<sub>2</sub>S<sub>4</sub>-HSO<sub>3</sub>-ACF, all the other sulfur-treated ACFs have similar chemical structures since they have similar TGA and XPS curves, although the concentration of different functional groups may vary. One exception is Na<sub>2</sub>S<sub>4</sub>-HSO<sub>3</sub>-ACF, besides the fundamental structure shown in Figure 2.8, Na ions can interact with the negatively charged sulfonated groups by electrostatic forces, leaving S ions being active.

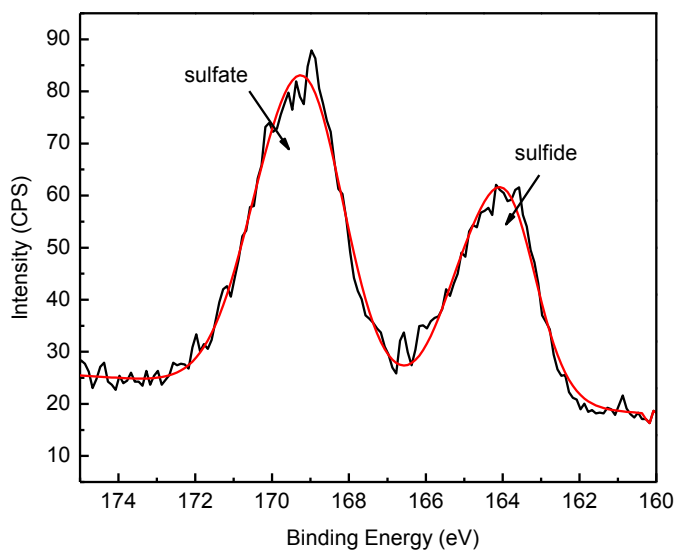


**Figure 2.7 High-resolution S 2p spectra of Na<sub>2</sub>S<sub>4</sub>-ACF**

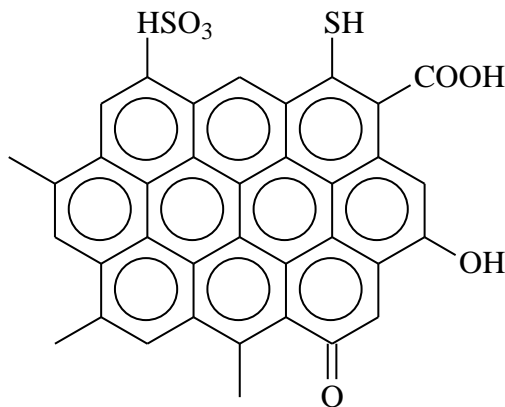


**Figure 2.8 A possible structure of sulfur treated ACFs**

### 2.2.3.3 *Effects of chemical structures on mercury adsorption*

The concentrations of sulfate and sulfide groups of sulfur-treated samples derived from XPS data are listed in Table 2.3. For Type I, the samples are primarily sulfate, while for Type II, the majority of the functional groups—over 60 wt%—are sulfide. Since type I and type II are grouped by their effectiveness for Hg removal, sulfide groups are generally more effective for Hg removal than sulfate. According to previous studies by Vidic [46], elemental sulfur, thiophene, metal sulfide and sulfate are stated to be likely responsible for mercury uptake; and sulfate is more effective than sulfide in Hg removal performance. At first glance, our results seem to be inconsistent with the previous work. However, careful examination shows that Vidic's data are questionable. His data are too scattered to be fitted linearly and in the range of 0-0.6 wt% S content, sulfide should be equally effective, if not more effective than the sulfate groups for mercury adsorption. Although the reason why some form of sulfur groups are more effective for mercury adsorption than other kind of sulfur groups is still unclear yet, it is reported that at least one lone pair of electrons should remain available for interaction with mercury, or at least as a point of initial attachment [49]. In this case, sulfide groups have two lone pairs of electrons; hence they are capable of interacting and binding zero-valent mercury. On the other hand, as all of the electrons of sulfur have been occupied, it is reasonable to presume that sulfate groups have little or limited effects on adsorbing zero-valent mercury. Therefore, our results are reasonable where sulfide groups are more responsible for Hg removal than sulfate groups.

If a lone pair of electrons serves as the active site for sulfur interaction with mercury, or as a point of initial attachment, we can propose the following three-step

mechanism for Hg adsorption: (1) oxidation; (2) electron transfer; and (3) rearrangement. These, Hg(0) is oxidized to Hg(II) and forms a double bond with S using two pairs of shared electrons. Then, one electron transfers from the Hg=S double bond to C-S single bond, leaving one electron of the Hg and one electron of the carbon being reactive. Finally, the reactive electron of the Hg and the reactive electron of the carbon form a single bond. And the bond, which originally connected C and S, breaks and creates a lone pair of electrons. The illustration of the mechanism for Hg adsorption is shown in Figure 2.9.

**Table 2.3 Ratio of sulfate to sulfide groups in sulfur-treated samples derived from XPS**

	Sulfate (wt%)	Sulfide (wt%)	
DMSO-ACF	92.61	7.38	} Type I
Na <sub>2</sub> S <sub>4</sub> -ACF	62.49	37.50	
Na <sub>2</sub> S <sub>4</sub> -HSO <sub>3</sub> -ACF	67.73	32.28	
NaSH-ACF	37.78	62.22	} Type II
S(v)-ACF	15.59	84.42	



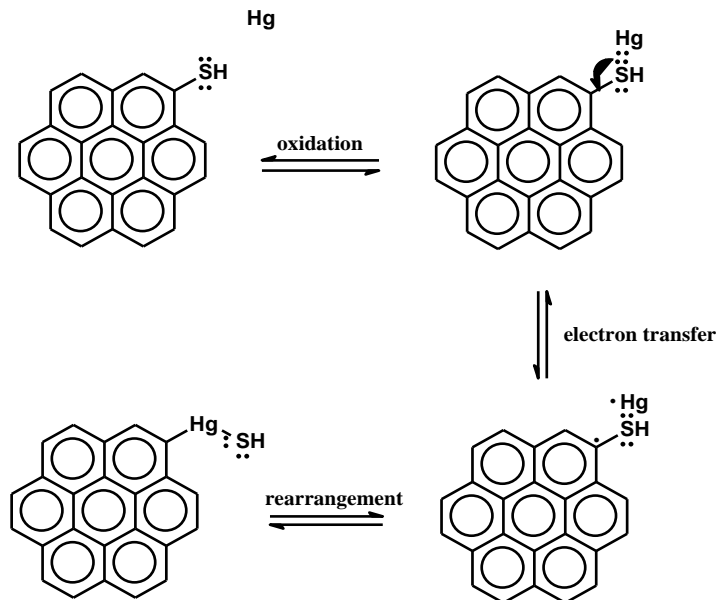


**Figure 2.9 A possible mechanism for Hg adsorption by a sulfide group**

Based on the total sulfur content from elemental analysis results and ratio of sulfide to sulfate groups derived from XPS, the sulfur content in sulfide and sulfate forms can be calculated, as shown in Table 2.4. If mercury adsorption is only controlled by sulfide groups present on the carbon surface, the mercury uptake capacity should be of the order of  $\text{Na}_2\text{S}_4\text{-ACF} > \text{S(v)-ACF} > \text{Na}_2\text{S}_4\text{-HSO}_3\text{-ACF} > \text{NaSH-ACF} > \text{DMSO-ACF}$ . However, the mercury uptake capacity is actually of the order of  $\text{NaSH-ACF} > \text{S(v)-ACF} > \text{Na}_2\text{S}_4\text{-ACF} > \text{DMSO-ACF} \sim \text{Na}_2\text{S}_4\text{-HSO}_3\text{-ACF}$ . Therefore, in addition to chemical structure, other factors such as physical pore properties may also play a role on Hg removal.

**Table 2.4 Sulfur content in sulfate and sulfide forms based on carbon materials**

	Total Sulfur Content (wt%)	Sulfur Content in Sulfate Form (wt%)	Sulfur Content in Sulfide Form (wt%)
DMSO-ACF	4.9	4.5	0.4
Na <sub>2</sub> S <sub>4</sub> -ACF	22.2	13.9	8.3
Na <sub>2</sub> S <sub>4</sub> -HSO <sub>3</sub> -ACF	17.2	11.6	5.6
NaSH-ACF	6.5	2.5	4.0
S(v)-ACF	8.2	1.3	6.9

#### 2.2.3.4 Effects of physical pore properties on mercury adsorption

Table 2.5 shows the physical pore properties of sulfur-treated samples. Generally, introducing sulfur groups tends to block the pores, resulting in a decrease in surface area and a reduction in pore volume [34]. Micropores are pores less than 2 nm diameter, while the diameter of mesopores is in the range of 2 to 50 nm. Since micropores will benefit from the overlapping adsorption potentials of opposite pore walls, sulfur containing groups would be attracted to micropores and block them while leaving the mesopores. This probably explains why sulfur treated samples appear to have larger pores compared with raw ACF.

As shown in Table 2.5, except S(v)-ACF, all sulfur treated samples appear to have larger pores and decreased surface areas compared with raw ACF. Unlike all the other sulfur-treated samples for which ACFs are treated with precursor solutions first and then heated up to high temperature, S vapor is used for S(v)-ACF. S vapor can act as an activation gas, attacking the outer surface of the carbon and etching more rather than depositing in inner pores, resulting in an increase in both surface area and pore volume. Some sulfur treated samples, i.e. Na<sub>2</sub>S<sub>4</sub>-HSO<sub>3</sub>-ACF and DMSO-ACF, show relatively low pore volumes and surface areas. For Na<sub>2</sub>S<sub>4</sub>-HSO<sub>3</sub>-ACF, by introducing Na<sub>2</sub>S<sub>4</sub> on

sulfonated ACFs, the two steps of sulfur impregnation not only block the pores but also damage the pore structure, resulting in a relatively low surface area and pore volume. For DMSO-ACF, as the carbon matrix is not thermally stable in O<sub>2</sub>, the burn out of some amount of carbon at low temperature (200°C in this case) probably causes partial structural collapse and loss of porosity and surface area.

**Table 2.5 Porous structure characteristics of sulfur impregnated samples**

	Specific surface area (m <sup>2</sup> /g)	average pore size (Å)	pore volume (mL/g)	Micro-pores	Meso-Pores	
ACF	487	33	0.4071	60%	40%	
DMSO-ACF	62	30	0.0462	61%	39%	} Type I
Na <sub>2</sub> S <sub>4</sub> -ACF	109	56	0.1541	9%	91%	
Na <sub>2</sub> S <sub>4</sub> -HSO <sub>3</sub> -ACF	47	120	0.0719	10%	90%	
NaSH-ACF	254	63	0.2662	23%	77%	} Type II
S(v)-ACF	624	103	0.7063	2%	98%	

Besides specific chemical structures, the mercury uptake capacity also depends on surface area and pore structure [13]. Usually micropores possess the majority of the active sites for mercury adsorption, while mesopores act as transport routes [31,54]. Compared with Na<sub>2</sub>S<sub>4</sub>-ACF, S(v)-ACF and Na<sub>2</sub>S<sub>4</sub>-HSO<sub>3</sub>-ACF, which consist mainly of mesopores, NaSH-ACF contains both micropores and mesopores. Although all three sulfur-treated samples have more sulfide groups than NaSH-ACF, their pore properties make Hg easier to be transported through but more difficult to be adsorbed. Hence, they show lower mercury capacities than NaSH-ACF. The same reasoning may also explain why Na<sub>2</sub>S<sub>4</sub>-HSO<sub>3</sub>-ACF and DMSO-ACF have similar Hg capacities while the sulfur content in sulfide groups of the former is ten times higher than that of the latter. However, the relatively low sulfur content in sulfide groups and pore volume still make

the capacity of DMSO-ACF much lower than  $\text{Na}_2\text{S}_4$ -ACF and S(v)-ACF. For  $\text{Na}_2\text{S}_4$ -ACF and S(v)-ACF, both samples have relatively high sulfur contents in the form of sulfide groups and mainly consisted of mesopores. The reason why  $\text{Na}_2\text{S}_4$ -ACF is not as effective as S(v)-ACF is because S(v)-ACF has a much higher surface area and pore volume than  $\text{Na}_2\text{S}_4$ -ACF.

#### *2.2.3.5 Morphology study*

The SEM images of ACF are also investigated. The carbonaceous material is coated on nonwoven fiber glass mat with a fiber diameter of 5-7  $\mu\text{m}$  as shown in Figure 2.10A. The image is clearer in Figure 2.10C, wherein a thin layer of coating is shown on a single glass fiber. Although micropores are invisible in SEM, large amounts of mesopores and some amounts of macropores exist in the carbonaceous coating material (Figure 2.10D), suggesting ACF has a highly porous structure. There are no significant differences in SEM images between ACF and sulfur-treated ACFs. In Figure 2.10B is shown the SEM of DMSO-ACF, representing one of the sulfur-treated ACFs. Based on our previous conjecture of chemical structures of sulfur-treated ACFs, sulfur atoms can be built-in with carbon matrix; hence no cluster of sulfur should be seen in the SEM image. This explains why the SEM images look similar for ACF and all sulfur-treated ACFs.

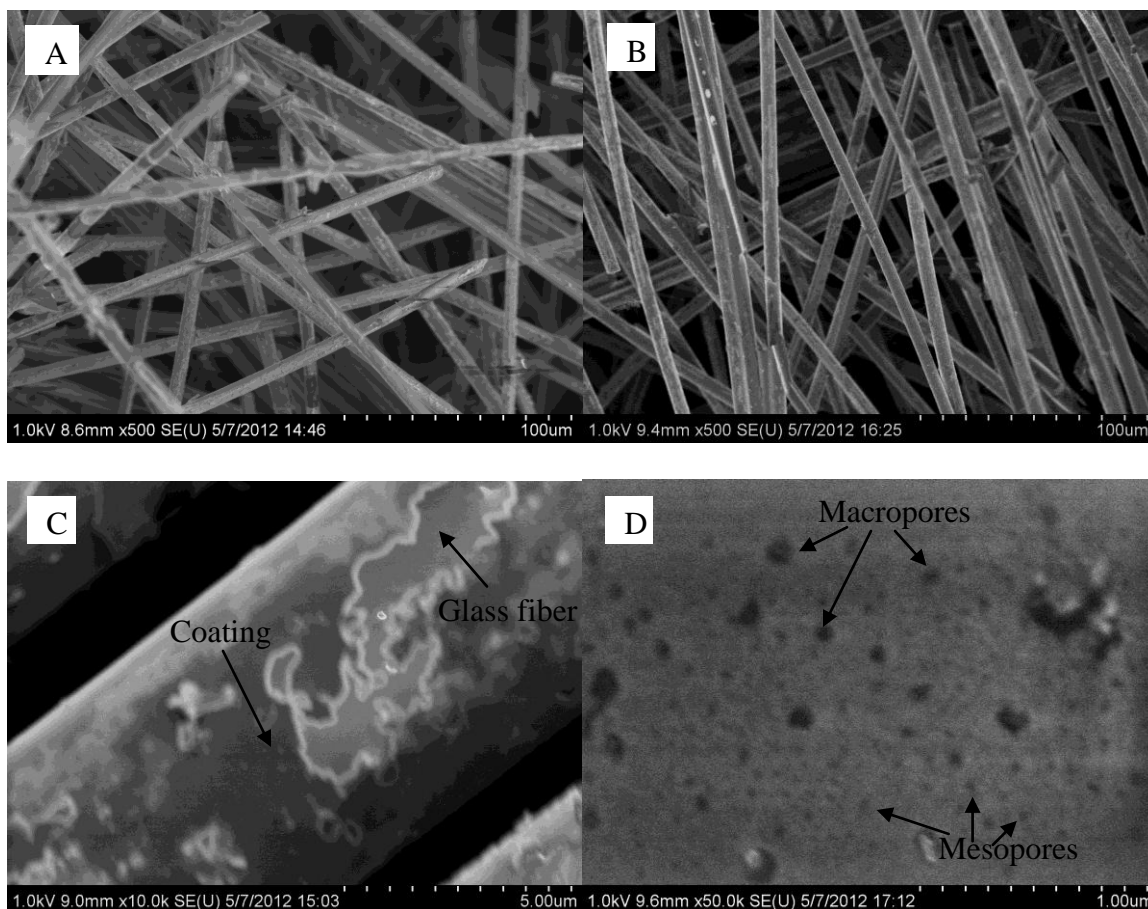


**Figure 2.10 SEM images of ACF (A, C, D) and DMSO-ACF (B)**

## 2.2.4 Conclusions

Although the mechanism for mercury adsorption is still not yet well understood, based on our studies, both chemical structure and physical pore properties play an important role on Hg adsorption. The incorporation of sulfur groups appears to facilitate the oxidation process of Hg and subsequent bonded with oxidized Hg, resulting in higher Hg capacities. Sulfide groups appear to be more effective for mercury removal than sulfate groups since the lone pairs of electrons of sulfide groups are responsible for interaction with mercury, or at least as a point of initial attachment. Additionally, physical properties associated with sorbent properties such as surface area, pore volume

and pore size also affect mercury adsorption performance. For example, as stated earlier micropores are responsible for Hg adsorption while mesopores serve as transport route.

In general, sulfur impregnation decreases surface area and increases Hg uptake capacity when compared to raw ACF samples [34,47,54]. Our best results for mercury uptake is 11-15 mg/g C with sulfur content between 6-7 wt% for NaSH-ACF and S(v)-ACF. The results are comparable with previous reports, which ranged from 2 mg/g to 11 mg/g by varying sulfur impregnation temperature from 250°C to 650°C [34,47,48] and usually less than 2 mg/g by reacting with H<sub>2</sub>S [33,45,46].

For the future, our methods may show even higher mercury uptake capacity since our experimental procedure has not been optimized yet. Take the S(v)-ACF for example, a number of variables may be modified to achieve the optimized results, like the S/ACF ratio, sulfur impregnation temperature, reaction time and the flow rate of carrier gas. By varying those conditions, better results may be achieved. Additionally, the combined system shows great potential for commercialization since they may collect fly ash and mercury simultaneously.

## **2.3 Design of brominated activated carbon fibers (ACFs) for mercury removal**

### **2.3.1 Overview**

The results in Section 2.2 indicate that sulfur treated ACFs show good mercury uptake capacities (11-15 mg/g C for our best samples). Consequently, we started to explore other moieties which also show strong affinity for mercury. Previously in our group, Foster had successfully prepared chlorinated ACFs by reacting ACFs with Cl<sub>2</sub> gas [55]. Based on the methods described by Foster, the mercury uptake capacities for

chlorinated ACFs were tested, which ranged between 30-40 mg/g C. The results for chlorinated ACFs were inspiring to us. After that, brominated ACFs were tried since bromine is in the same column with chlorine in the period table and softer than chlorine.

In this Section, three methods have been developed to incorporate bromine containing groups in activated carbon fibers (ACFs) involving the use of bromine vapor, KBr impregnation and an electrochemical method using KBr solution. For our brominated samples, bromine atoms were incorporated into the carbon matrix which increased Hg uptake capacities when compared to raw ACF samples. The chemical and physical properties of these brominated ACFs have also been evaluated. Both static and dynamic tests were carried out to measure the mercury adsorption performances of these brominated samples. A possible mechanism for mercury adsorption, which involves the formation of oxidized mercury complexes (e.g.  $[\text{HgBr}]^+$ ,  $[\text{HgBr}_2]$  and  $[\text{HgBr}_4]^{2-}$ ), is also discussed. For the brominated samples treated by  $\text{Br}_2$  vapor and the electrochemical method, they showed stable mercury adsorption performance (30% to 33% removal) up to 3 months, which are very promising for commercialization.

## **2.3.2 Experimental**

### *2.3.2.1 Materials*

Glass fiber was provided by PPG Industrial. Novolac resin 2074 was obtained from Georgia Pacific.  $\text{CO}_2$  gas was lab grade from S.J. Smith Welding, Inc. Other chemicals used were all from Sigma-Aldrich unless otherwise indicated.

### 2.3.2.2 Preparation of activated carbon fibers (ACFs)

The glass fibers were impregnated with a Novolac precursor (Novolac 4.17 g, hexamethylenetetramine 0.28 g, ethanol 100 ml) and placed in the hood overnight to be dried. The coated glass fibers were cured first by heating to 100 °C for 20 minutes to further remove solvent, then heated to 170 °C and kept at there for 3 hours. The samples were carbonized in flowing N<sub>2</sub> by heating to 600 °C (~10 °C /min) and then switching to CO<sub>2</sub>/H<sub>2</sub>O and holding for 5 hours. (The activation gas was generated by bubbling CO<sub>2</sub> through liquid water.) After activation, the ACFs were cooled in flowing N<sub>2</sub>. The samples were washed with deionized water and dried under vacuum at 120 °C for at least 12 hours before using.

### 2.3.2.3 Preparation of brominated ACFs

Three kinds of bromination processes were tried, involving the use of Br<sub>2</sub> vapor [56], impregnation of KBr solution and deposition by electrochemical reaction [57].

ACF was impregnated with KBr aqueous solution (10 wt%) for 30 minutes. After drying in the hood overnight, the samples were heated to 600°C for 5 hours. N<sub>2</sub> was used to maintain an oxygen free environment. Then the samples were washed with D. I. water and dried in the oven. The samples were identified as KBr-ACF.

The samples made from Br<sub>2</sub> vapor in a sealed glass tube were labeled as Br(v)-ACF. ACF was impregnated with liquid Br<sub>2</sub> overnight. After placing in the hood for 5 hours, the samples were placed in the furnace. N<sub>2</sub> was used to purge the furnace from room temperature to 400°C to maintain an oxygen free environment. At 400°C, N<sub>2</sub> flow was shut down and the samples reacted with bromine vapor in a sealed tube for 3 hours.



After the reaction, the tube was open and  $N_2$  again was allowed to flow to remove the excess  $Br_2$ . After cooling down to room temperature, the samples were washed with D. I. water and dried in the oven.

Another bromination method involved the electrochemical intercalation process (eBr-ACF). ACF was suspended in the electrolyte by a platinum wire, which served as the anode. While the platinum foil was used as the cathode and a 10 wt% KBr solution was used as the electrolyte. A battery of 9V was used, and after 6 hours of  $Br_2$  intercalation, the samples were washed with D. I. water and dried in the oven.

#### *2.3.2.4 Static mercury uptake test*

Static mercury capacity test was run by PPG Inc. The sample (8 cm\*8 cm) was suspended in a saturated mercury vapor in air at room temperature (~21 ng/mL). After two weeks, the weight change was measured assuming all the increased weight was attributed to Hg adsorption.

#### *2.3.2.5 Dynamic mercury adsorption test*

Dynamic mercury adsorption test was conducted at Nucon International. The test was performed by sending in radioactive mercury vapor at 2-4 ppb at 400°F at a volume flow rate of 2 liter per minute. Air was used to maintain vapor pressure of radioactive Hg. The sample size was around 6 cm in diameter, and Hg pick-up was analyzed by counting the gamma rays from radioactive mercury disintegration.

### 2.3.2.6 Characterization techniques

All the samples were initially heated at 120°C in a vacuum oven overnight to remove moisture and other adsorbed contaminants.

The amount of the carbonaceous material coated on glass fiber mat was measured using a Hi-Res TA instrument 2950 thermogravimetric analyzer (TGA) by burning off the coating in air at 750°C. The samples (10-20 mg) were heated at 10°C/min to 750°C, and held at that temperature for 30 min.

The analysis of surface area and average pore size was carried out with an Autosorb-1 apparatus (Quantachrome). All samples were outgassed at 150°C until the test of outgas pressure rise was passed by 5 µg Hg/min prior to their analysis. Nitrogen isotherm at 77K was used for further calculation. Nitrogen surface area was determined using the standard BET equation [52]. Average pore size and micropore volume were determined using the Dubinin-Radushkevich (DR) equations [53]. The volume of mesopores in the samples was calculated by subtracting the volume of micropores from the total pore volume at a relative pressure of 0.95.

A Model CE440 elemental analyzer (EA) was used to determine the C and H weight percentages in the samples. Bromine content was measured using inductively coupled plasma (OES Optima 2000 DV by Perkin Elmer). The oxygen contents were calculated by mass difference after combining the results of TGA and assuming the glass weight remain unchanged after burn-off and there were no other elements in the samples.

XPS (X-ray photoelectron spectroscopy) experiments were performed on Kratos Axis ULTRA. XPS spectra were obtained using an X-ray source operated at 13 kV and 10 mA. Survey scans were collected from 0-1100 eV with a pass energy of 160 eV. High-

resolution scans were performed with the pass energy adjusted to 40 eV. The pressure inside the vacuum system was maintained at approximately  $10^{-9}$  Torr during all XPS experiments. XPS spectra were analysed using a software called CasaXPS (Version 2.3.14). The carbon 1s electron binding energy was referenced at 284.5 eV for calibration [51].

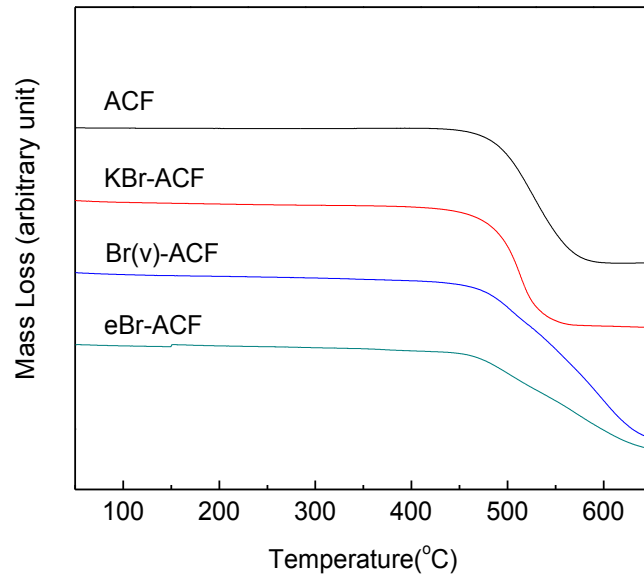
STM studies were carried out in a home built system in Prof. Joe Lyding's research group in University of Illinois at Urbana-Champaign with a base pressure of  $1.2 \times 10^{-8}$  Pa ( $9.0 \times 10^{-11}$  Torr). Topographic images were obtained in constant current mode using electrochemically etched W tips. The current and voltage used in this condition were 54 pA and 3.0 V, respectively. The sample size was 4 mm\*9.5 mm.

### **2.3.3 Results and discussions**

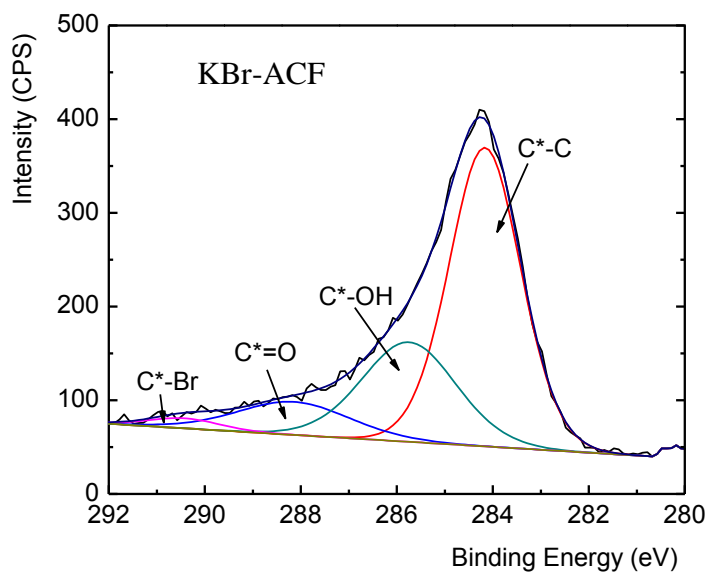
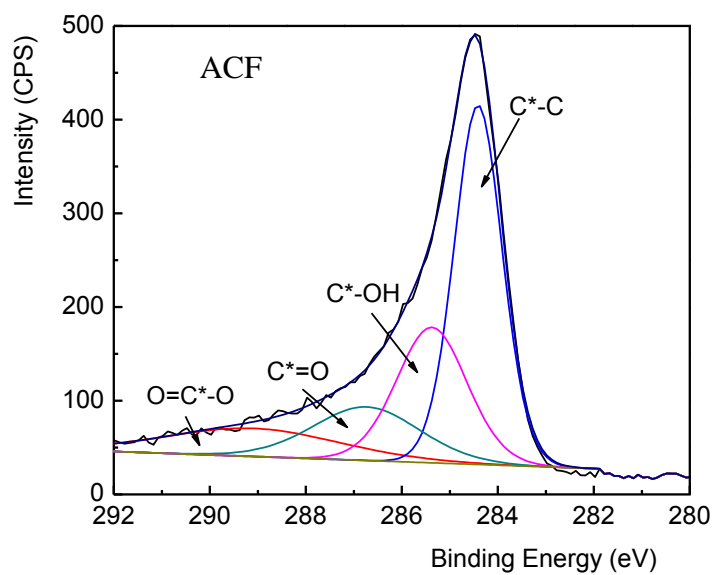
#### *2.3.3.1 Chemical structures of brominated activated carbon fibers (ACFs)*

Figure 2.11 shows TGA results of raw ACF and brominated ACFs. Usually there should be a weight loss around 100°C due to the desorption of the physically adsorbed water. However, since our samples are dried at 120°C in vacuum overnight before the measurement, it is reasonable that there is no weight loss around 100°C. At higher temperatures (480°C—620°C), the decomposition takes place owing to the burning out of surface carbon complexes [58]. Compared with raw ACF, all brominated samples including KBr-ACF, Br(v)-ACF and eBr-ACF show similar weight loss curves; this suggests that bromine atoms have been incorporated into the surface carbon matrix. If the bromine atoms exist in other forms, i.e. the bromine, other peaks corresponding to the loss of bromine should appear in the TGA curves.

The chemical structures of our samples were also investigated using XPS as shown in Figure 2.12. Originally raw ACF contained carbon-carbon groups (284.5 eV), carbon-hydroxyl groups (~285.5 eV), quinone groups (~287 eV) and carboxylic groups (~289 eV) [51,59]. After bromination processes, the peak corresponding to carbon-bromine groups which appears at 285.5~289.5 eV, such as in KBr-ACF, Br(v)-ACF and eBr-ACF. These results are consistent with previous TGA results showing that the bromine atoms have been incorporated into the carbon structure. At the same time, carboxylic and quinone groups disappear after bromination processes. This is reasonable since these groups have higher energy leading to a preference to react with bromine. Among these brominated ACFs, KBr-ACF has a unique chemical structure compared with the other two brominated samples. Besides the existence of carbon-bromine peak as expected, another new peak appears: normally, the carbanion groups corresponding to the binding energy of 281 – 283 eV. Probably the carbanion groups are formed by the strong interaction with KBr. Since carbanion groups are negatively charged, the positively charged potassium ions may still connect to these carbanion groups.



**Figure 2.11 TG curves of brominated ACFs**



**Figure 2.12 XPS spectra of brominated ACFs**

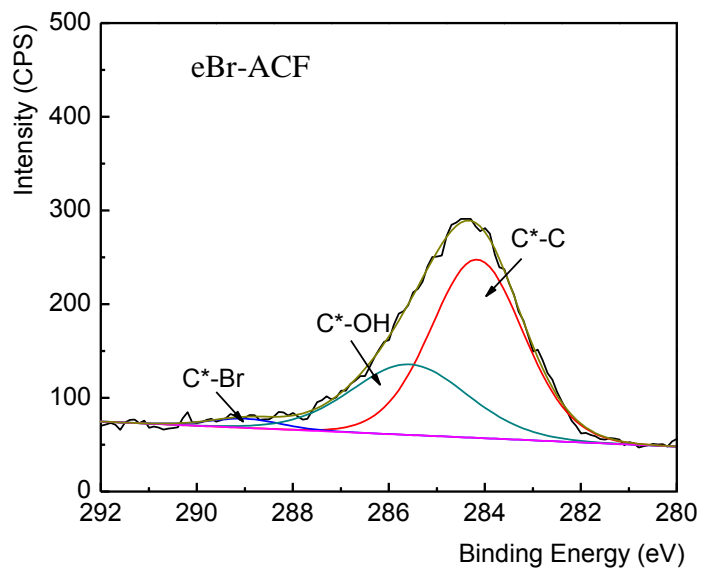
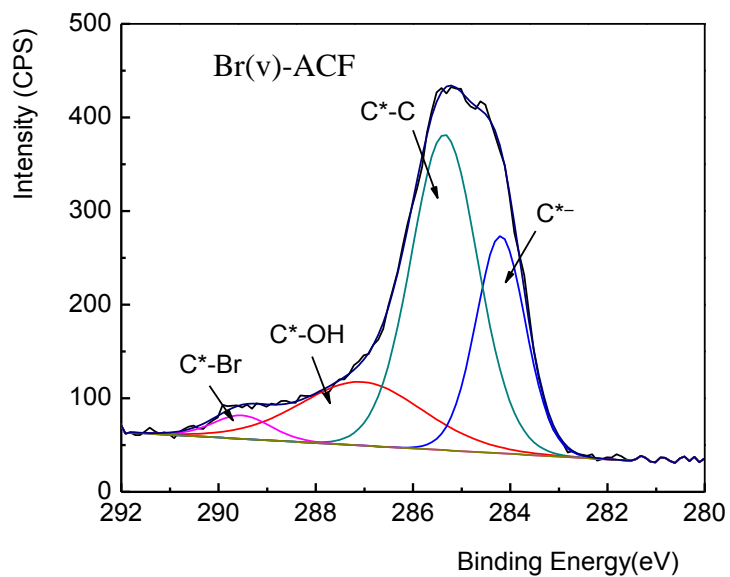


**Figure 2.12 XPS spectra of brominated ACFs (continued)**

### 2.3.3.2 Physical pore properties of brominated ACFs

The pore properties of brominated samples were also studied as shown in Table 2.6. Etching by CO<sub>2</sub>/H<sub>2</sub>O gas, ACF yields a highly porous structure with high specific surface areas. For KBr-ACF, the bromination process cause a decrease in surface area and pore

volume as compared with raw ACF. This is reasonable since micropores will benefit from the overlapping adsorption potentials of opposite pore walls, bromine groups would prefer to be attracted to micropores and block them while leaving the mesopores unreacted. This probably explains why brominated samples appear to have larger pores compared with raw ACF. Br(v)-ACF shows an even lower specific surface area and pore volume. In addition to the reasons we just mentioned, other reasons may include the specific bromination process of Br(v)-ACF. During the reaction between ACF samples and Br<sub>2</sub> vapor in a sealed furnace, most of the bromine attaches to the carbon matrix, while a small amount of carbon also likely reacts with the Br<sub>2</sub> vapor to give CBr<sub>4</sub>. This can result in partial structural collapse and a reduction in porosity and surface area. Unlike KBr-ACF and Br(v)-ACF, eBr-ACF has one unique feature, namely, a relatively large pore size. This is due to the intercalation of bromine groups in the electrochemical process. During the electrochemical process of eBr-ACF, at the ACF (anode) bromide ions form bromine, cluster together and intercalate within the graphite platelets, resulting in enlarged pores and higher pore volume. Therefore, the presence of micropores diminishes, leading to a lower surface area.

**Table 2.6 Porous structure characteristics of brominated samples**

	BET (m <sup>2</sup> /g)	average pore size (Å)	pore volume (cc/g)	Micro- pores	Meso- Pores
ACF	452	34	0.3900	63%	37%
KBr-ACF	359	40	0.3590	47%	53%
Br(v)-ACF	59	38	0.0562	60%	40%
eBr-ACF	124	244	0.7548	8%	92%



### 2.3.3.3 Static mercury uptake test

Figure 2.13 shows the static test results for Hg removal. As seen from this figure, all brominated samples show improved Hg uptake capacity compared with raw ACF. Thus, bromine containing groups appear to enhance mercury uptake capacities. Among these three kinds of samples, KBr-ACF is the most effective for Hg adsorption, as the mercury uptake capacity increases 15 times compared with the raw ACF to around 100 mg/g C. The second highest capacity is seen with Br(v)-ACF, where the mercury capacity is 64 mg/g C. eBr-ACF is the least effective with mercury uptake only half that of KBr-ACF.

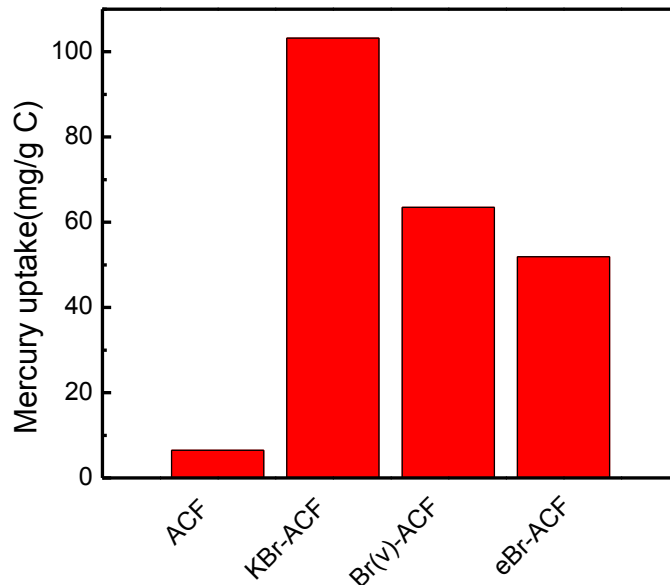


**Figure 2.13 Static mercury uptake capacities of brominated samples**

To study the effectiveness of all brominated samples on mercury removal, the elemental analyses results are shown in Table 2.7, trying to correlate the mercury uptake capacity with amount of bromine in the samples. The amount of oxygen is calculated by the difference of other elements, which may contain some amount of unburned ash. For

eBr-ACF, the total amount of carbon, hydrogen and bromine exceeds 100% probably due to experimental errors. For example, the error for elemental analysis is +/- 0.40%. And the error for TGA is +/- 0.2%. Additionally, since glass fiber substrate has a highly fluffy texture, the carbonaceous material may not uniformly coat on the substrate. The specific part of samples used for TGA analysis and elemental analysis may not have exactly the same amount of carbon on them. Originally, ACF consisted of 80 wt% carbon and 20 wt% oxygen. After bromination, 10 wt% to 20 wt% bromine is introduced into the samples based on the mass of coating content, as shown in Table 2.7. The bromine content based on coating content for KBr-ACF, Br(v)-ACF and eBr-ACF are 11.3 wt%, 15.5 wt% and 20.0 wt%, respectively. If the mercury adsorption is dominated by bromine groups present in activated carbon surface, mercury capacity should go as eBr-ACF > Br(v)-ACF > KBr-ACF. However, the actual results deviate from this trend.

**Table 2.7 Elemental analysis results of brominated samples**

	C (wt.%)	H (wt.%)	Br (wt.%)	O (wt.%)
ACF	76.6	0.9	none	22.5
KBr-ACF	74.0	0	11.3	14.7
Br(v)-ACF	56.9	0.3	15.5	27.3
eBr-ACF	82.5	0.9	20.0	-3.4

Referring to the chemical structures mentioned earlier in this paper, it is noted that compared with Br(v)-ACF and eBr-ACF, KBr-ACF has a unique chemical structure: the peak corresponding to the carbanion groups appears. As KBr-ACF shows much higher mercury uptake capacity compared with the other two brominated samples, it is probably caused by the presence of carbanion groups in KBr-ACF. For the negatively charged carbanion groups, the positively charged potassium ions may still connect to these

carbanion groups. Since potassium has a strong affinity to react with mercury and form amalgam, it is reasonable that KBr-ACF showed much higher mercury uptake capacity compared with the other two brominated samples although it only has 10 wt% of bromine.

Additionally, there is more bromine connecting to the carbon surface in KBr-ACF compared with Br(v)-ACF and eBr-ACF. This makes the bromine groups more accessible to mercury during the test, which provides another reason that KBr-ACF is more effective for mercury removal compared with the other two brominated samples.

As we can see here, besides the chemical structures, pore properties also play an important role on mercury adsorption performance. Usually, micropores are mainly responsible for mercury adsorption while mesopores may serve as transportation channels [31,54]. For KBr-ACF and Br(v)-ACF, both samples consist of almost equal amount of micropores and mesopores, it is reasonable that both samples have higher mercury uptake capacities compared with eBr-ACF. For eBr-ACF, the sample mainly consists of mesopores, hence Hg molecules would be easier to pass through rather than being captured. That explains why eBr-ACF has the lowest mercury uptake capacity although it has the highest amount of bromine. However, for ACF, although the sample consist of almost equal amount of micropores and mesopores, it does not have any specific chemical sites (bromine groups or carbanion groups in this case) to enhance mercury adsorption. Hence, the mercury uptake capacity for ACF is relatively low. Therefore, the Hg adsorption mechanism of bromine treated samples at room temperatures may be described as a combined function of chemical and physical interactions.

#### 2.3.3.4 *Dynamic mercury performance resultst*

The dynamic tests of mercury adsorption using radioactive Hg were also conducted for ACF and their brominated samples. The results of the dynamic tests are described below: there is almost no mercury adsorption for ACF. Br(v)-ACF and eBr-ACF have similar performances: a steady mercury removal of 30% to 33% which lasts up to 3 months. KBr-ACF has a dramatically higher mercury removal efficiency at the beginning of the experiment (over 90%), however, the mercury removal efficiency dropped to below 30% within a week.

Since the dynamic test was run at 400°F trying to mimic the flue gas temperature, the mechanism for mercury adsorption is different from that conducted at room temperatures. At 400°F, chemical structure would play a more important role for mercury adsorption since physical adsorption capability will decrease due to desorption. On the other hand, mercury adsorption at room temperature is attributed to both chemisorption and physisorption [60].

Therefore, it is reasonable that raw ACF has almost no adsorption of mercury since it has no specific chemical sites and mainly depends on physical pore properties for Hg adsorption. For KBr-ACF, it has dramatically high mercury removal efficiency initially (over 90%) due to the contributions of both bromine groups and carbanion groups. However, carbanion groups are not very stable in air, they may be oxidized and form carbon connecting with oxygen containing groups (i.e. hydroxyl, carboxylic or quinone), causing a loss in mercury adsorption performance within a week.

Both Br(v)-ACF and eBr-ACF show stable mercury adsorption performances up to 3 months. The experiments were stopped not because the samples reached their

equilibrium but because 3 months is relatively long for a field test. Hence, these samples may show stable performance for an even longer period of time. The steady maximum removal of 30% mercury is probably limited by the mass transfer zone caused by the short resident time during the test. Although 30% of mercury removal efficiency does not seem very impressive at first glance, the whole mercury removal efficiency may add up to over 90% since a bag house has tens of layers of fabric filters and our results are only based on one layer. Additionally, since Br(v)-ACF and eBr-ACF showed stable performances over a long period of time (up to 3 months), these two brominated samples show great potential for bag house usage which normally need to be replaced every two to three years. Also, this combined system with bag house may remove Hg and fly ash simultaneously without changing the whole power plant configuration.

Although our studies show that Br-containing functional groups play an important role for mercury adsorption, the mechanism of Br-containing functional groups interacting with Hg is still not clear yet. According to studies on mercury adsorption of Cl-contained activated carbon [35,61], formation of oxidized mercury complexes (e.g.  $[\text{HgCl}]^+$ ,  $[\text{HgCl}_2]$  and  $[\text{HgCl}_4]^{2-}$ ) was confirmed. Therefore, we propose a similar mechanism involving the mercury oxidation using Br-contained activated carbon fibers as shown in Figure 2.14.

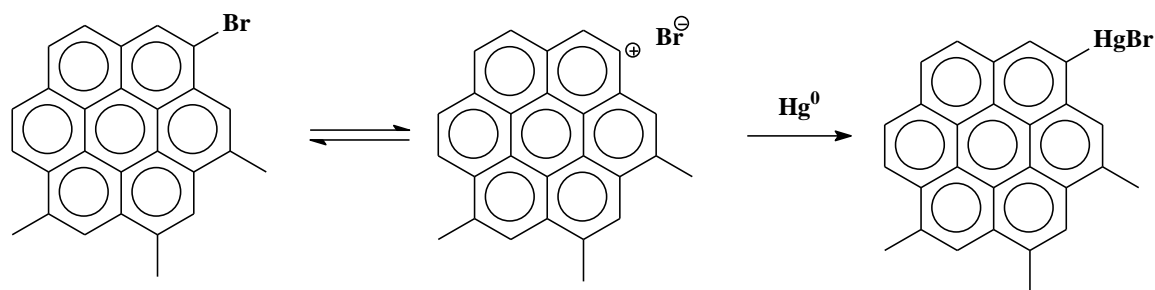


**Figure 2.14 A possible mechanism for Hg adsorption using Br-containing group**

#### 2.3.3.5 Morphology study

During the activation process, CO<sub>2</sub>/H<sub>2</sub>O gases etch the edges of carbonaceous material, creating a random (but locally semi-organized) number of graphite platelets [26]. Our ACF and brominated samples have highly porous structures. The STM image of raw ACF is shown in Figure 2.15. The image is not very clear due to noise contamination caused by ambient electromagnetic interference, but it still shows the morphology of a raw ACF. Seen from Figure 2.15, in the carbon matrix, lots of graphite platelets are formed by the etching, while micropores and mesopores are formed between these platelets.

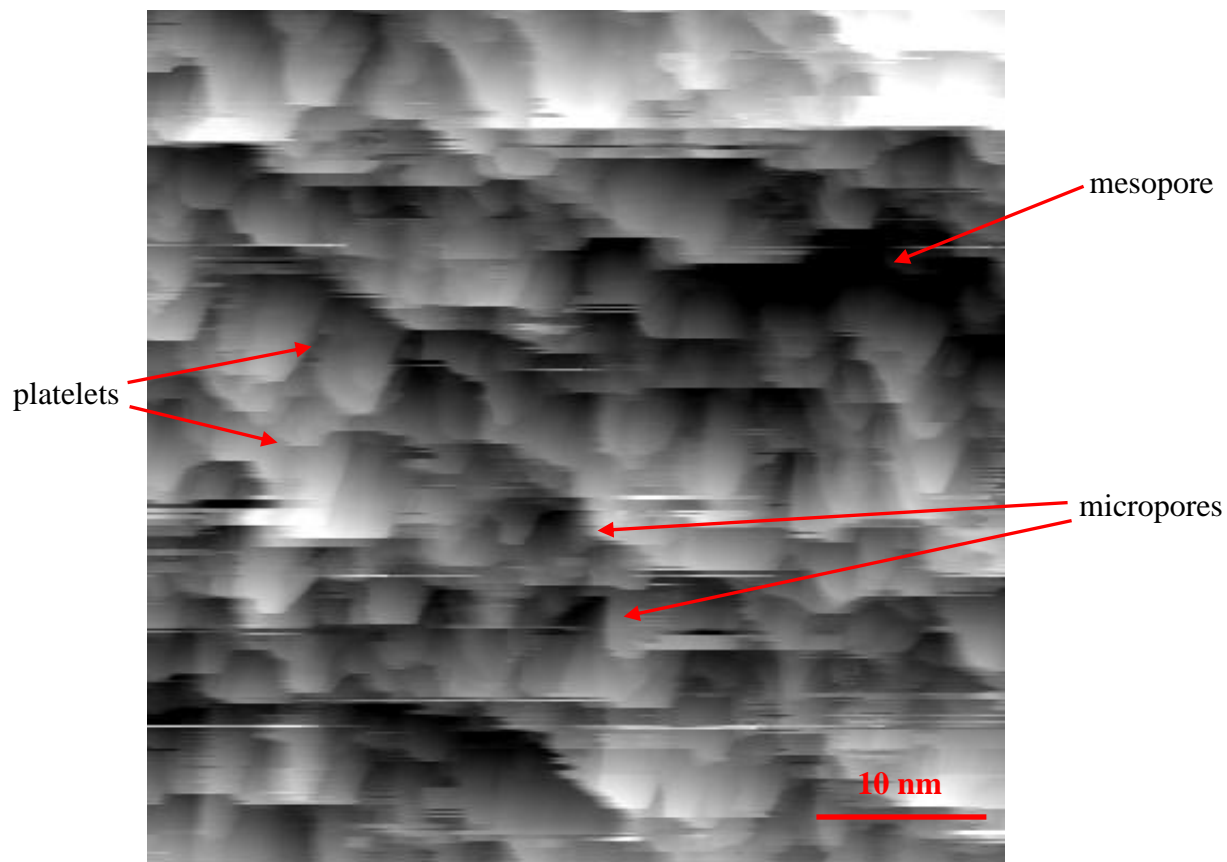


**Figure 2.15 STM image of original ACF**

### **2.3.4 Conclusions**

The mechanism for mercury adsorption is still not well understood yet. Based on our studies, mercury adsorption is attributed to both chemisorption and physisorption at room temperature while chemical structure plays a more important role at 400°F. The incorporation of bromine groups appears to facilitate the oxidation process of Hg and hence increases the mercury adsorption performance. For the brominated samples treated with Br<sub>2</sub> vapor and the electrochemical method, stable mercury adsorption performances (30% to 33% removal) are observed up to 3 months. Although 30% of mercury removal efficiency does not seem very impressive at first glance, the whole mercury removal

efficiency may add up to over 90% since a bag house has tens of layers of fabric filters and our results are only based on one layer. Additionally, the mercury adsorption performance tests are stopped after 3 months not because the samples reach their equilibrium but because 3 months is relatively long for an experiment. Hence, these two brominated samples are very promising for commercial applications of bag house. Also, this combined bag house system may remove Hg and fly ash simultaneously without changing the whole power plant configuration.

## **2.4 Design of chemically activated carbon fibers (CAFs) for mercury removal**

### **2.4.1 Overview**

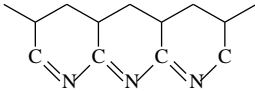
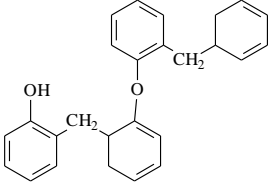
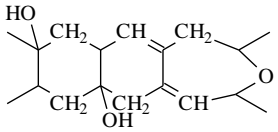
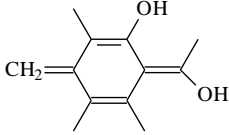
In Section 2.2 and Section 2.3, we have described the use of chemical modifications on ACFs to enhance mercury removal properties. However, these processes include two steps: namely synthesis of ACFs followed by chemical treatments. To simplify the process, another method called chemically activated carbon fibers (CAFs) is going to be explored in this Chapter. Chemical activation can also produce a high surface area organic material onto the glass fiber substrate [62,63,64]. To create the porous structure in CAFs, activation agents such as  $\text{ZnCl}_2$ ,  $\text{H}_3\text{PO}_4$  etc. are needed. This is different from the pore formation mechanism in ACFs. During the process of forming the ACFs, the porous structure is formed by etching using  $\text{CO}_2/\text{H}_2\text{O}$ . Compared with ACFs, the process of making CAFs is carried at a much lower temperature ranging from  $250^\circ\text{C}$  to  $400^\circ\text{C}$ . The CAF sample also shows a higher yield and controlled pore size distribution. This kind of process could be applied to a variety of polymers including phenolic, polyacrylonitrile (PAN), polyvinyl alcohol (PVA) and Cellulose. The chemical



structures of low temperature chemically activated carbon fibers made from a variety of polymers are summarized in Table 2.8.

For our experiments, two CAF samples were prepared using Novolac and PAN as the precursor polymers. Compared with ACF, the mercury uptake capacities for these two CAFs increase 15 to 20 times. For Novolac based CAF, the functional groups remained in the adsorbent structure may facilitate the mercury uptake process [65]. For PAN based CAF, the nitrogen incorporated into the aromatic ring structure could produce electropositive sites, which could catalyze mercury oxidation and result in higher mercury uptake capacity [13]. The chemical and physical properties of these samples will be discussed in more details later in this Section.

**Table 2.8 Chemical structures of low temperature chemically activated carbon fibers**

Resin	Activation Agent	Activation Temp. (°C)	Surface Area (m <sup>2</sup> /g coating)	Yield (wt %)	Structure
PAN	ZnCl <sub>2</sub>	400	1000	90	
Phenolic	ZnCl <sub>2</sub>	400	1200	80	
PVA	H <sub>3</sub> PO <sub>4</sub>	250	1600	60	
Cellulose	ZnCl <sub>2</sub>	400	2500	35	

## 2.4.2 Experimental

### 2.4.2.1 Materials

Glass fibers were provided by PPG Industrial. Novolac resin 2074 was obtained from Georgia Pacific. All the gases, N<sub>2</sub>, Cl<sub>2</sub>, CO<sub>2</sub> gas were lab grade from S.J. Smith Welding, Inc. Other chemicals used were all from Sigma-Aldrich unless otherwise indicated.

#### 2.4.2.2 Preparation of activated carbon fibers (ACFs)

The glass fibers were impregnated with a Novolac precursor (Novolac 4.17 g, hexamethylenetetramine 0.28 g, ethanol 100 ml) and placed in the hood overnight to be dried. The coated glass fibers were cured first by heating to 100 °C for 20 minutes to further remove solvent, and then heated to 170 °C and kept there for 3 hours. The samples were carbonized in flowing N<sub>2</sub> by heating to 600 °C (~10 °C /min) and then switching to CO<sub>2</sub>/H<sub>2</sub>O and holding for 5 hours. (The activation gas was generated by bubbling CO<sub>2</sub> through liquid water.) After activation, the ACFs were cooled in flowing N<sub>2</sub>. The samples were washed with deionized water and dried under vacuum at 120 °C for at least 12 hours before usage.

#### 2.4.2.3 Preparation of chemically activated carbon fibers (CAFs)

Nov-CAF was made using a Novolac precursor. The glass fibers were coated a Novolac precursor (Novolac 7.50 g, ZnCl<sub>2</sub> 1.18 g, ethanol 100 ml) and placed in the hood overnight to be dried. The coated glass fibers were cured first by heating to 80°C for 20 minutes to further remove solvent, then heating to 170°C and isothermed at 170°C for 6 hours. The samples were activated in flowing N<sub>2</sub> by heating them to 400°C and holding that temperature constant for 30 min. After cooling in flowing N<sub>2</sub>, the samples were thoroughly washed with deionized water, followed by thorough washing with 0.5 M HCl and rinsing with deionized water.

Another method for preparing low temperature chemically activated carbon fibers uses PAN as the precursor (PAN-CAF). PAN was first dissolved in DMF at 70°C with electromagnetic stirring; and ZnCl<sub>2</sub> was then added to the solution at ambient

temperature. (PAN 1.6 wt%, ZnCl<sub>2</sub> 4.7 wt%). The coated glass fibers were passed through a bath containing a 5 wt% ZnCl<sub>2</sub> aqueous solution at room temperature, in order to remove the DMF and to better coagulate the PAN coating. The coated glass fibers were dried in the hood overnight, cured by first heating to 100°C for 20 minutes and then stabilized at 200°C for 6 h. The samples were activated in flowing N<sub>2</sub> by heating at ~10°C/min to 400°C and holding at that temperature for 30 min. After cooling in flowing N<sub>2</sub>, the samples were thoroughly washed with deionized water, followed by thorough washing with 0.5 M HCl and rinsing with deionized water. Then the samples were transferred to a vacuum oven at 120°C for at least 12 h.

#### *2.4.2.4 Static mercury uptake test*

Static mercury capacity test was run by PPG Inc. The sample (8 cm\*8 cm) was suspended in a saturated mercury vapor in air at room temperature (~21 ng/mL). After two weeks, the weight change was measured assuming all the increased weight was attributed to Hg adsorption.

#### *2.4.2.5 Characterization techniques*

All the samples were initially heated at 120°C in a vacuum oven overnight to remove moisture and other adsorbed contaminants.

The amount of the carbonaceous material coated on glass fiber mat was measured using a Hi-Res TA instrument 2950 thermogravimetric analyzer (TGA) by burning off the coating in air at 750°C. The samples (10-20 mg) were heated at 10°C/min to 750°C, and held at that temperature for 30 min.

The analysis of surface area and average pore size was carried out with an Autosorb-1 apparatus (Quantachrome). All samples were outgassed at 150°C until the test of outgas pressure rise was passed by 5 µg Hg/min prior to their analysis. Nitrogen isotherm at 77K was used for further calculation. Nitrogen surface area was determined using the standard BET equation [52]. Average pore size and micropore volume were determined using the Dubinin-Radushkevich (DR) equations [53]. The volume of mesopores of the samples was calculated by subtracting the volume of micropores from the total pore volume at a relative pressure of 0.95.

A Model CE440 elemental analyzer (EA) was used to determine the C, H and N weight percentages in the samples. The oxygen content was calculated by mass difference after combining the results of TGA and assuming the glass weight remain unchanged after burn-off and there were no other elements in the samples.

XPS (X-ray photoelectron spectroscopy) experiments were performed on Kratos Axis ULTRA. XPS spectra were obtained using an X-ray source operated at 13 kV and 10 mA. Survey scans were collected from 0-1100 eV with a pass energy of 160 eV. High-resolution scans were performed with the pass energy adjusted to 40 eV. The pressure inside the vacuum system was maintained at approximately  $10^{-9}$  Torr during all XPS experiments. XPS spectra were analysed using a software called CasaXPS (Version 2.3.14). The carbon 1s electron binding energy was referenced at 284.5 eV for calibration [51].

pH testing of the various samples was measured using the ASTM method D1512-93. First, the carbon samples were crushed into fine powder and dried. 0.5 g of carbon was weighed and placed into a 100 mL beaker. Next, 50 mL of boiling deionized water

was added along with 3 drops of acetone to facilitate the wetting of the sample. The beaker was covered with a watch glass and the mixture kept boiling for another 15 min. After that, the mixture was then allowed to cool down to room temperature and pH values were obtained using pH meter.

### 2.4.3 Results and discussions

#### 2.4.3.1 Static mercury uptake capacities

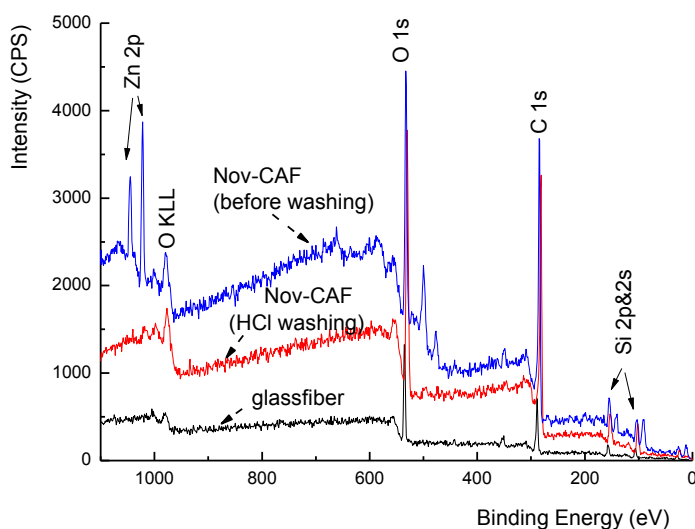
Table 2.9 shows the mercury uptake of PAN and novolac based CAFs. Compared with ACF, the mercury uptake capacities have increased dramatically, up to over 15 times. Especially for PAN-CAF, the mercury uptake is around 120 mg/g C, even 1 to 2 orders higher than the sulfur-treated and brominated ACFs described in Section 2.2 and Section 2.3. As mentioned earlier in this thesis, mercury uptake capacities at room temperature is a co-function of both chemical structure and physisorption, further discussion on these two properties will be discussed later in this Section.

	ACF	Nov-CAF	PAN-CAF
Hg uptake (mg/g C)	6.5	83.5	117.3

#### 2.4.3.2 Chemical structures of CAFs

It is reported that  $ZnCl_2$  may also play a role in mercury removal [35,61]. Since  $ZnCl_2$  is used in our experiments as reactive agents, we need to confirm that the increased mercury uptake for CAFs is not attributed to the residual  $ZnCl_2$  remained in the final products. Figure 2.16 shows XPS spectrum of Nov-ACF before and after washing by HCl. Before washing, the peaks corresponding to  $ZnCl_2$  (1022 and 1045 eV [51]) show

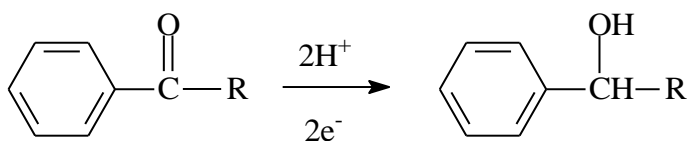
up in the spectrum. However, after washing by HCl, these two peaks diminished, indicating that there is no residual  $\text{ZnCl}_2$  left in the final products. A similar phenomenon is observed for PAN-ACF, no residual  $\text{ZnCl}_2$  is observed after washing by dilute 0.5 M HCl solution. Hence, these relatively large mercury uptake capacities of CAFs are not attributed to  $\text{ZnCl}_2$  but surface functional groups on the adsorbents. In this case, surface functional groups of both Nov-CAF and PAN-CAF need to be investigated.



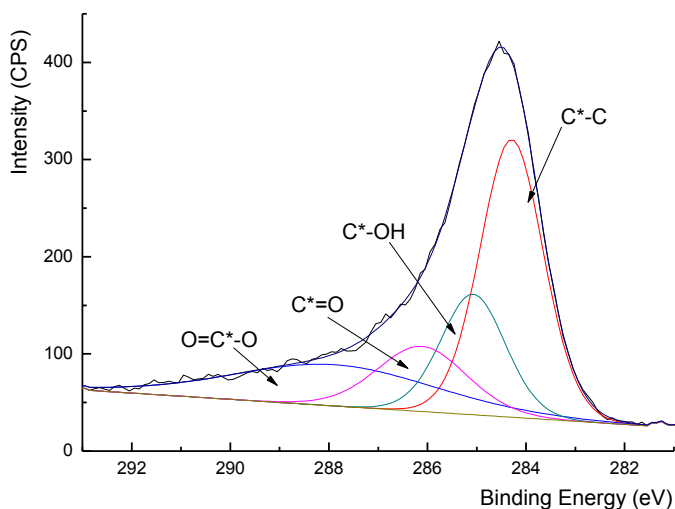
**Figure 2.16 XPS of Nov-ACF before and after washing by HCl**

Figure 2.17 shows the high-resolution C 1s spectra of Nov-CAF. Similar to ACFs, the Nov-CAF also contains carbon-carbon groups (284.5 eV), carbon-hydroxyl groups (~285.5 eV), carbonyl groups (~287 eV) and carboxylic groups (~289 eV) [51,59]. However, the concentrations of the surface functional groups vary. Compared with ACF, Nov-CAF have more carboxylic groups, while ACF have more hydroxyl groups based on data from Table 2.10. The possible mechanism involving oxygen surface functional groups is likely an electron transfer process in which the carbon surfaces may act as an

electrode for  $\text{Hg}^0$  oxidation [65]. Among these oxygen surface functional groups, both carbonyl and carboxylic groups are likely to be the active sites for mercury adsorption. Both groups are reducible groups on the carbon surfaces [30], for example, the reactions could be expressed as followed:



During the reduction process, carbonyl and carboxylic groups can act as electrodes to accept electrons for  $\text{Hg}^0$  oxidation and facilitate the mercury adsorption process. On the other hand, hydroxyl groups may inhibit mercury oxidation process or affect the equilibrium concentrations of carbonyl or carboxylic groups. Therefore, it is reasonable that Nov-CAF has 15 times higher mercury uptake capacity compared with ACF due to the higher amount of carbonyl and carboxylic groups but lower amount of hydroxyl groups in Nov-CAF than in ACF.



**Figure 2.17 C 1s of Nov-CAF**



**Table 2.10 Percentages of functional groups derived from XPS for ACF and Nov-CAF**

mass	C-C (wt.%)	Hydroxyl (wt.%)	Carbonyl (wt.%)	Carboxylic (wt.%)
ACF	46.22	25.55	15.27	12.95
Nov-CAF	44.35	19.69	14.71	21.25

Figure 2.18 High-resolution C 1s and N 1s spectra of PAN-CAF shows the high-resolution C 1s and N 1s spectra of PAN-CAF. The surface oxygen functional groups on carbon also contain carbon-carbon groups (284.5 eV), carbon-oxygen groups (~285.5 eV), carbonyl and carboxylic groups (~289 eV). Besides those oxygen containing surface functional groups, there is also nitrogen groups incorporated into the aromatic ring structure including pyridinic, pyrrolic and quaternary structures. The nitrogen incorporated into the aromatic ring structure could produce electropositive sites, facilitate mercury oxidation process and hence a better mercury uptake capacity [13]. This probably explains why PAN-ACF has an even higher mercury uptake capacity compared with Nov-CAF.

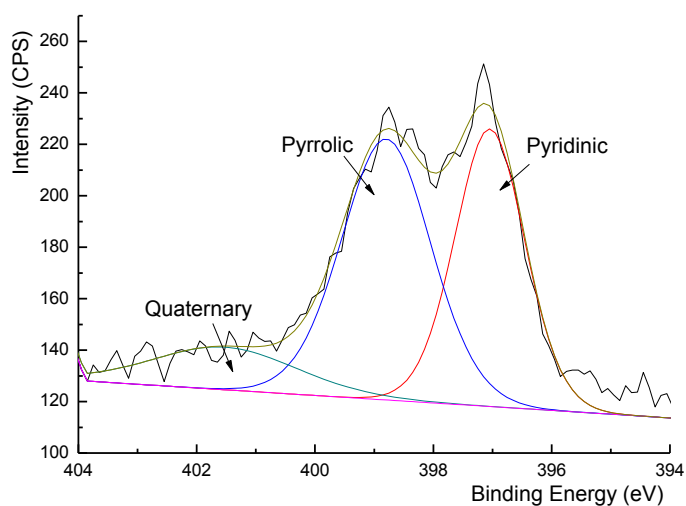
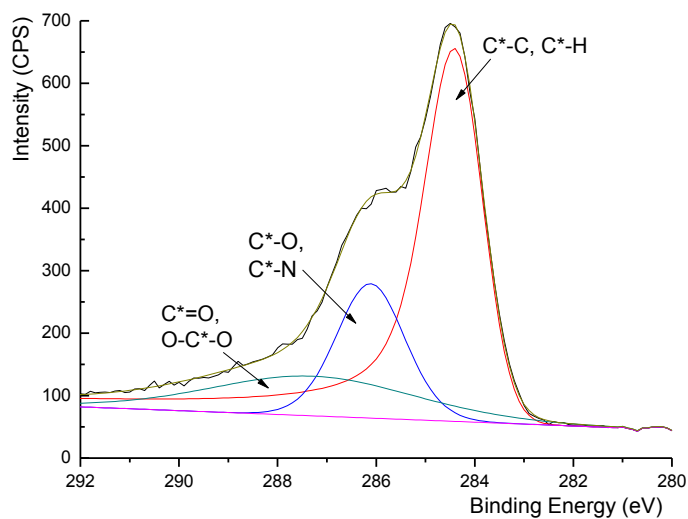


**Figure 2.18 High-resolution C 1s and N 1s spectra of PAN-CAF**

#### 2.4.3.3 Physical pore properties

The pore properties of CAF samples were also studied as shown in Table 2.11. For ACF, the porous structure is obtained by etching using oxidative gases. On the other hand, the pores in CAFs are created by activation agents. The activation agents are dissolved in the precursors, coated on the glass fiber along with the precursors, remained

in the coating after activation process, and then washed out to leave the pores in the final product. By using chemically activation process, we can also get a highly porous structure with a high yield, such as Nov-CAF. For PAN-CAF, since the precursor solution is more viscous than that of ACF, it is more difficult for precursor to diffuse through the mat, resulting in an incomplete activation process and hence a lower surface area in the final product compared with Nov-CAF.

Besides the chemical structure, pore properties should also be considered in mercury adsorption. Generally, micropores are considered as the active sites for mercury adsorption while mesopores act as transport routes [30]. Both PAN-CAF and Nov-CAF have almost equal amount of micropores and mesopores, their pore properties provide another reason why PAN-CAF and Nov-CAF show good mercury adsorption performance. However, for ACF, although it also has similar pore properties, the chemical structures inhibit its mercury uptake capacity. Therefore, the mercury adsorption is attributed to both physical pore properties and chemical structures.

**Table 2.11 Physical pore properties of CAF samples**

	Specific surface area (m <sup>2</sup> /g)	Average pore size (Å)	Pore volume (ml/g)	Micropores	Mesopores
ACF	452	34	0.3900	63%	37%
PAN-CAF	162.5	45	0.1825	48%	52%
Nov-CAF	305	35	0.2658	50%	50%

#### 2.4.3.4 pH tests

The pH values of CAF samples are shown in Table 2.12. All the samples have slightly acidic surfaces due to the carboxylic groups on the adsorbents. Although these samples have difference concentration of carboxylic groups, there are almost no differences of pH values between these samples. This is probably because the dilution of

carbon in deionized water and partial dissociation of weak carboxylic groups alleviate the differences of carboxylic concentrations on adsorbent surfaces, resulting in the same order of  $H^+$  concentrations in the sludges and hence similar pH values.

**Table 2.12 pH values of CAF samples**

	ACF	PAN-CAF	Nov-CAF
pH	5.576	5.192	5.642

#### 2.4.4 Conclusions

Low temperature chemically activated samples also show good mercury adsorption properties, approximately one order higher than the sulfur treated ACFs described in Chapter 3 and comparable to the brominated ACFs described in Chapter 4: 117.3 mg/g C for PAN-CAF and 83.5 mg/g C for Nov-CAF. Additionally, activation process for CAF is simplified compared with the methods used for the chemical treatments following the synthesis of ACFs. Hence, CAF provides a great potential for applications such as mercury adsorption.

Between Nov-CAF and PAN-CAF, Nov-CAF is easier to be dealt with since ethanol is used to make the precursor solution instead of DMF and no heat is needed for the dissolution. Additionally, novolac is cheaper than PAN as a raw material. Therefore, Nov-CAF is more promising for possible scaling-up. Besides Nov-CAF and PAN-CAF, other inexpensive polymers can be used as precursors such as PVA and cellulose. In future, CAFs based on cheaper polymers can be studied and CAF may provide a new direction for mercury adsorption.

## 2.5 References

- [1] G. Liu, Y. Cai, N. O'Driscoll, *Environmental Chemistry and Toxicology of Mercury*, John Wiley and Sons, Inc., New Jersey, 2010.
- [2] T.W. Clarkson, L. Magos, The toxicology of mercury and its chemical compounds, *Crit. Rev. Toxicol.* 36 (2006) 609-662.
- [3] N.E. Selin, Global biogeochemical cycling of mercury: a review, *Annu. Rev. Environ. Resour.* 34 (2009) 43–63.
- [4] S.G. Gilbert, *A small dose of toxicity: the health effects of common chemicals*, 2nd Edition, Healthy World Press, 2009.
- [5] B.C. Scudder, L.C. Chasar, D.A. Wentz, N.J. Bauch, M.E. Brigham, P.W. Moran, D.P. Krabbenhoft, *Mercury in fish, bed sediment, and water from streams across the United States: 1998–2005*, U.S. Geological Survey Scientific Investigations Report, 2009, 2009-5109.
- [6] A.T. Chalmers, D.M. Argue, D.A. Gay, M.E. Brigham, C.J. Schmitt, D.L. Lorenz, Mercury trends in fish from rivers and lakes in the United States: 1969–2005, *Environ. Monit. Assess.* 175 (2011) 175-191.
- [7] M.F. Wolfe, S. Schwarzbach, R.A. Sulaiman, Effects of mercury on wildlife: a comprehensive review, *Environ. Toxicol. Chem.* 17 (1998) 146–160.
- [8] A.M. Scheuhammer, M.W. Meyer, M.B. Sandheinrich, M.W. Murray, Effects of environmental methylmercury on the health of wild birds, mammals, and fish, *AMBIO: A. J. Hum. Environ.* 36 (2007) 12–19.
- [9] M. Harada, Minamata disease: methylmercury poisoning in Japan caused by environmental pollution. *Crit. Rev. Toxicol.* 25 (1995) 1–24.
- [10] US Environ. Prot. Agency (EPA), Water quality criterion for the protection of human health: methylmercury, Rep. EPA-823-R-01-001, 2001.
- [11] [http://www.mercury.utah.gov/atmospheric\\_transport.htm](http://www.mercury.utah.gov/atmospheric_transport.htm) (Retrieved by March, 2013)
- [12] R. Strivastava, *Control of Mercury Emissions from Coal Fired Electric Utility Boilers: An Update*. U.S. Environmental Protection Agency: Research Triangle Park, NC, 2005.

- [13] J.H. Pavlish, E.A. Sondreal, M.D. Mann, E.S. Olson, K.C. Galbreath, D.L. Laudal, S.A. Benson, Status review of mercury control options for coal-fired power plants, *Fuel Process. Technol.* 82 (2003) 89-165.
- [14] R.H. Perry, D. Green, Perry's Chemical Engineers' Handbook, 8th edition, McGraw-Hill Companies, Inc., NY, 2007.
- [15] US Environ. Prot. Agency (EPA), Study of hazardous air pollutant emissions from electric utility steam generating units: final report to Congress, EPA-453/R-98-004a, 1998.
- [16] E.G. Pacyna, J.M. Pacyna, K. Sundseth, J. Munthe, K. Kindbom, S. Wilson, F. Steenhuisen, P. Maxson, Global emission of mercury to the atmosphere from anthropogenic sources in 2005 and projections to 2020, *Atmos. Environ.* 44 (2010) 2487-2499.
- [17] US Environ. Prot. Agency (EPA), Reconsideration of certain new source and startup/shutdown issues: national emission standards for hazardous air pollutants from coal- and oil-fired electric utility steam generating units and standards of performance for fossil-fuel-fired electric utility, industrial-commercial-institutional, and small industrial-commercial-institutional steam generating units, *Federal Register*, 2012 (77) 71323-71344, FR Doc. 2012-28892.
- [18] C.D. Copper, F.C. Alley, Air Pollution Control: A Design Approach (4th Edition), Waveland Press Inc., IL, 2011.
- [19] T.J. Feeley, L.A. Brickett, A. O'Palko, Field testing of mercury control technologies for coal-fired power plants, DOE/NETL Mercury R&D Program Review, U.S. DOE, May 2005.
- [20] H. Yang, Z. Xu, M. Fan, A.E. Bland, R.R. Judkins, Adsorbents for capturing mercury in coal-fired boiler flue gas, *J. Hazard. Mater.* 146 (2007) 1-11.
- [21] T.R. Carey, O.W. Hargrove, C.F. Richardson, Factors affecting mercury control in utility flue gas using activated carbon, *J. Air Waste Manage. Assoc.* 48 (1998) 1166-1174.
- [22] J.R. Morency, T. Panagiotou, C.L. Senior, Zeolite sorbent that effectively removes mercury from flue gases, *Filtrat. Sep.* 39 (2002) 24-26.
- [23] S.D. Serre, G.D. Silcox, Adsorption of elemental mercury on the residual carbon in coal fly ash, *Ind. Eng. Chem. Res.* 39 (2000) 1723-1730.

- [24] G.E. Dunham, R.A. DeWall, C.L. Senior, Fixed-bed studies of the interactions between mercury and coal combustion fly ash, *Fuel Process. Technol.* 82 (2003) 197-213.
- [25] S.B. Ghorishi, C.B. Sedman, Low concentration mercury sorption mechanisms and control by calcium-based sorbents: application in coal-fired processes, *J. Air Waste Manage. Assoc.* 48 (1998) 1191-1198.
- [26] H. Marsh, F. Rodriguez-Reinoso, *Activated Carbon*, Elsevier, London, 2006.
- [27] G.M. Roy, *Activated Carbon Applications in the Food and Pharmaceutical Industries*, Technomic Publishing Company, PA, 1995.
- [28] M.B. Rao, R.G. Jenkins, Molecular dimensions and kinetic diameters for diffusion for various species, *Carbon*, 25 (1987) 445-446.
- [29] S.V. Moore, D.L. Trimm, The preparation of carbon molecular sieves by pore blocking, *Carbon*, 15 (1977) 177-180.
- [30] R.C. Bansal, M. Goyal, *Activated Carbon Adsorption*, Taylor and Francis Group, UK, 2005.
- [31] M.M. Valer-Maroto, Y. Zhang, G.J. Evan, T. Zhong, H.W. Pennline, Effect of porous structure and surface functionality on the mercury capacity of a fly ash carbon and its activated sample, *Fuel* 84 (2005) 105-108.
- [32] J. Wu, J. Chen, S. Zhang, P. He, J. Fang, Y. Wu, Removal of gas-phase elemental mercury by bromine-impregnated activated carbon, *Adv. Mater. Res.* 356-360 (2012) 1660-1663.
- [33] W. Liu, R.D. Vidic, T.D. Brown, Optimization of sulfur impregnation protocol for fixed-bed application of activated carbon-based sorbents for gas-phase mercury removal, *Environ. Sci. Technol.* 32 (1998) 531-538.
- [34] H. Hsi, M.J. Rood, Effects of sulfur impregnation temperature on the properties and mercury adsorption capacities of activated carbon fibers (ACFs), *Environ. Sci. Technol.* 35 (2001) 2785-2791.
- [35] H. Zeng, F. Jin, J. Guo, Removal of elemental mercury from coal combustion flue gas by chloride-impregnated activated carbon, *Fuel* 83 (2004) 143-146.
- [36] S.B. Ghorishi, R.M. Keeney, S.D. Serre, Development of a Cl-impregnated activated carbon for enhanced-flow capture of elemental mercury, *Environ. Sci. Technol.* 36 (2002) 4454-4459.

- [37] Apogee Scientific Inc. Assessment of Low Cost Novel Sorbents for Coal-Fired Power Plant Mercury Control, Final Report, DE-FC26-01NT41180, 2004.
- [38] C.L. Mangun, Z. Yue, J. Economy, Adsorption of organic contaminants from water using tailored ACFs, *Chem. Mater.* 13 (2000) 2356-2360.
- [39] J. Economy, M. Daley, Coated adsorbent fibers, US Patent 5834114, 1998.
- [40] W.H. Schroeder, Sampling and analysis of mercury and its compounds in the atmosphere, *Environ. Sci. Technol.* 16 (1982) 394-400.
- [41] Arizona Instrument LLC, User manual: JEROME® J405 Mercury Vapor analyzer, AZ, 2013.
- [42] H.H. Willard, L.L. Merritt, J.A. Dean, F.A. Settle, Instrumental Methods of Analysis, Wadsworth Publishing Company, 1988.
- [43] J.W. Anthony, R.A. Bideaux, K.W. Bladh, M.C. Nichols, Handbook of Mineralogy, Mineralogical Society of America, VA, 2003.
- [44] US Environ. Prot. Agency (EPA), Mercury Releases and Spills, <http://www.epa.gov/mercury/spills/index.htm>. (Retrieved March 2013).
- [45] W. Feng, E. Borguet, R.D. Vidic, Sulfurization of carbon surface for vapor phase mercury removal – I: Effect of temperature and sulfurization protocol, *Carbon* 44 (2006) 2990–2997.
- [46] W. Feng, E. Borguet, R.D. Vidic, Sulfurization of a carbon surface for vapor phase mercury removal – II: Sulfur forms and mercury uptake, *Carbon* 44 (2006) 2998–3004.
- [47] H. Hsi, M.J. Rood, M. Rostam-Abadi, Mercury adsorption properties of sulfur-impregnated adsorbents, *J. Environ. Eng.* 128 (2002) 1080-1089.
- [48] H. Hsi, S. Chen, M. Rostam-Abadi, Preparation and evaluation of coal-derived activated carbons for removal of mercury vapor from simulated coal combustion flue gases, *Energy Fuels* 12 (1998) 1061-1070.
- [49] V.A. Durante, Z. Xu, G.S. Shealy, Capture of mercury from a gasous mixture containing mercury, International Patent WO 2007/056478 A1, 2007.
- [50] Y. Liu, S. Xie, Y. Li, Y. Liu, Novel mercury control technology for solid waste incineration: sodium tetrasulfide (STS) as mercury capturing agent, *Environ. Sci. Technol.* 41 (2007) 1735-1739.



- [51] J.F. Moulder, W.F. Stickle, P.E. Sobol, K.D. Bomben, J. Chastain. Handbook of X-ray photoelectron spectroscopy, Perkin-Elmer Corporation, Eden Prairie, MN, 1992.
- [52] S. Brunauer, P.H. Emmett, E. Teller, Adsorption of gases in multimolecular layers, *J. Am. Chem. Soc.* 60 (1938) 309-319.
- [53] B. McEnaney, Estimation of the dimensions of micropores in active carbons using the Dubinin-Radushkevich equation, *Carbon* 25 (1987) 49.
- [54] G. Skodras, Ir. Diamantopoulou, G.P. Sakellariopoulos, Role of activated carbon structural properties and surface chemistry in mercury adsorption, *Desalination* 210 (2007) 281-286.
- [55] K. Foster, The role of micropore size and chemical nature of the pore structure on the adsorption properties of activated carbon fibers, thesis, University of Illinois, 1993.
- [56] C.T. Ho, D.D.L. Chung, Bromination of graphitic pitch-based carbon fibers, *Carbon* 28 (1990) 831-837.
- [57] C.T. Ho, D.D.L. Chung, Carbon fibers brominated by electrochemical intercalation, *Carbon* 28 (1990) 521-528.
- [58] B.R. Puri, Chemistry and Physics of Carbon, Marcel Dekker, New York, 1970.
- [59] Z. Yue, J. Economy, G. Bordson, Preparation and characterization of NaOH-activated carbons from phenolic resin. *J. Mater. Chem.* 16 (2006) 1456-1461.
- [60] J. Wu, J. Chen, S. Zhang, P. He, J. Fang, Y. Wu, Removal of gas-phase elemental mercury by bromine-impregnated activated carbon. *Adv. Mater. Res.* 356-360 (2012) 1660-1663.
- [61] Z. Tan, L. Sun, J. Xiang, H. Zeng, Z. Liu, S. Hu, J. Qiu, Gas phase elemental mercury removal by novel carbon-based sorbents, *Carbon* 50 (2012) 362-371.
- [62] J. Economy, C. Mangun, Z. Yue, Activated organic coatings on a fiber substrate, US Patent 6517906, 2003
- [63] Z. Yue, C.L. Mangun, J. Economy, Preparation of fibrous porous materials by chemical activation 1. ZnCl<sub>2</sub> activation of polymer-coated fibers, *Carbon* 40 (2002) 1181-1191.
- [64] Z. Yue, C.L. Mangun, J. Economy, Preparation of fibrous porous materials by chemical activation 2. H<sub>3</sub>PO<sub>4</sub> activation of polymer coated fibers, *Carbon* 41 (2003) 1809-1817.

[65] Y.H. Li, C.W. Lee, B.K. Gullett, Importance of activated carbon's oxygen surface functional groups on elemental mercury adsorption, *Fuel* 82 (2003) 451-457.

## CHAPTER 3

### DESIGN OF ADVANCED NANOFILTRATION MEMBRANES FOR WATER PURIFICATION AND DESALINATION

#### 3.1 Background

##### 3.1.1 Water crisis

Although water is the commonest substance on earth, only 2.53 percent is freshwater. Among this relatively low percentage of freshwater, two thirds of this freshwater is locked up in glaciers and permanent snow cover. The accessible freshwater in lakes, rivers, aquifers, rainfall run-off and man-made reservoirs, is now increasingly coming under pressure. Besides population growth, pressures also come from climate change and pollution [1]. Every day about 2 million tons of wastes are dumped into receiving waters, including industrial wastes and chemicals, human waste and agricultural wastes (fertilizers, pesticides and pesticide residues). Therefore, safe drinking water with good microbiologic and chemical quality is critically needed in many regions of the world.

##### 3.1.2 History of membrane development

Systematic studies of membranes were carried out as early as the eighteenth century. In 1748, Abb éNolet used a diaphragm for water permeation. However, due to its unreliability, low flux, low selectivity and high cost, this kind of membranes had no widespread industrial applications. The membrane processes was not commercialized until 1960s, when Loeb and Sourirajan developed a method to prepare defect-free, high-flux, anisotropic membranes [2]. Based on Loeb-Sourirajan technique, industrial applications involving membrane processes and their alternatives such as distillation, evaporation and extraction started to emerge. By 1980, microfiltration (MF),

ultrafiltration (UF), reverse osmosis and electro dialysis were all well-established processes. In the 1980s, gas separation and pervaporation membranes were introduced and commercialized.

The driving forces for membrane separation can be pressure, chemical potential or electric potential. For pressure-driven processes, the driving force is the pressure difference across membranes. As illustrated in Figure 3.1, this kind of process includes microfiltration (MF), ultrafiltration (UF), nanofiltration (NF) and reverse osmosis (RO). The separation mechanism for MF is molecular sieving through fine pores. MF is primarily used to separate particles and bacteria ranging from 0.1 to 10  $\mu\text{m}$  in diameter under an operating pressures below 2 bar. UF has the same separation mechanism as MF. UF can be used to filter dissolved macromolecules, e.g. proteins, from solution and operating pressures are between 1 and 10 bar. NF is between pure RO and pure UF. Sometimes NF is called loose RO or low-pressure RO. NF is usually operated at pressures of 4-14 bar and is used to separate sugars, other organic molecules or multivalent salts from monovalent salts and water. RO membranes are not considered to have pores or very small pores (0.3 to 0.5 nm), which is in the range of thermal motion of the polymer chains. Transport of the solvent is accomplished through the free volume between the segments of the polymer. Separation occurs due to the difference in solubility and mobility of different solutes in the membrane. This mechanism is called the solution-diffusion model. The operating pressures in RO are generally between 10 and 100 bar.

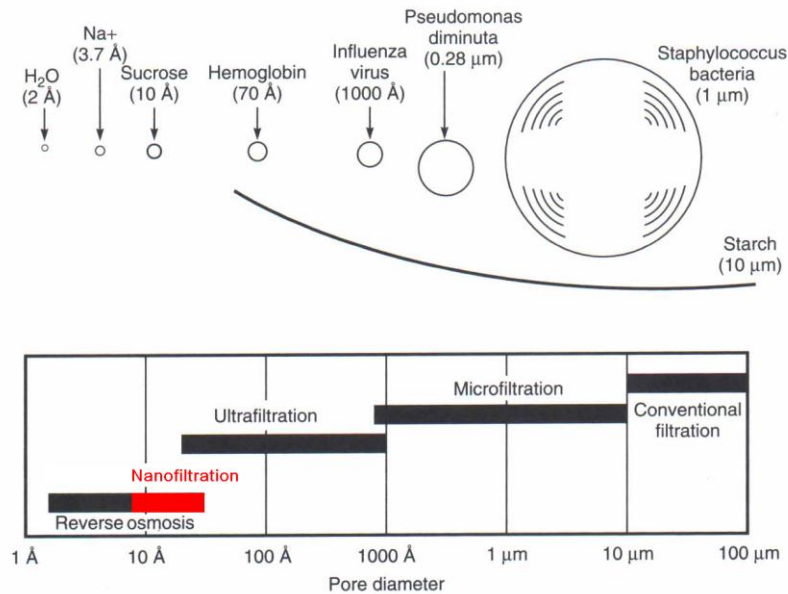


**Figure 3.1 Nominal pore diameter of different membranes [3]**

### 3.1.3 Nanofiltration membranes

Nanofiltration (NF), sometimes is defined “as a process between Ultrafiltration (UF) and Reverse Osmosis (RO). Typically, NF membranes have sodium chloride rejections between 20 and 80% and molecular weight cutoffs for dissolved organic solutes of 200-1000 Dalton.

NF membranes have found many applications in a variety of industries including food [4], textile [5], pulp and paper [6], chemical [7] and water [8]. Almost all of the applications fall into three areas: 1) removal of monovalent ions from solution; 2) separation between ions with different valences; and 3) separation of low- and high-molecular weight components. NF membrane principal application is to remove low levels of contaminants from already relatively clean water.

The desalination performance of a NF membrane depends largely on the membrane material and the membrane structure [9]. An industrially useful NF membrane must exhibit several characteristics such as high water flux, high salt rejection, mechanical

stability, tolerance to temperature variation, resistance to fouling, and low cost. So far, a number of polymer materials such as cellulose acetates [2], polyamides [10, 11, 12], crosslinked poly (furfuryl alcohol) [13] and sulfonated polyethersulfone [14] have been used to make NF and RO membranes.

The mechanisms for NF separation mostly involve both size and Donnan exclusion effects. In NF, the separation of a non-charged solute is determined by a steric exclusion mechanism. A separation between solutes will only be achieved when the solutes have a difference in size. For charged solutes two additional mechanisms are considered:

1) Donnan exclusion [15]. Because the membrane is charged, solutes with an opposite charge (counter-ions) are attracted, while solutes with a similar charge (co-ions) are repelled. At the membrane surface a distribution of co- and counter-ions will occur and result in an additional separation.

2) Dielectric exclusion [16]. Water molecules will show a polarization in the pore of the charged membrane, which causes a decrease of the dielectric constant inside the pore. This will limit the entry of a charged solute. On the other hand, when ions moved from the bulk into the pore, a change in electrostatic free energy of the ions would also results in exclusion [17].

Although the role of these two mechanisms is under debate, Donnan exclusion is commonly considered as the separation mechanism in most literatures.

### **3.1.4 Membrane formation**

So far, there are two main techniques for membrane formation, namely 1) the phase inversion method for asymmetric membranes; and 2) the interfacial polymerization technique for composite membranes [3].

Phase inversion is a process in which a polymer in solution is converted to a solid in a controlled manner. The change in phase can be initiated in a number of ways, such as solvent evaporation, thermal precipitation, immersion precipitation and vapor precipitation [18]. In this study, immersion precipitation has been used for membrane preparation and will be discussed here briefly.

In general, a polymer solution is cast as a film on a support (glass plate or non-woven fabric) with a casting knife. Then this film is immersed into a coagulation bath containing a non-solvent. Rapid exchange of solvent and non-solvent occurs with a consequently rapid phase separation and solidification at the interface. Once the skin forms, counter-diffusion of the solvent and non-solvent decreases and a highly porous, open substructure is developed.

The membrane morphology and performance are strongly influenced by the characteristics of the casting solution, such as the polymer concentration, the intrinsic viscosity and the composition. The introduction of a third component as an additive into the casting solution has been an effective way to improve the membrane performance. This additive may have several effects on the membrane formation process. For example, the viscosity of the polymer solution will be changed. Smid et al. [19] found that the minimal skin thickness of the membrane is reduced when a higher intrinsic viscosity of the polymer is used, leading to a decrease in membrane resistance and an increase in water flux through the membrane. Also, specific interactions between polymer and additive, solvent and additive, coagulant and additive, can be induced. The diffusion rate of solvent and non-solvent may be altered as well. Thus, the membrane development is mostly an empirical process and the membrane performance is usually optimized based

on trial-and-error procedures.

Interfacial polymerization has been employed to prepare a thin layer of cross-linked polyamide depositing on a substrate ultrafiltration membrane. The performance of the membrane is mainly determined by the monomers used in the interfacial polymerization. Even small changes in the monomers structure can strongly influence the membrane properties. So far, best results were obtained using trimesoyl chloride and *m*-phenylenediamine as monomers [3]. The membrane performance and morphology will be dependent on several synthesis conditions, such as concentration of reactants, reaction time and post treatments of the resulting films [20]. Moreover, the surface roughness and pore dimension of the substrate membrane also have significant effects on the formation of the interfacial film. Generally, a smooth surface may favor the formation of a thick defect-free active layer. The resultant composite membranes will give high salt rejection and low flux. On the other hand, a rough surface may result in a thin active layer with some defects. So the composite membrane may have higher flux with a little sacrifice of salt rejection [21, 22, 23].

### **3.1.5 Surface modifications of membranes**

Surface modifications have commonly been used to further improve membrane performance of the prepared membranes. By physical and/or chemical modification, membrane chemistry, morphology and pore structure may be altered resulting in improved selectivity and permeability. Many techniques such as surface functionalization, coating, crosslinking and grafting can be used for this purpose. In this study, crosslinking and coating will be discussed briefly.



1) Cross-linking. Membranes are often prepared from soluble polymers by phase inversion method. Their solvent resistance is usually low and can be improved by cross-linking. Several strategies have been reported in the literature including reaction with di- or tri-functional molecules, hydrolysis by base treatment and UV or ion-beam irradiations. For example, polyimide membranes were modified by immersing the films in the diamine/methanol solution for a stipulated period of time [24]. A series of linear aliphatic cross-linking diamines reagents (ethylenediamine, propane-1,3-diamine, and butane-1,4-diamine) were used. Membrane surfaces can also be modified both chemically and physically when they are exposed to high energy particles. UV/ozone irradiation can break most C-C bonds and also can induce chain scission and cross-linking on polymer surface [25]. After photo-irradiation, the polyimide membranes exhibited higher permeation rates while still being able to effectively separate several combinations of gases [26].

2) Coating. A thin film can be coated on top of the membrane surface via hydrophobic interactions, hydrogen bonding, van der Waals attractions, and electrostatic interactions [27]. In recent years, polyelectrolytes have been used as coating materials to modify membrane charge and hydrophilicity [28]. Such coatings can be multilayer [29] or monolayer [30] which shows high resistance to common organic foulants like proteins and humic substances. If the fouling can still exist, membrane cleaning can be easily applied to regenerate the membranes [28, 30].

### **3.1.6 State of the art**

Among the various materials and methods for membranes, the most successful two kinds of membranes are summarized below.

Cellulose acetate (CA) membranes were the first high-performance RO membrane material discovered. A typical CA membrane exhibits a flux of  $0.9 \text{ m}^3\text{m}^{-2}\text{day}^{-1}$  at 425 psi and an average NaCl rejection of 97.5% from a 2000 mg/L NaCl feed solution. The main advantage of CA is its low price and hydrophilic nature which makes it less prone to fouling. CA also has a good chlorine resistance up to 5 ppm. Thus, today, CA membranes still maintain a small fraction of the market. However, an inherent weakness of CA is that it can be eaten by microorganisms. It also slowly hydrolyzes over time and generally should not be used above  $35^\circ\text{C}$  [3].

A more successful, commercially available RO membrane for desalination is the thin film composite (TFC) aromatic polyamide membrane. A typical membrane exhibits a NaCl rejection of 99.5 % and a flux of  $1.2 \text{ m}^3/\text{m}^2\cdot\text{day}$  for a feed solution of 35,000 mg/L NaCl at 800 psi. Figure 3.2 shows a typical structure of the composite membrane [31]. It mainly consists of a porous substrate (usually polysulfone) and an ultrathin layer of a crosslinked aromatic polyamide. The porous support provides mechanical strength, whereas the separation is performed by the thin polyamide top-layer. Although the TFC membranes exhibit both high flux and very high salt rejection, it still has several disadvantages such as low resistance to fouling, limited oxidant tolerance [32] and low resistance to organic solvents [33, 34].

Therefore, the development of advanced membranes with solvent resistant properties and anti-fouling properties is critically required for water purification.

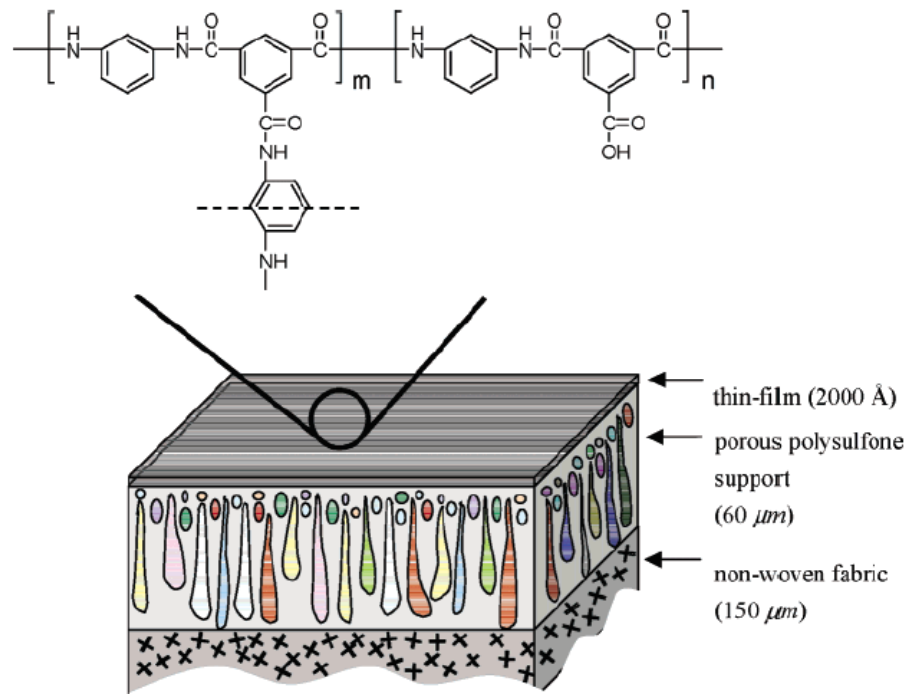


**Figure 3.2 Schematic of thin-film-composite (TFC) RO membrane and the chemical structure of the aromatic polyamide thin-film layer [31].**

### 3.1.7 Objectives of our work

The goals of our projects mainly focus on developing novel RO and nanofiltration (NF) membranes for specific properties such as solvent resistance and fouling resistance.

In Section 3.2, we prepared positively charged NF membranes by chemical modification of the P84 copolyimide asymmetric membranes using branched polyethylenimine (PEI). Different reaction temperatures were studied. The optimized membranes were prepared at 70°C, with a molecular weight cut off (MWCO) of 226 Da. The rejection sequence of  $\text{CaCl}_2 > \text{NaCl} > \text{Na}_2\text{SO}_4$  indicated a positively charged membrane surface. The rejection of selected dyes including Methyl Orange, Disperse Red and Safranin O ranged from 92% to 98%. Additionally, the resultant membranes were very stable in dimethyl formamide (DMF), a harsh aprotic solvent. Even after soaking in DMF for 1 month, there were no significant changes in membrane

performance or membrane structure. Thus, our membranes render possibilities to be used for further applications in harsh solvent environments.

In Section 3.3, we developed polyelectrolyte multilayers membranes (PEMs) involving the use of pressure during deposition process. The PEMs were prepared by alternating layer-by-layer deposition of sulfonated poly (ether ether ketone) (sPEEK) and branched polyethyleneimine (PEI). During this electrostatic self-assembly deposition, it was demonstrated that the use of pressure could increase the salt rejection of the PEMs by one to two times. The effect of polymer charge density on membrane performance, e.g. sulfonation degree of sPEEK, was also studied. By depositing the sPEEK dissolved in methanol and branched PEI dissolved in water, the rejection of the PEMs could be further increased. The rejection is about 89% and very close to that of current commercially successful polyamide membranes, which is about 96%. The antifouling property of the PEMs has also been studied. Our membranes have a better antifouling property in comparison with commercial membranes, NTR 7450.

## **3.2 Design of polyethylenimine crosslinked P84 membranes for solvent resistance**

### **3.2.1 Overview**

Solvent resistant nanofiltration (SRNF) is a relatively young technology that broke through around the beginning of the 21<sup>st</sup> century. By applying a pressure, SRNF can separate organic mixtures down to a molecular level [35]. Although SRNF is not considered as a proven technology, it holds enormous potential in applications like food applications, petrochemical applications and pharmaceutical areas [36].

In SRNF, membranes need to have chemical, mechanical and thermal stabilities as well as excellent and reproducible performance. There are two main kinds of SRNF membranes reported [37]; either a composite membrane consisting of a polydimethylsiloxane (PDMS) separation layer and a polyacrylonitrile (PAN) support layer, or an asymmetric polyimide (PI) membrane. For PDMS/PAN composite membranes, although PAN is stable in many solvents, the swelling of PDMS limits its use in many solvents [38,39]. On the other hand, PI is well known for its oxidative, mechanical and thermal stabilities [40]. However, PI membranes are not stable in aprotic solvents and chlorinated solvents. This problem can be solved by crosslinking the polymer chains using thermal treatment, UV irradiation [41] or chemical reactions [24,40].

Among the PI membranes, P84, a co-polyimide of 3,3',4,4'-benzophenone tetracarboxylic dianhydride with 80% toluenediisocyanate and 20% ethylphenylene-diisocyanate (BTDA-TDI/MDI), has been widely studied in particular due to its good resistance to a variety of solvents as well as to a broad range of pH conditions. See Toh et al. [42] and Vanherck et al. [43] have studied P84 copolyimide membranes crosslinked using different small molecular weight diamines; the resultant membranes were stable in a variety of organic solvents including methanol, toluene, methylene chloride, tetrahydrofuran (THF) and dimethyl formamide (DMF). See Toh et al. [42] also studied the molecular weight cut off (MWCO) of the crosslinked membranes. MWCO is an important parameter for membrane selections in the membrane industry, which is determined by plotting rejection of solutes against solute molecular weight and interpolating this data to find the molecular weight corresponding to the 90% rejection.

The MWCO of the membranes prepared by See Toh et al. was between 250 and 400 g mol<sup>-1</sup>.

Previously in Economy's group, Ba et al. [30] successfully prepared positively charged membranes by chemical modification of P84 asymmetric membranes using branched polyethyleneimine (PEI). The prepared membranes showed no significant changes in membrane performance after immersion in a variety of organic solvents including methanol, acetone, THF, DMF, etc. Thus, this type of membrane shows promise for use in SRNF. In this Section, using the same process as described in Ba's paper, the effect of reaction temperature on membrane performance including surface charge, MWCO, gel content will be investigated, and the solvent resistant properties against DMF will also be studied.

### **3.2.2 Experimental**

#### *3.2.2.1 Materials*

P84 powder was obtained from HP Polymer Inc. and used as received. PEI (Mw: 25000, Mn: 10000) was purchased from Sigma Aldrich. All the salts including NaCl, CaCl<sub>2</sub>, Na<sub>2</sub>SO<sub>4</sub> were obtained from Fisher Scientific and used as received. For the selected dyes, methyl orange and safranin O were obtained from Alfa Aesar while disperse red was from MP Biomedicals, LLC. A series of alkanes including C<sub>10</sub>H<sub>22</sub>, C<sub>14</sub>H<sub>30</sub>, C<sub>18</sub>H<sub>38</sub> and C<sub>22</sub>H<sub>46</sub> were all from Sigma Aldrich. All the solvents were used as received from Sigma Aldrich unless specially indicated.

#### *3.2.2.2 Preparation of the crosslinked membranes*

Asymmetric porous P84 membranes were prepared by the phase inversion technique [36]. 23% P84 in DMF solution was cast onto a polyester non-woven fabric support followed by immediate immersion into a room temperature tap water bath without evaporation of solvents in the air. After precipitation, the membranes were kept in the water bath overnight in order to exchange DMF out from the nascent membrane and then rinsed with deionized (DI) water for further modifications.

The crosslinked membranes were prepared using a modified procedure as described previously [30]. P84 membranes were immersed in a 1% PEI solution (wt/vol) in a mixture of isopropanol and water (1:1 in volume) at varied temperatures including room temperature, 50°C, 70°C and 90°C for 60 mins. After that, the resultant membranes were rinsed with and stored in DI water before carrying out further treatments.

### *3.2.2.3 Nanofiltration tests*

The desalination performance of the membranes was carried out using a dead-end filtration cell (Sterlitech™ HP4750) under a pressure of 13.79 bar at room temperature. A standard magnetic stirrer (Corning Stirrer/Hot Plate, Model PC-420) was used to minimize the influence of concentration polarization. Typically, 300 ml of feed solution was needed and the concentration of the solution was 2 g/L NaCl in DI water. The permeated samples were collected until a stable permeation flux was achieved and the concentration of the permeation solution was determined using a Corning pH/ion analyzer 455. The salt rejection  $R$  of the membranes was determined by comparing the permeation concentration and feed concentration using

$$R = (1 - C_p/C_f) \times 100\%$$

where  $C_p$  and  $C_f$  represent the permeation concentration and feed concentration respectively.

Besides NaCl solution, the same experiments were done using 2 g/L  $\text{CaCl}_2$  and  $\text{Na}_2\text{SO}_4$  aqueous solutions. By comparing the rejections of these three solutions, the surface charge of the membranes can be determined qualitatively.

#### *3.2.2.4 MWCO (Molecular weight cut off) measurement*

The procedures used for MWCO determination were based on the method described by See Toh et al [44]. A series of *n*-alkane test solutions including decane, tetradecane, octadecane and docosane were prepared by dissolving these solutes in methanol solution at low concentrations (100 mg/L). After the feed solution passed through the dead-end filtration cell, the concentrations of permeation solutions were determined using an Agilent 7890A Gas Chromatograph (GC) equipped with a standard 5975C mass selective detector and a commercial Wiley and NIST libraries (2008 edition) for mass spectra interpretation. By plotting a graph of rejection of solutes against solute molecular weight, MWCO can be determined by finding the molecular weight corresponding to the 90% rejection.

#### *3.2.2.5 Gel content measurement*

The gel content of the membranes was determined by the weight change after immersing the membranes in DMF after two weeks [43].



$$\text{Gel content} = W_a / W_b \times 100\%$$

where  $W_a$  and  $W_b$  are the dry weight of the membranes after and before soaking in DMF, respectively. Since untreated P84 is soluble in DMF while the crosslinked part after chemical modification is not, the retained weight of the membranes can be used to characterize the stability of the crosslinked membranes.

### 3.2.2.6 Separation of selected dyes in methanol solution

Separation of organic dyes in methanol solution has long been used to characterize the solvent resistant properties of membranes [39,45]. Three dyes including disperse red, methyl orange and safranin O were selected in this paper to characterize the membrane performance in methanol solution since they have similar molecular weight (MW) but different charges. The concentrations of feed solutions were 100 mg/L, while the concentrations of the permeation solution were determined using a Varian Cary 5G Ultraviolet (UV) spectrophotometer. The molecular weight, charge and detection UV wavelength of these dyes were listed in Table 3.1.

**Table 3.1 Principle characteristic of the selected dyes**

Dyes	Methyl Orange	Disperse Red	Safranin O
MW (g/mol)	327.3	314	350.85
Charge	Negative	Neutral	Positive
Max. Wavelength (nm)	422	570	528

### 3.2.2.7 Physical characterization methods

All the membranes were dried using solvent exchange method to prevent the collapse of the porous structures. The samples were immersed in isopropanol overnight to

displace the water contained in the membranes followed by the same procedures using hexane and then dried in vacuum to remove the residual solvents from the membranes for further characterizations.

Thermogravimetric analyzer (TGA) was performed using a Hi-Res 2950 TA instrument. The samples (10-20 mg) were heated at 10°C/min to 700°C, and then held at that temperature for 30 min in nitrogen.

A commercial Hitachi S-4800 scanning electron microscope (SEM) was used for high resolution examination of both the surfaces and the cross-sections of our samples. For cross-sectional observations, the membranes need to be fractured after immersion in liquid N<sub>2</sub> to retain the porous structure. Then the samples were peeled off from the polyester support and coated with gold and palladium by sputtering for conductivity improvement before SEM testing. The accelerating voltage used for all runs was 10.0 kV.

### **3.2.3 Results and discussion**

#### *3.2.3.1 Effect of reaction temperature on surface charge*

Figure 3.3 shows the effect of reaction temperatures on the rejections of three salts including Na<sub>2</sub>SO<sub>4</sub>, NaCl and CaCl<sub>2</sub>. With increasing reaction temperature, the rejections for these three salts increase gradually until they reach a stable value while the permeation fluxes decrease during the range. This phenomenon is reasonable since more PEI will diffuse into and react with the P84 substrate as reaction temperature increases, thus a denser and more crosslinked barrier layer will be formed, resulting in higher rejections and lower permeation fluxes for these salts. When the reaction is completed (i.e. 70°C in this case), a stable value for salt rejections will be achieved. On the other

hand, a further temperature increase probably brings about the shrinkage of the pore structure of the P84 support, which may lead to a further decrease in permeation flux [46]. Comparing the membrane performance of the samples prepared at different temperatures, reaction temperature of 70°C seems to be the optimized value for our experiment since membranes prepared at this temperature have the highest salt rejections while still retaining reasonable fluxes.

Besides, the rejection sequence of  $\text{CaCl}_2 > \text{NaCl} > \text{Na}_2\text{SO}_4$  indicates that the membranes have a positively charged surface [47]. The positive charge is attributed to the amine groups remaining after the interaction between PEI and P84 copolyimide [30]. As shown in Figure 3.3, the membranes get more and more positively charged with the increase of reaction temperature. This trend is consistent with the process of reaction since more PEI is introduced into the membranes as temperature increases, which brings in more amine groups resulting in more charge.

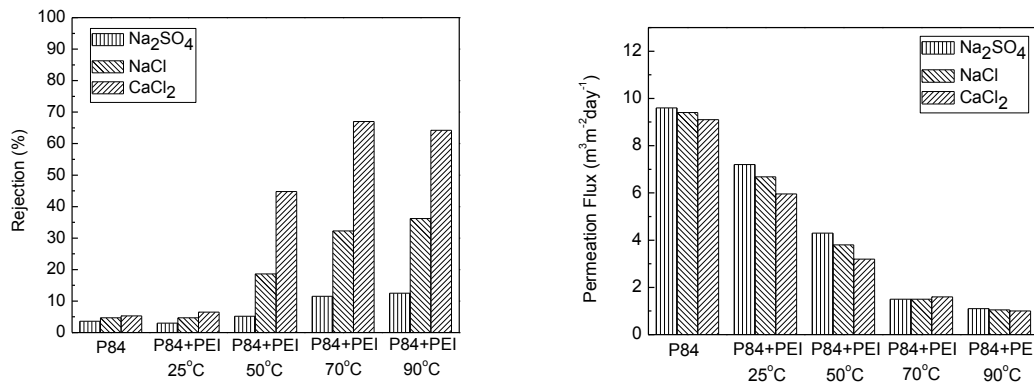


**Figure 3.3 salt rejections and permeation flux of the membranes prepared at different temperatures**

### 3.2.3.2 Effect of reaction temperature on MWCO

Figure 3.4 shows the MWCO of the membranes prepared at different reaction temperature. A series of *n*-alkanes including C<sub>10</sub>H<sub>22</sub>, C<sub>14</sub>H<sub>30</sub>, C<sub>18</sub>H<sub>38</sub> and C<sub>22</sub>H<sub>46</sub> in methanol solution was selected to determine the MWCO of the membranes due to the low cost, no charge and ease of access for *n*-alkanes while methanol was used as solvent since the membranes would be applied in solvent resistant areas. For each membrane, rejection increases with increasing molecular weight. Additionally, the rejections for these four solutes increase as reaction temperature increases until the lowest MWCO of 228 g/mol for membranes prepared at 70°C. This trend is consistent with our previous study for the surface charge; a more crosslinked structure will be formed as reaction temperature increases and modification progresses, resulting in higher rejections and lower MWCO. On the contrary, the membranes prepared at 90°C has a larger MWCO (around 280 g/mol) compared with those prepared at 70°C. This is probably because the membrane goes through a re-imidization process causing a loss in membrane performance [30]. The MWCO values also confirmed that the membranes prepared at 70°C and 90°C fell into the nanofiltration range, which normally spans from 200-1000 g/mol. Additionally, our results are comparable with the values (250-400 g/mol) reported by See Toh et al [42], who crosslinked P84 substrate using small molecular weight diamines. Although the membranes prepared by small molecular diamines may have a more dense structure due to their shorter chains, the branched structure of PEI and positive charge renders more interaction between the surface and the solutes. Therefore, our membranes crosslinked using PEI at 70°C and 90°C show better separation performance compared with the reported data by See Toh et al.

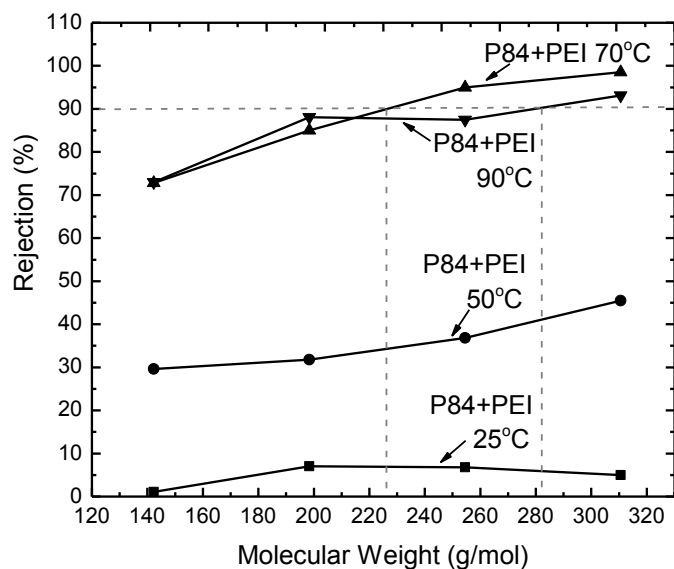


**Figure 3.4 MWCO of the membranes prepared at different reaction temperatures**

### 3.2.3.3 Characteristics of the membranes crosslinked at different reaction temperatures

Thermal properties of the membranes prepared at different temperatures are shown in Figure 3.5. For the original P84, there are mainly two peaks in the derivative weight lose curve. The first peak is a little less than 100°C, which is due to the adsorption of water [48]. The P84 is thermally stable until 305°C, where a degradation of the polymer chain happens. After modification, a new peak around 185°C appears corresponding to the contribution of PEI. At the same time, the peak intensity increases as the reaction temperature increases. This result is in good agreement with our previous study, which shows that more and more PEI will get into the membranes with an increase in reaction temperature, hence a more positively charged surface and a more crosslinked structure will be obtained.

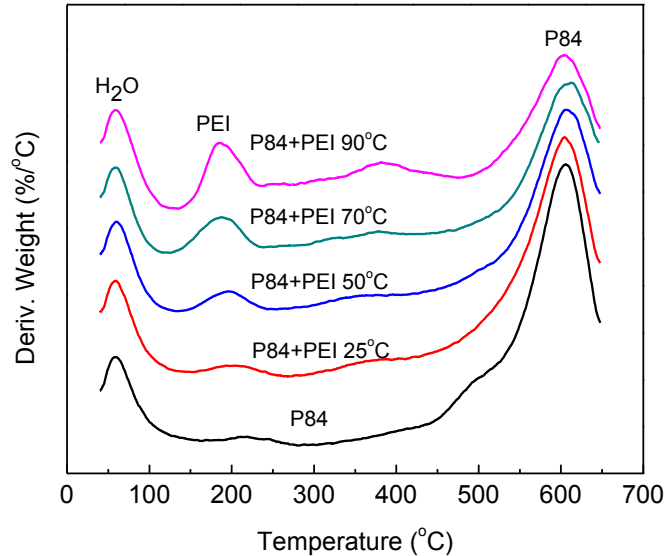


**Figure 3.5 Derivative TGA curves for the membranes prepared using PEI at various reaction temperatures**

The remained weights of the membranes after soaking in DMF for two weeks are shown in Table 3.2. DMF was selected as the test solvent because untreated P84 is soluble in DMF while the crosslinked part after chemical modification is not. Theoretically, original P84 should be completely dissolved in DMF and no weight should be left in the membranes after two weeks. The remained weight in our experiment was caused by the insoluble interpenetrated polyester when the membrane was peeled off the polyester fabric used for mechanical support. Less weight loss is observed with the increase of reaction temperature due to the formation of a more crosslinked structure as interaction between PEI and P84 proceeds. There is almost no weight change for the membranes prepared at 70°C and 90°C, indicating a highly crosslinked structure of the membranes and a significantly improved resistance against DMF.

**Table 3.2 Gel contents of the membranes prepared at various reaction temperatures**

	Gel Content
P84	25.2%
P84+PEI 25°C	66.2%
P84+PEI 50°C	84.5%
P84+PEI 70°C	96.2%
P84+PEI 90°C	96.4%

#### *3.2.3.4 Morphology study of the membranes prepared at different reaction temperatures*

The SEM analysis of the membranes prepared at different reaction temperatures is shown in Figure 3.6. With an increase in reaction temperature, the membrane pores get narrower as shown in the surface images for P84, P84+PEI 25°C and P84+PEI 50°C. This is reasonable since with an increase in temperature, more PEI molecules diffuse into the pores and anchor on the pore walls, resulting in much narrower pores. Then after a thin layer of PEI forms, a much rougher surface can be observed as shown in P84+PEI 70°C and P84+PEI 90°C. The thin layer formed by PEI is more obvious in the cross-sectional images, especially in P84+PEI 50°C and P84+PEI 70°C. These images vividly confirm our previous speculation, which is that a denser and more crosslinked barrier layer will be formed as more and more PEI will get into the membranes with the increase of reaction temperature, resulting in higher rejections and lower permeation fluxes.

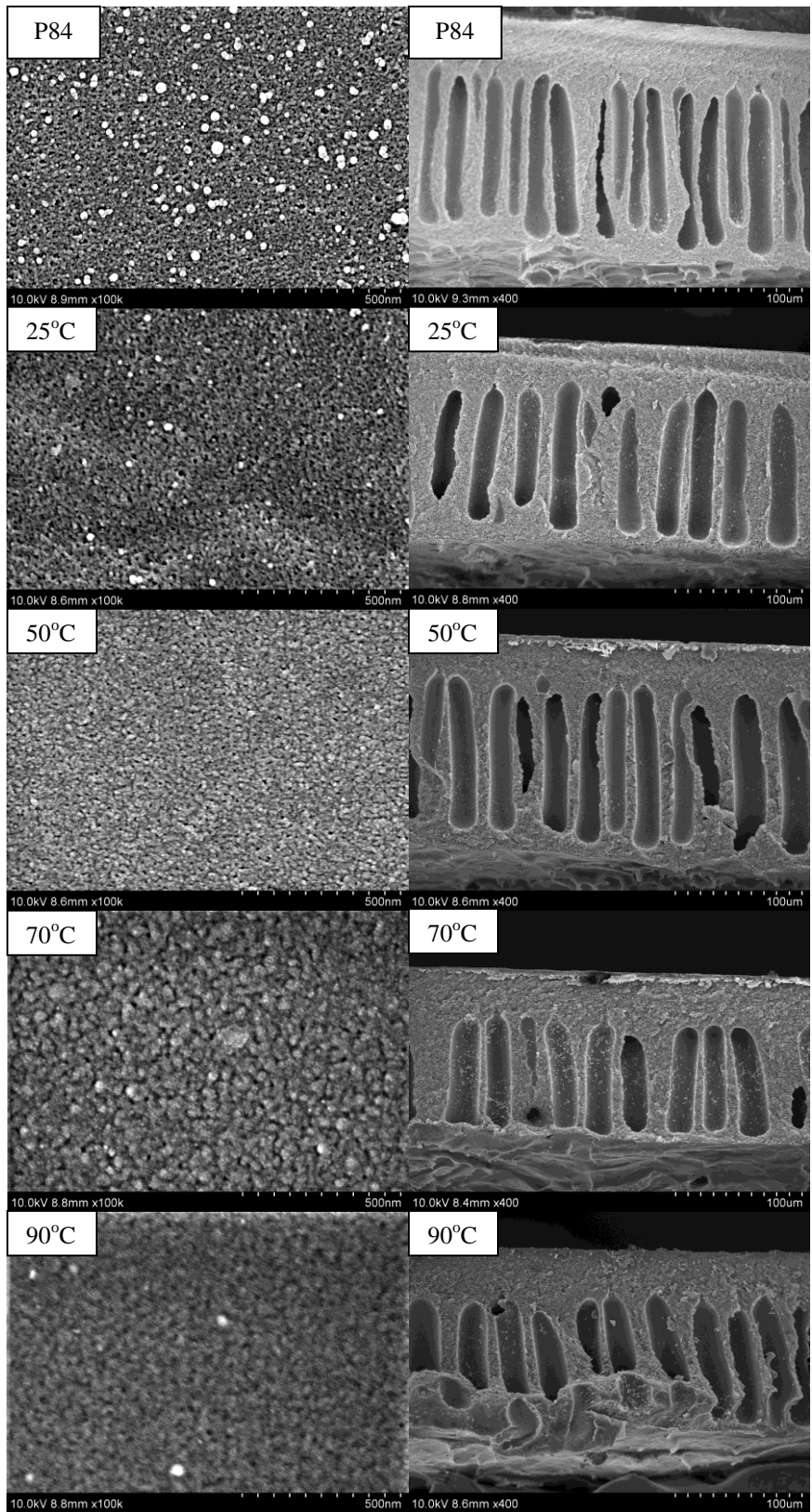


**Figure 3.6 Surface (left) and cross-sectional (right) morphologies of P84 membranes prepared at different temperatures**



### *3.2.3.5 Separation of selected dyes in methanol solution*

Three dyes including disperse red, methyl orange and safranin O were selected to characterize the membrane performance since they have similar molecular weight (MW) but different charges while methanol was used as solvent since it is a commonly used organic solvent. The membranes used here were prepared under the optimized conditions of 70°C in this case. The permeation flux and solute rejection of these dyes as a function of time were shown in Figure 3.7. Due to the positively charged surface of the membrane, the rejection for safranin O is the highest (over 98%), followed by disperse red (94%~98%) and methyl orange (90%~94%). However, the differences between the rejections of these selected dyes are not as significant as those of the selected inorganic salts. In other words, surface charge may have a less significant effect on membrane performance in methanol solution. This is probably because all selected dyes have slight larger MW (314-350 g/mol) than the MWCO (228 g/mol) of the positively charged membranes, hence these solutes will be rejected mainly by a sieve mechanism while the effect of surface charge is negligible [49]. Another possible reason is that the interaction between the solute-membrane-solvent is different for aqueous and non-aqueous systems [45]. These results indicate that our membranes have a stable performance in methanol up to 10 hours, and a very effective behavior to separate solutes higher than 314 g/mol no matter what kind of charge the solutes have.

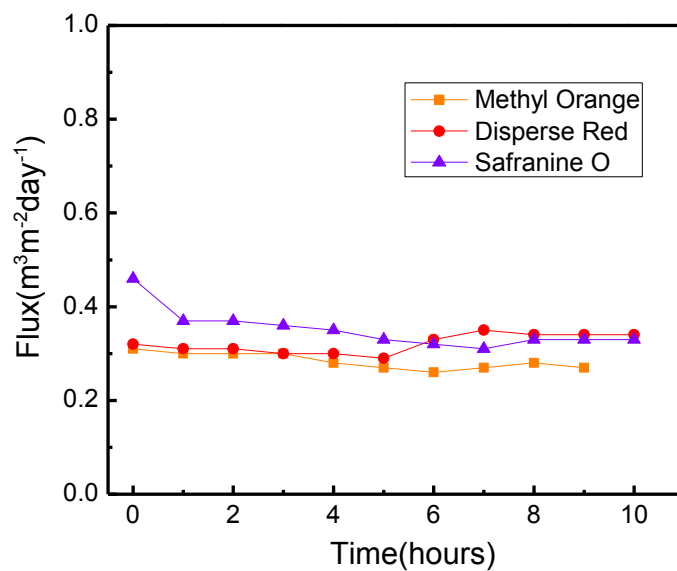
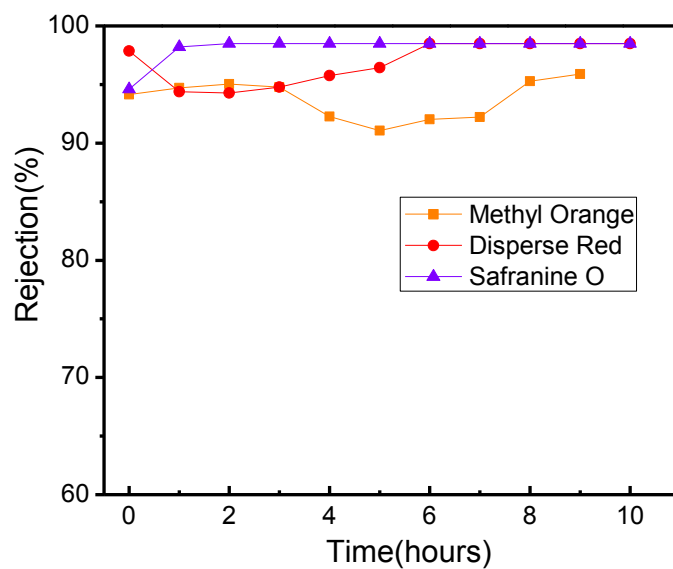


**Figure 3.7 Separation performance of selected dyes in methanol solution using the membranes prepared at 70°C**

*3.2.3.6 Membrane performance against DMF*

For the membranes prepared at 70°C, their performance before and after soaking in DMF for 30 days was also compared. DMF was selected here due to its harsh aprotic

properties. As shown in Figure 3.8, there is almost no change in either the rejection or permeation flux after the treatment of DMF. This result indicates that both chemical composition and pore structure of the membranes show excellent resistance against DMF. The improved resistance is caused by the crosslinking structure resulted from the reaction between PEI and P84 [30]. One minor thing to be noted is that the membrane after the treatment is not as positively charged as before the treatment by comparing the sequence rejections of  $\text{CaCl}_2$ ,  $\text{NaCl}$  and  $\text{Na}_2\text{SO}_4$ . A possible reason is that the membrane is slightly neutralized by the contaminants in DMF solvent during the period when the membrane is soaking in DMF for 1 month.

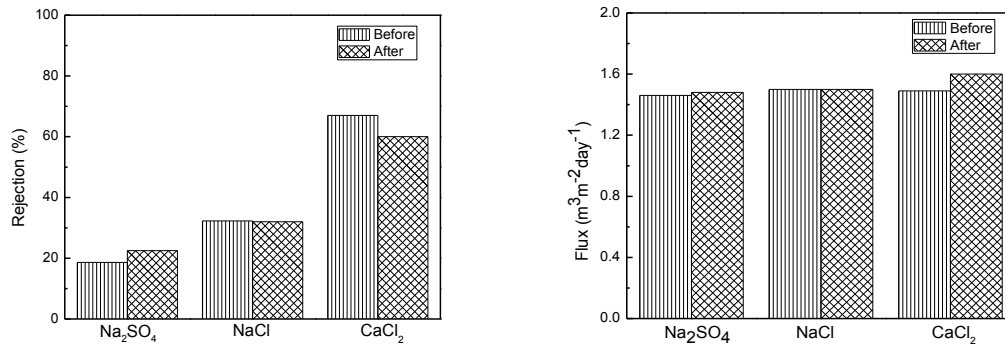


**Figure 3.8 Effect of DMF treatment on membrane performance**

The morphologies of the crosslinking membranes prepared at  $70^\circ\text{C}$  before and after soaking in DMF are shown in Figure 3.9. There is no visible difference for both surface and cross-sectional images before and after DMF treatment. Both the thickness of the dense layer and the pore size of the membrane surface can contribute to the permeation flux [50], hence the permeation fluxes remain unchanged even after soaking in DMF for 1 month. These images vividly confirm our previous study that the pore structure of the membranes shows excellent resistance against DMF.

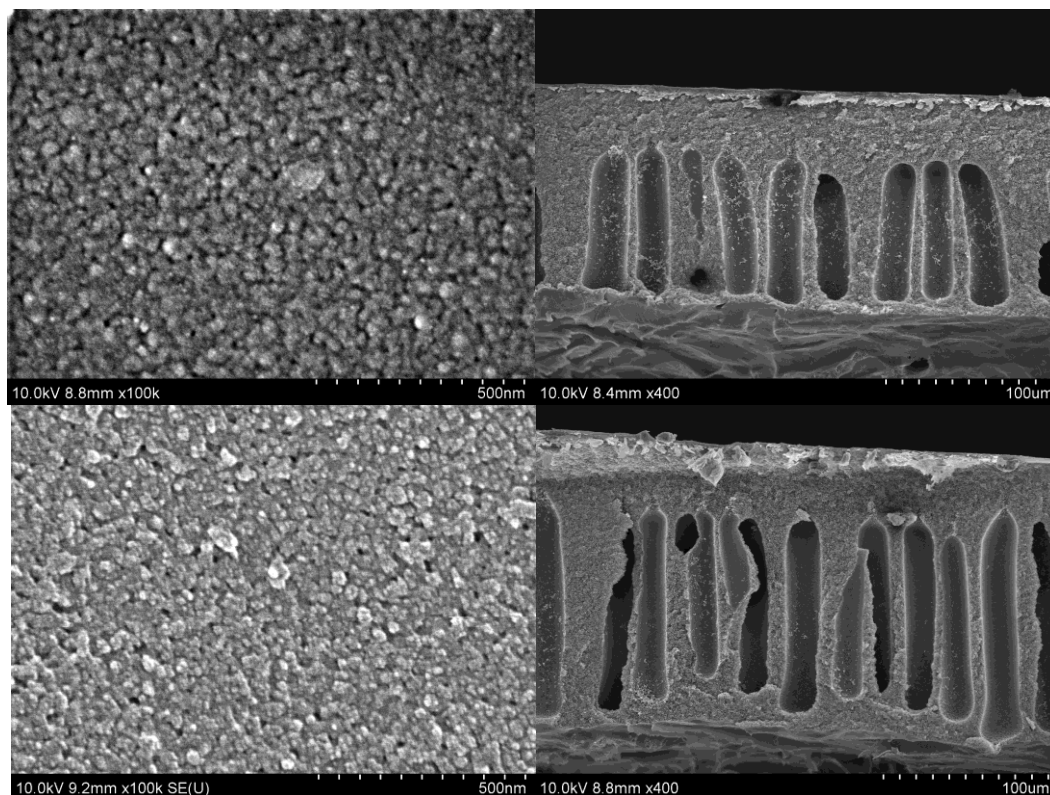


**Figure 3.9 Surface (left) and cross-sectional (right) morphologies of PEI modified P84 membranes prepared at 70°C before and after soaking in DMF for 1 month**

### 3.2.4 Conclusions

In this Section, the solvent resistant nanofiltration membranes were prepared by chemical reaction between PEI and P84 asymmetric membranes. The resultant membranes have a positively charged surface and a highly crosslinked structure. The rejections increase as the reaction temperature increases until the reaction temperature reaches 70°C. Above that temperature, a loss of membrane performance was observed which is probably caused by polymer re-imidization.

The membranes prepared at 70°C under the optimized condition, have a MWCO of 228 g/mol. These membranes can successfully filter 92% to 98% of the selected dyes including methyl orange, disperse red and safranin O from methanol solution no matter

what kind of charge these solutes carry. The crosslinking structures also show an improved stability in DMF, a harsh aprotic solvent. There is almost no weight change after immersing in DMF for 2 weeks. Even after soaking in DMF for 1 month, there are still no significant changes in both permeation flux and rejections for  $\text{CaCl}_2$ ,  $\text{NaCl}$  and  $\text{Na}_2\text{SO}_4$ . Thus, this type of membrane shows great potential for applications in solvent resistance nanofiltration areas.

### **3.3 Preparation of polyelectrolyte multilayer membranes for anti-fouling properties**

#### **3.3.1 Overview**

The alternating physisorption of oppositely charged polyelectrolytes on porous supports is a relatively new technique that provides a simple way to create ultrathin polyelectrolyte multilayers (PEMs). In the late 1960s, Iler et al. first reported the alternate self-assembly of charged colloidal particles and suggested the idea of building a multilayer structure from polycations and polyanions by electrostatic interaction [51]. In 1991, Decher et al. first deposited charged polymers alternately to form thin multilayer films by this method [52,53]. In comparison with Langmuir-Blodgett (LB) or conventional spin coating and casting techniques, the electrostatic self-assembly has several advantages: (1) the films are mechanically stable because of a strong electrostatic interaction; and (2) there are no pinholes and other defects as in LB films. In addition, this process can be carried out under ambient conditions using economically available raw materials [54].

PEMs, typically  $< 1 \mu\text{m}$  thick, are created by alternately exposing a substrate to positively- and negatively-charged polyelectrolyte with an interval process, e.g. the rinse

of water and/or drying. The amount of adsorbed polyelectrolyte and the layer structure (conformation of the attached chains) are governed by parameters such as the charge density of the polyelectrolyte, the sign and the density of the surface charge, and the ionic strength of the depositing solution [55,56,57]. As illustrated in Figure 3.10, in general, higher charge density of the polymer results in a more compacted conformation. When salts are added, the charge of the polymer will be screened to some extent. This is the same effect as the reduction of charge density of the polymer, i.e. the layer becomes thicker and more polymer segments are adsorbed.

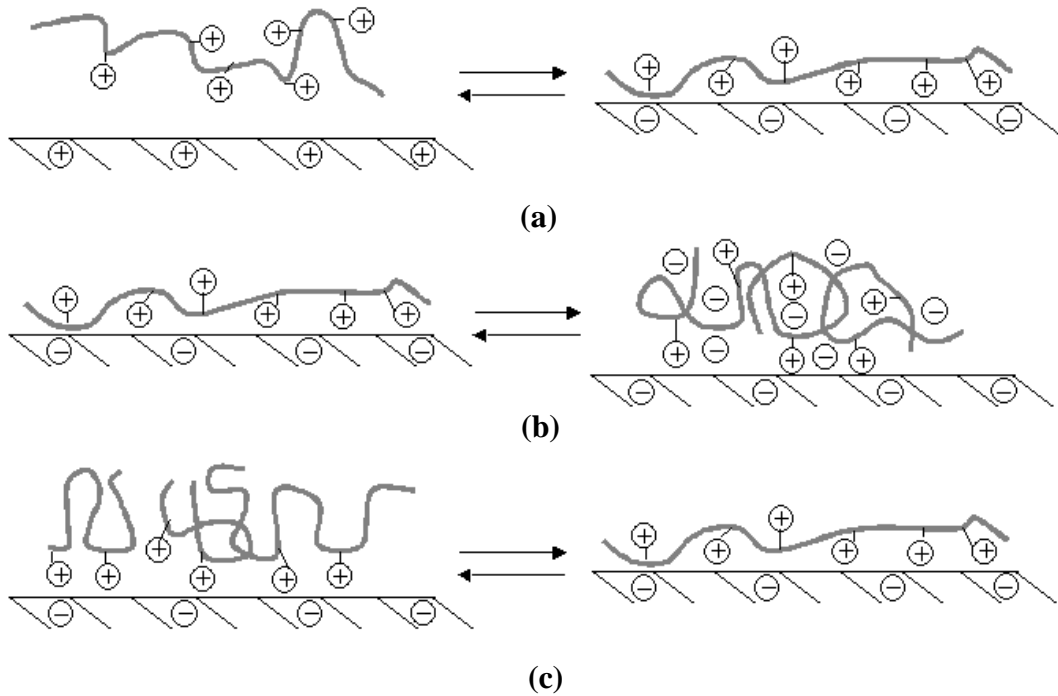


**Figure 3.10 Schematic description of the adsorption of a charged homopolymer at a solid surface. Effects of (a) surface charge, (b) electrostatic screening and (c) charge density of the polymer on the amount and the structure of the adsorbed polyelectrolyte [54]**

The method of polyelectrolyte self-assembly has now been adopted in many applications including controlled drug delivery, molecular sensors, artificial muscles, solid battery electrolytes, and separation membranes. Despite the enormous research activities in the field of polyelectrolyte multilayers, only a small number of publications has involved this simple technique for the preparation or modification of membranes, especially for NF membranes [54,58]. However, there are several advantages of PEM films for NF membranes [59]. First, PEM films have high water adsorption. It was reported that from 6 to 10 water molecules were associated with each ionic group (regardless of sign) in a neutral polyelectrolyte complex. This number corresponds to the first hydration sphere around ions. Since these water molecules can be considered as bound water instead of free water, it is possible to achieve a high selectivity in the passage of water relative to the passage of salt. Second, the proximity of ionic groups facilitates the transport of water. Finally, for non-neutral complexes, the presence of immobilized ions in NF membranes will suppress the imbibing of ions from solution due to the Donnan exclusion effects. In addition, this “layer-by-layer” or “electrostatic self-assembly” (ESA) method affords control over thickness, charge density, and composition of the selective skin layer in NF membranes. Moreover, a wide range of polyelectrolytes is available to form PEM films. Therefore, flux, selectivity and possibly fouling rates of NF membranes could be tailored by judicious selection of constituent polyelectrolytes. Despite the versatility of PEM films, studies for NF applications thus far have primarily focused on poly (styrene sulfonate)/poly (allylamine hydrochloride) (PSS/PAH) [60], PSS/Chitosan [61], PSS/poly(diallyldimethylammonium chloride) (PDADMAC) [61], hyaluronic acid (HA)/Chitosan [61], and poly (vinyl amine)/poly (vinyl sulfate) [62]. The

highest rejection among the PEM films reportedly by Bruening et al. was only around 40% for a feed concentration of 0.01 M NaCl [60,61]. Although Tieke et al. achieved 84% rejection for 0.01 M NaCl, the flux was relatively low ( $\sim 0.013 \text{ m}^3 \text{ m}^{-2} \text{ day}^{-1}$  at 5 bars). In his case he deposited 60-bilayer poly (vinyl amine)/poly (vinyl sulfate) films on PAN/PET supporting membranes [62]. In addition, all these PEM films were prepared in water. The formation of PEM films in organic solvents for NF application has received much less attention.

In this Section, we prepared PEM membranes consisting of sulfonated poly (ether ether ketone) (sPEEK) and branched polyethyleneimine (PEI). The typical structure is shown in Figure 3.11. By applying pressure during the deposition process, a relatively high salt rejection (up to 89%) can be obtained with only several bilayers (below 5 bilayers). The effect of polymer charge density on membrane performance, e.g. sulfonation degree of sPEEK, was also studied. By depositing the sPEEK dissolved in methanol and branched PEI dissolved in water, the rejection of the PEMs could be further increased. The rejection is about 89% and very close to that of current commercially successful polyamide membranes, which is about 96%. The antifouling property of the PEMs has also been studied. Our membranes have a better antifouling property in comparison with commercial membranes with sulfonated surfaces, NTR 7450.



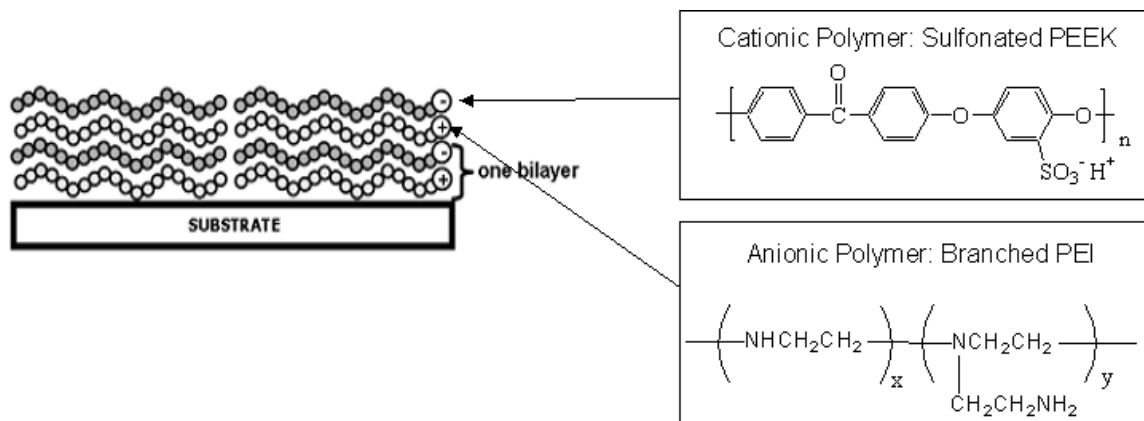


**Figure 3.11 Layer-by-Layer electrostatic assembly of sPEEK and PEI**

### 3.3.2 Experimental

#### 3.3.2.1 Materials

PAN (homopolymer,  $T_g = 85^\circ\text{C}$ , average  $M_w$  150,000), polyvinylpyrrolidone (PVP,  $M_w = 29,000$ ), branched polyethylenimine (PEI, typical  $M_n = 10,000$  (GPC), typical  $M_w = 25,000$  (LS)), low molecular weight polyethylenimine (typical  $M_n = 600$  (GPC), typical  $M_w = 800$  (LS), branched), and poly(4-vinylpyridine) (P4VP, typical  $M_w = 160,000$ ,  $T_g = 142^\circ\text{C}$  (onset, annealed)) were received from Aldrich. Poly(ether ether ketone) (PEEK) pellets was purchased from Polysciences, Inc.

#### 3.3.2.2 Preparation of asymmetric hydrolyzed PAN UF membranes for substrate membranes

The UF membranes were prepared by the phase separation technique using water as a coagulant. PAN was used as a membrane material and PVP as an additive to make the membrane more porous. PAN and PVP powder were dissolved at  $80\text{-}90^\circ\text{C}$  with stirring in DMF to form a 15:5 wt% PAN: PVP casting solution. The solution was cast onto a Hollytex® polyester non-woven fabric using a laboratory membrane-casting machine

(Separation Systems Technology, USA). The nascent membrane was immersed in a room temperature tap water coagulation bath without evaporation of solvents in the air. After precipitation, the membrane was kept in a water bath for several days and then washed with deionized water before further experiments. The substrate membrane was then obtained by hydrolysis in 1M NaOH for 24hours and soaked in 1M HCl solution overnight followed with DI water rinsing.

#### *3.3.2.3 Sulfonation of PEEK*

Victrex<sup>®</sup> PEEK was sulfonated according to the procedure described by Cui et al with a small modification to prepare sPEEK soluble in water [63]. The polymer (60 g) was dissolved in 95–97% H<sub>2</sub>SO<sub>4</sub> (330ml) at room temperature and at 70 °C for 30mins. The reaction temperature was decreased to 60 °C and the reaction mixture was stirred for an additional 8 hrs. sPEEK dissolved in methanol and NMF was prepared via the method of Bailly et al [64] by vigorously stirring PEEK in 95–97% H<sub>2</sub>SO<sub>4</sub> for 3 and 5 days, respectively. The sulfonated polymer was then precipitated in 5 L of water, filtered off and washed in DI water until a neutral pH was obtained. The polymer was finally dried to constant weight at 80 °C.

#### *3.3.2.4 Film Deposition*

The hydrolyzed PAN substrate membrane was assembled in a filtration cell (Sterlitech<sup>™</sup> HP4750 Stirred Cell) so that only the PAN side contacted the polyelectrolyte solution. 200 ml 0.1 M PEI was filled in the cell and kept for 5 mins. The membrane was rinsed with 200 ml tap water three times (about 1 minute per time). The

cell was then filled with 200 ml DI water and the water was pressed through the membrane under various pressures for 5 mins. After that, the membrane was exposed to 100 ml 0.1 M sPEEK for 5 mins, followed by another three-time rinse with tap water. The cell was again filled with 200 ml DI water and the water was pressed through the membrane under pressure for 5 mins. This process was repeated until the desired number of bilayers was produced. To make the PEMs from non-aqueous systems, the water was replaced with the corresponding organic solvents.

#### *3.3.2.5 Membrane performance measurement*

Rejection was determined using a NaCl solution. The salt solution flux and salt rejection were measured at 13.79 bars and room temperature. The feed concentration was typically 2000 mg/L in pure DI water. The permeated samples were collected for a few minutes and the concentration of permeates were determined, using a Corning pH/ion analyzer 455.

#### *3.3.2.6 Characterization of the antifouling properties*

The antifouling measurement was conducted according to the process in the reference [65] with some modifications. Membranes were assembled into a Sterlitech<sup>TM</sup> HP475 stirred dead-end cell with a cell volume of 300 ml. The experiment was carried out at a pressure of 13.79 bars. DI water was first passed through the membrane for at least 2 hours until the flux remained stable. The cell was then refilled with the model foulant solution. Three kinds of model foulants were used: 1) Protein solutions comprised 1000 mg/L BSA (bovine serum albumin) in PBS (Phosphate buffered saline with BSA,

pH=7.4, powder form from Sigma); 2) NOM (natural organic matter) fouling studies used 1000 mg/L humic acid (from Alfa Aesar) and 1mM CaCl<sub>2</sub> (Ca<sup>2+</sup> ions can enhance the fouling ability of humic acid through their complexation with the carboxyl groups of humic acid) in DI water; and 3) Polysaccharide fouling experiments were performed with 1000 mg/L sodium alginate (from Aldrich) in DI water. The volume of permeate was measured and normalized to the initial volume. When permeate exceeded about 100ml, the filtration cell was refilled with a 300ml fresh foulant solution and the experiment was resumed.

### *3.3.2.7 Scanning Electron Microscopy and Attenuated Total Reflectance Fourier Transform Infrared Spectroscopy (ATR/FTIR)*

The morphology of membranes was observed with a scanning electron microscope (Hitachi S-4700). Membranes were pretreated by the solvent-exchange method to prevent the structure from collapsing upon drying. Water in the membrane was replaced first with *iso*-propanol and then with *n*-hexane.

ATR/FTIR spectra were collected in the range 4000-600 cm<sup>-1</sup>, on a Nexus 670 FT-IR (Thermo Electron Corporation, Madison, WI) with a Golden Gate<sup>™</sup> MKII Single Reflectance ATR (Specac Inc., Woodstock, GA). The spectrometer was installed with a deuterated triglycine sulfate-potassium bromide (DTGS-KBr) detector and KBr beamsplitter. Spectra collection was performed using FT-IR software (OMNIC, Thermo Electron Corporation, Madison, WI) and analyzed using spectrum software (KnowItAll Informatics System 5.0 Academic Edition, Bio-Rad Laboratories, Inc). Spectra were recorded by positioning the samples on a cell platform operating at room temperature (64

scans, 4 cm<sup>-1</sup> resolution).

### **3.3.3 Results and discussion**

#### *3.3.3.1 Effect of pressure*

Pressure as a deposition condition was investigated. The result is shown in Figure 3.12. At first, the rejection increased while flux decreased with the increase of applied pressure during the film deposition. When the pressure was higher than 13.79 bars, the rejection and flux showed little change with the pressure. The highest rejection was observed at 13.79 bars, which was 76%. It was about 2.5 times higher than that of membranes prepared without pressure. One possible explanation of this effect might be the survival of the fittest. When the film was formed, there were some weaker regions in every single layer. These regions could not withstand the pressure applied. While in the next deposition cycle, stronger layers might form on these damaged regions. Therefore, membranes suitable for the corresponding pressure survived. The final membrane should be more compact than those prepared without pressure. When a membrane formed at a lower pressure, e.g. 13.79 bars, was used at a higher pressure, e.g. 27.58 bars, the salt rejection would decrease down to 30%. This observation confirmed the existence of some weaker regions within the PEMs. In addition, the formation of PEMs inside pores of substrate hydrolyzed PAN membranes might also play a role. The PEMs in the pores might form a special orientation with the help of the flow of solvents under pressure. It seems some polyelectrolytes first attached loosely on the surface during the contact between the substrate and the polyelectrolyte solution. Then, under pressure, they were moved along the surface towards pores in the substrate with solvents and anchored there.

These results might also suggest a way to form PEMs inside nanopores with a diameter below 50 nm. These PEMs might have distinct features in comparison with the PEMs formed by directly pressing polyelectrolyte solutions through nanopores.

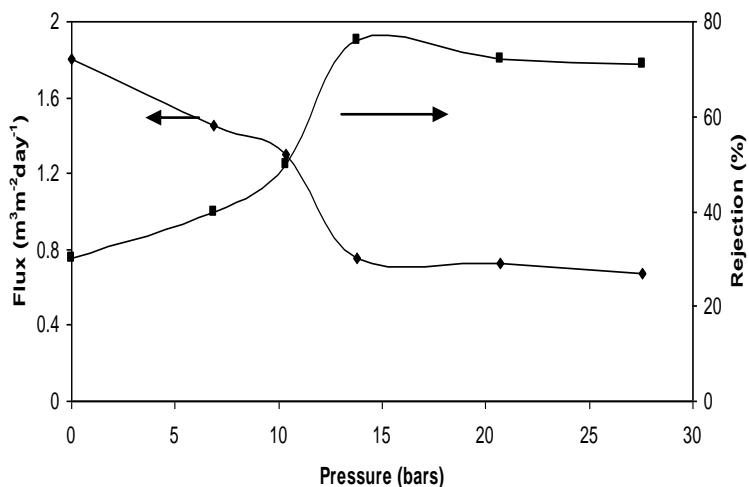


**Figure 3.12 Salt rejection (■) and flux (◆) of PEMs prepared at different pressures**

### 3.3.3.2 Effect of ionic strength

We used the depositing solutions of sPEEK and PEI containing 0, 0.1 M and 0.3 M NaCl to study the effect of ionic strength on the membrane performance. The water pressed through the membrane also contained NaCl with corresponding concentration, i.e. 0, 0.1 M and 0.3 M, respectively. The performance of final membranes consisting of 3.5 bilayers is illustrated in Figure 3.13. With the increase of ionic strength, the salt rejection decreased and the flux increased. This is expected since the salt screens the charge of polyelectrolytes, which results in the formation of looser layers with the increase of ionic strength. The results are inconsistent with previous work reported by Van de Steeg et al. [66], who also analyzed the effects of ionic strength on the adsorption of polyelectrolytes on a substrate surface. They pointed out that depending on the balance

between electrostatic and non-electrostatic attraction between polyelectrolyte segments and the substrate surface, the added salts could decrease the adsorption of polyelectrolytes. The reason is that salt screens the segment-surface attraction between polyelectrolytes and the substrate surface, which decreases the adsorption of polyelectrolytes. Hence, the ionic crosslinking density in the film would become smaller when ionic strength increased. The layers formed at a high salt concentration are thus looser than the layers formed at a low salt concentration. Therefore, with the increase of ionic strength, the salt rejection decreased and the flux increased.

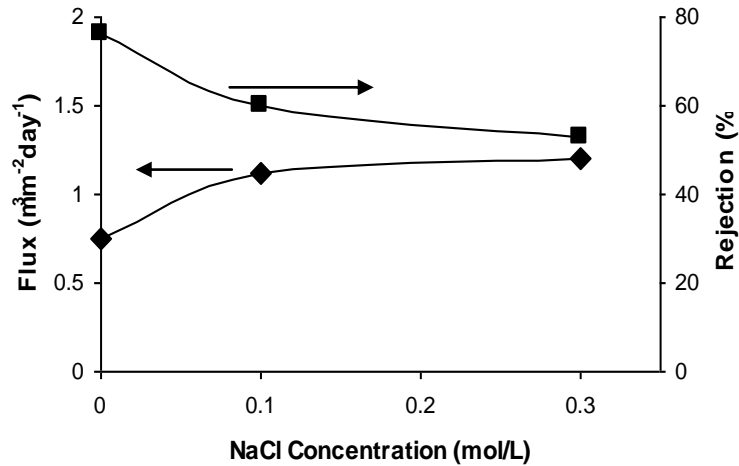


**Figure 3.13 Effect of ionic strength on PEM performance**

### 3.3.3.3 Effect of PEI $M_w$

Figure 3.14 shows the effect of  $M_w$  of PEI. From low  $M_w$  PEI, the salt rejection reaches a plateau, about 61% after 3.5 bilayers as shown in Figure 3.14(a). In Figure 3.14(b), although the flux of the PEM from low  $M_w$  PEI decreases with the increase of deposited layers as that from branched high  $M_w$  PEI, there is no salt rejection. Besides, the decrease of the flux after the deposition of the first layer of branched high  $M_w$  PEI in

Figure 3.14(a) is much more obvious than that in Figure 3.14(b). In addition, the flux of the PEM from branched high  $M_w$  PEI is much smaller than the PEM from low  $M_w$  PEI with corresponding layer number. The molecular weight of the polyelectrolytes, i.e. the chain length, has an important effect on the membrane performance. At the beginning of the deposition of PEMs, polyelectrolytes might adsorb on the substrate surface as isolated “islands”. These islands would be connected during the following adsorption steps [67]. High  $M_w$  PEI will have a better bridging capability than low  $M_w$  PEI. Therefore, the better salt rejection would then appear earlier with a lower number of bilayers for high  $M_w$  PEI. While for low  $M_w$  PEI, a larger number of bilayers is required to observe the salt rejection. It is also reasonable to deduce that the PEM from low  $M_w$  PEI would have a looser structure, which also results in the low salt rejection and high flux.

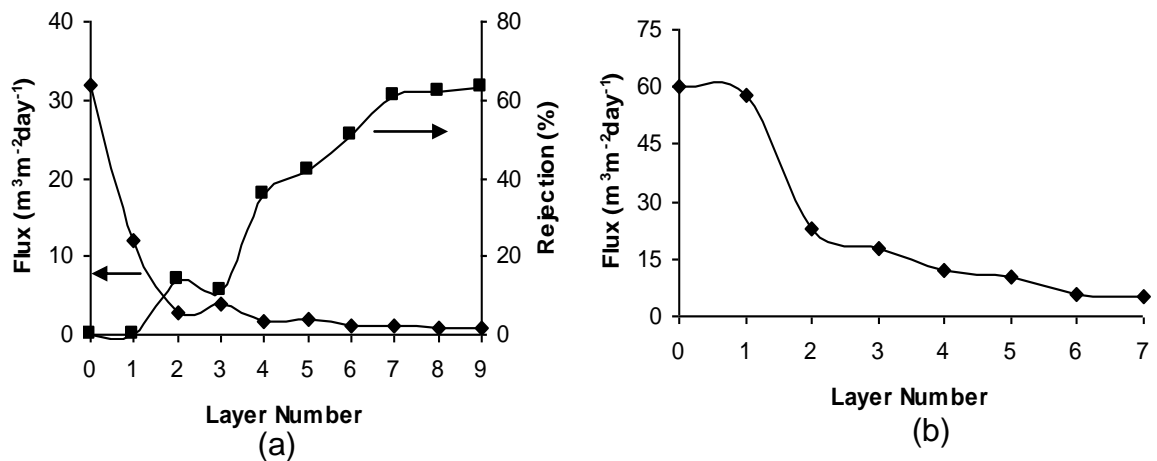


**Figure 3.14 Performance of PEMs from (a) branched PEI ( $M_w=25,000$ ) and (b) low  $M_w$  PEI ( $M_w=800$ ) with sPEEK in water.**

#### 3.3.3.4 Effect of sulfonation degree of sPEEKs

sPEEKs with different degrees of sulfonation were used to prepare PEMs with branched PEI in water. The performance is listed in Table 3.3. According to the different



IECs, sample A can be dissolved in NMP not in methanol, sample B in methanol not in water, and sample C in water. The highest rejection was observed for sample B. But the optimum performance was from sample C. PEM from sample A had the lowest salt rejection. The reason might be due to the lower density of ionic bonds formed within the PEM, i.e. the lowest interaction between sPEEK and PEI, because of the relatively low IEC of sample A. In addition, the solvent plays an important role in the deposition of PEM films [68]. In methanol, significant ionic dissociation occurs and results in a classical polyelectrolyte-like behavior, which means that polyelectrolytes behave in methanol as in water. On the other hand, when we prepared PEM membranes from the deposition solutions, i.e. sample B in methanol and branched PEI in water, the deposited sPEEK layers did not dissolve back in water during the deposition of PEI layers from water due to the insolubility of sample B in water. Therefore, the amount of sPEEK in every bilayer would be higher than that in the PEMs from sample A, which resulted in higher salt rejection and lower flux. The insolubility of sample B will also make the PEM swell less in water and lead to a higher salt rejection. Furthermore, the PEM films from sample B would be expected to be more stable in water than the films from sample A.

**Table 3.3 Performance of PEMs from sPEEK with different sulfonation**

sPEEK	A	B	C
IEC (mmol/g)	1.60	1.93	2.40
Salt rejection (%)	6	80	76
Flux ( $\text{m}^3 \text{m}^{-2} \text{day}^{-1}$ )	3.00	0.30	0.75

#### 3.3.3.5 Performance of PEMs based on different PAN substrate membranes

We also studied the effect of different PAN substrates on the membrane performance. From the company, Sepro Membranes, we obtained PAN UF membranes

with different water flux and pore size as shown in Table 3.4. All these PAN UF membranes were hydrolyzed in 1 M NaOH at room temperature for 24 hours before the deposition of PEMs. On these hydrolyzed PAN UF membranes, PEMs with 3-bilayers were formed from 0.1 M sPEEK in methanol and 0.1 M branched PEI in water under a pressure of 13.79 bars. The performance of the PEMs is listed in Table 3.5. The best performance, i.e. highest flux and salt rejection, was found when PAN 200 was used as a substrate. It demonstrated that there was an optimum pore size of the substrate membranes. It seems reasonable that, when the pore is too small, the substrate will become the bottleneck and result in a lower flux. But why did the larger pore result in a low flux, i.e. PEMs based on PAN 400 have a lower flux than those based on PAN 200? The possible explanation might be related to the attachment of polyelectrolytes (sPEEK and PEI) onto the pore wall in PAN substrates. When the pore is small, the pore will be filled by polyelectrolytes very quickly, e.g. the deposition of the first bilayer, and thicker layers of PEMs can form on top of pores during the following deposition steps, e.g. the deposition of the second and third bilayer. When the pore becomes larger, the pore might be filled until the deposition of the second bilayer, thus only the third bilayer on the top of pores, which results in thinner layers of PEMs and high flux. When the PEMs on the top of pores are thin enough, then the PAN substrate substitutes for the thickness of the PEMs as the flux-determining factor. On the other hand, when pores are filled, they would have some unfilled spaces smaller than the size of one polyelectrolyte molecule. These spaces determine the flux of the substrate membranes. The unfilled spaces in PAN 200 are larger than those in PAN 400, hence resulting in a higher flux. Now we have to explain the change of salt rejections among different PAN substrates. As we known, salt

rejections are usually determined by the thin-skin layer in a composite membrane. For PAN 10, the thicker layers of PEMs on top of pores resulted in a high salt rejection. For PAN 50, PAN 200 and PAN 400, the layers on top of pores might have similar thickness and thus similar salt rejection capability. Therefore, the difference in salt rejection would mainly result from the PEMs formed in nanopores of PAN substrate membranes. Inside nanopores, the formation of PEMs is totally different with the formation of PEMs on a flat substrate. For example, the thickness of one bilayer of PEMs in nanopores (with a diameter of several hundred nanometers) would be much larger, sometimes up to one order magnitude larger than that of PEMs on a smooth substrate where one bilayer has a thickness of a few nanometers. The structure of PEMs inside nanopores needs to be further addressed [69]. The relative high salt rejection and flux of our membranes should be directly related to the formation and structure of PEMs formed inside nanopores. For PAN 200, we assumed that the thickness or outer layer charges of PEMs inside nanopores happened to be the optimum to achieve a larger salt rejection. For PAN 50 and PAN 400, the unfilled spaces are possibly so small that the outer layers are not obvious. The whole PEMs could be considered as inner layers where net charges are negligible and thus no Donnan exclusion effects, which cause the lower salt rejection than that of PAN 200. It would be very interesting to explore the reason behind that. However, at least we learned that, by using PAN 200 as a substrate membrane, we could develop PEMs with an optimum performance.

**Table 3.4 Properties of different PAN UF membranes**

MODEL NUMBER	WATER FLUX (Lmh/bar)	MW of MARKER (Dalton)	MARKER REJECTION (%)
PAN10	70	20K PEG	95
PAN50	140	20K PEG	90
PAN200	300	20K PEG	85
PAN400	600	20K PEG	75

Notes: PEG-Poly (ethylene glycol)

**Table 3.5 Performance of PEMs with various PAN substrates**

PAN Substrates	PAN10	PAN50	PAN200	PAN400
Salt rejection (%)	73	68	79	75
Flux ( $\text{m}^3 \text{m}^{-2} \text{day}^{-1}$ )	0.33	0.51	0.60	0.53

### 3.3.3.6 Effects of the number of bilayers of PEMs

PAN 200 was used as an optimum substrate to study the effects of the number of bilayers on the performance of PEMs. The result is shown in Table 3.6. At the beginning of the deposition, the salt rejection increased sharply. As the number of bilayers increased, the salt rejection reached values of 89 percent. After three bilayers, the salt rejection only increased modestly. When we coated eight bilayers, the salt rejection even had a little drop. This observation might be again related to the PEMs forming inside nanopores. Before three bilayers, PEMs continued forming within nanopores. These PEMs would have an orientation perpendicular to the surface of substrate membranes, which would be helpful to achieve high salt rejection. After that the PEMs mainly formed on the top of the surface, thus the salt rejection increased slowly. When the deposition progressed further, the charge of the outlayer of PEMs might decrease due to the counterbalance of so many inner bilayers. The Donnan exclusion effects to NaCl would

therefore reduce and salt rejection decreased, even though the number of bilayers increased.

**Table 3.6 Performance of PEMs with various number of bilayers**

The number of bilayers	1	3	5	8
Salt rejection (%)	45	79	89	87
Flux ( $\text{m}^3\text{m}^{-2}\text{day}^{-1}$ )	1.12	0.60	0.27	0.16

In addition, two highly successful commercial membranes were tested at the same operating condition as a comparison. One is the NTR 7450, a nanofiltration membrane, which had a 65 % salt rejection with a flux of  $1.25 \text{ m}^3\text{m}^{-2}\text{day}^{-1}$ . The other is the SWC-4, a polyamide RO membrane, which had a 96% salt rejection with a flux of  $0.28 \text{ m}^3\text{m}^{-2}\text{day}^{-1}$ . Both membranes have been used for at least one decade. Therefore, our system appears promising for nanofiltration application. For reverse osmosis, salt rejection requires further improvement for commercialization. After further tuning various parameters such as the hydrolysis degree and porosity of PAN substrates, the properties of sPEEK including  $M_w$  and sulfonation distribution, etc, we believe that membranes with improved performance over commercial membranes can be prepared. In addition, by controlling the number of bilayers, a series of membranes for different applications can be prepared.

#### *3.3.3.7 Antifouling property of PEMs in comparison with NTR 7450*

We have compared the antifouling property of our PEMs with NTR 7450 because both membranes have a sulfonated polymer surface. The fouling behavior was investigated by employing bovine serum albumin, humic acid, and sodium alginate as representatives of the three important classes of biomolecule foulants: proteins, NOM and polysaccharides, respectively. Preliminary results showed antifouling property of our

membranes is comparable with the commercial membranes.

Figure 3.15 showed the dead-end filtration results for a BSA in a PBS solution plotted as a function of normalized flux (flux/initial flux) versus time. The flux of NTR 7450 showed a small decline over the course of the filtration, while our membrane displayed almost a constant performance. The better antifouling property might be facilitated by the hydrophilic ionic crosslinks in PEMs. Membrane susceptibility to fouling by humic acid (HA) was also investigated, as shown in Figure 3.16. At the beginning, there was little change for our membrane. As the filtration progressed, humic acid was observed to precipitate from solution, probably aided by the high concentration of  $\text{Ca}^{2+}$  in the solution. It aggregated in the center of the membrane due to the concentration polarization from the inefficient stirring of the filtration cell, which caused a decreasing flux. A similar occurrence was observed for NTR 7450, where the flux decreased more quickly. In Figure 3.17, the observed flux decline for both membranes was more dramatic. But our membranes still had better performance. One reason leading to the dramatic drop might be hydrogen bonds between sodium alginate and sulfonated polymers. The other reason was the concentration polarization where we observed much more precipitate on the membrane surface.

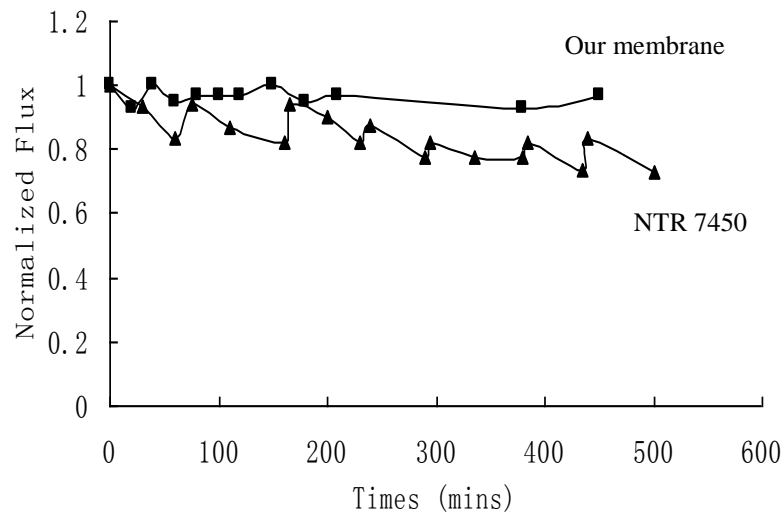


**Figure 3.15 Dead-end filtration of model protein solution (bovine serum albumin, 1.0g/L, 13.79 bars) with our membrane (3bilayers on PAN200 hydrolyzed 24hours) and NTR7450**

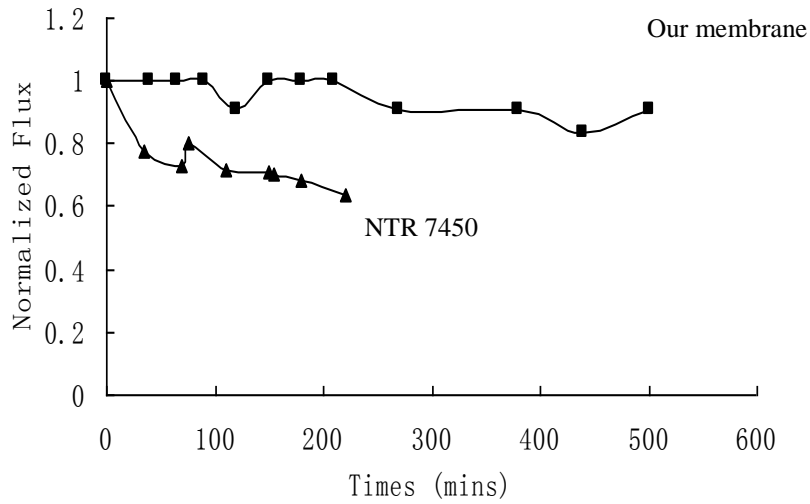


**Figure 3.16 Dead-end filtration of model NOM solution (humic acid 1.0g/L, 1mM CaCl<sub>2</sub>, 13.79 bars) with our membrane (3bilayers on PAN200 hydrolyzed 24hours) and NTR7450**

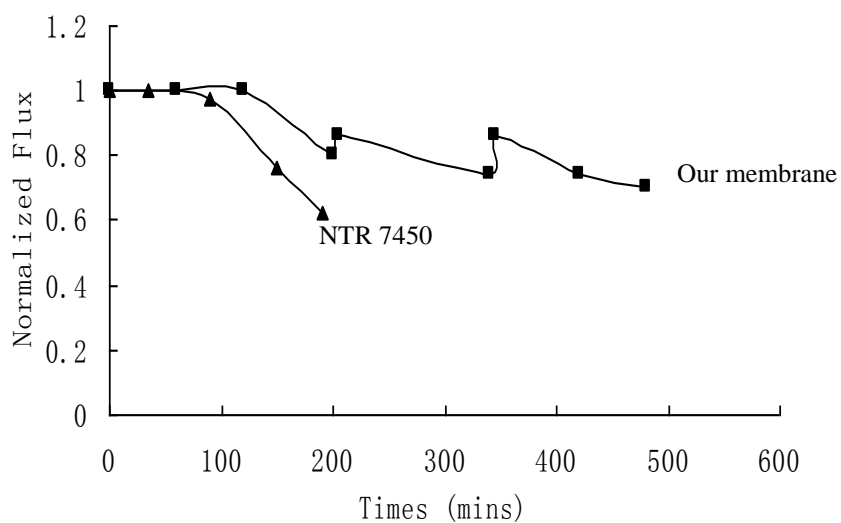


**Figure 3.17 Dead-end filtration of model polysaccharide solution (sodium alginate, 1.0g/L, 13.79 bars) with our membrane (3bilayers on PAN200 hydrolyzed 24hours) and NTR7450**

### 3.3.3.8 Characterization of PEMs

The ATR/FTIR spectra in Figure 3.18 demonstrated the transformation of membranes during the deposition of PEMs. After deposition of the first PEI layer, there appeared a peak at  $1565\text{ cm}^{-1}$  in Figure 3.18(b), which corresponded to the carbonyl stretching vibration in  $-\text{COO}^-\text{H}_3\text{N}^+$  ionic bonds. The OH and NH peak around  $3300\text{ cm}^{-1}$  also increased and shifted to the lower wavenumber region due to the NH groups in the PEI. When sPEEK was coated, the spectrum, i.e. Figure 3.18(c), showed some similar peaks as in Figure 3.18(d) where pure sPEEK membrane spectrum was shown. The peak around  $3300\text{ cm}^{-1}$  shifted back to the higher wavenumber region because of the contribution of OH groups in sPEEK.



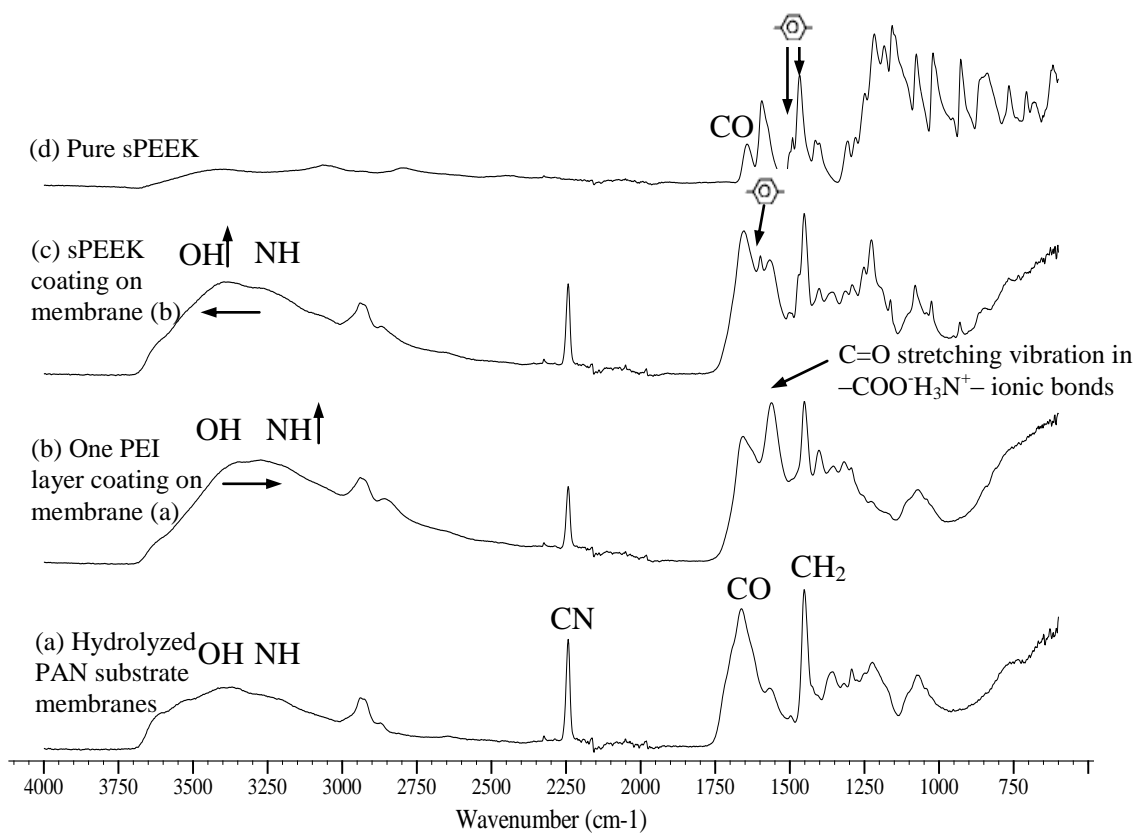


**Figure 3.18 ATR-FTIR spectra of the deposition of PEM membranes**

The change of the membrane surface morphology was illustrated clearly by SEM. Originally; the hydrolyzed PAN substrate has a highly porous surface. When the first layer of PEI was deposited on the hydrolyzed PAN substrate membrane, most pores were covered by PEI but still could be vaguely seen in Figure 3.19(b). After coated with PEI and sPEEK, no pores could be observed, as shown in Figure 3.19(c).

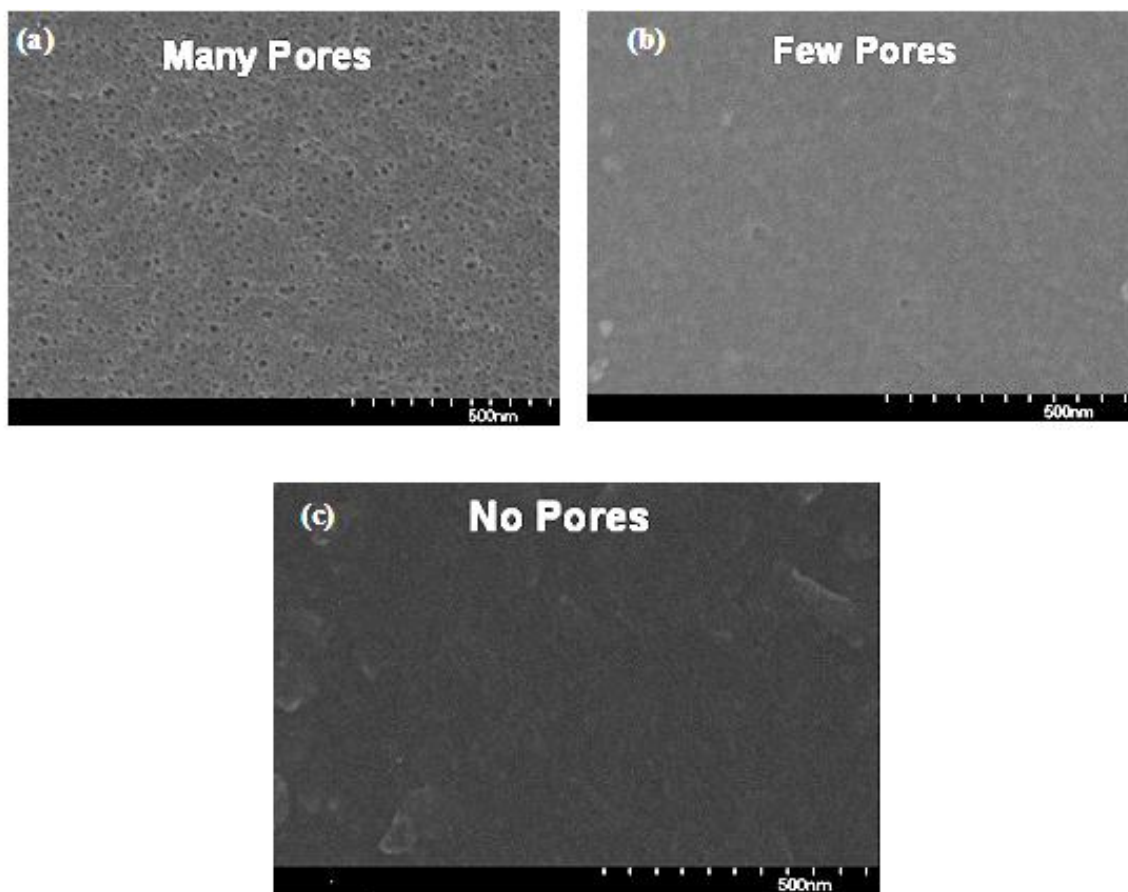


**Figure 3.19 SEM micrographs of the transformation of PEM membrane surfaces during deposition (a) hydrolyzed PAN substrate membrane, (b) hydrolyzed PAN membrane deposited with one layer PEI, and (c) hydrolyzed PAN membrane deposited with PEI and sPEEK**

### 3.3.4 Conclusions

Preparation of new polyelectrolyte multilayers (PEMs) as selective skins in composite membranes for nanofiltration was carried out by alternating layer-by-layer deposition of sPEEK and PEI. The supporting PAN substrate membrane was obtained by a phase separation process followed by hydrolysis in 1M NaOH. It was demonstrated that the use of pressure during the electrostatic self-assembly could increase the NaCl rejection of the PEMs from 30% to 76% at a feed concentration of 2g/L under 13.79 bar. The number of bilayers coated was only 3.5 with PEI on both top and bottom. The effect

of degree of sulfonation on sPEEK was also studied. By depositing the sPEEK dissolved in methanol and branched PEI dissolved in water on suitable substrate membranes, the rejection of the PEMs could be further increased up to 89%. In comparison with NTR 7450, the PEMs also exhibited excellent fouling resistance for a variety of model biofoulant solutions. The process and/or the composition we developed will be a promising competitor of current highly successful commercial membranes for nanofiltration or reverse osmosis.

### 3.4 References

- [1] “Water for People, Water for Life”, *United Nations World Water Development Report*, 2003.
- [2] S. Loeb, S. Sourirajan, Sea water demineralization by means of an osmotic membrane, in *Saline Water Conversion II*, R.F. Gould (ed.), *Advances in Chemistry Series Number 38*, American Chemical Society, Washington, DC, (1963) 117-132.
- [3] R.W. Baker, *Membrane Technology and Applications*, John Wiley & Sons, Ltd., 2004.
- [4] H.S. Alkhatim, M.I. Alcaina, E. Soriano, M.I. Iborra, J. Lora, J. Arnal, Treatment of whey effluents from dairy industries by nanofiltration membranes, *Desalination* 119 (1998) 177-184.
- [5] J. Sojka-Ledakowicz, T. Koprowski, W. Machnowski, H. H. Knudsen, Membrane filtration of textile dyehouse wastewater for technological water reuse, *Desalination* 119 (1998) 1-10.
- [6] K.-H. Ahn, H.-Y. Cha, I.-T. Yeom, K.-G. Song, Application of nanofiltration for recycling of paper regeneration wastewater and characterization of filtration resistance, *Desalination* 119 (1998) 169-176.
- [7] M.-B. Hagg, Membranes in chemical processing. A review of applications and novel developments, *Sep. Purif. Methods* 27 (1998) 51-168.
- [8] J. Schaep, B. Van der Bruggen, S. Uytterhoeven, R. Croux, C. Vandecasteele, D. Wilms, E. Van Houtte, F. Vanlerberghe, Removal of hardness from groundwater by

- nanofiltration, *Desalination* 119 (1998) 295-302.
- [9] R.J. Petersen, Composite reverse osmosis and nanofiltration membranes, *J. Membr. Sci.* 1993, 83, 81.
- [10] J.E. Cadotte, Evaluation of composite reverse osmosis membrane, in *Materials Science of Synthetic Membranes*, D.R.Lloyd (ed.), ACS Symposium Series Number 269, American Chemical Society, Washington, DC, (1985)
- [11] R.E. Larson, J.E. Cadotte, R.J. Petersen, The FT-30 seawater reverse osmosis membrane-element test results, *Desalination* 38 (1981) 473-483.
- [12] J.E. Cadotte, Interfacially synthesized reverse osmosis membrane, US Patents 4277344, 1981.
- [13] M. Kurihara, N. Harumiya, N. Kannamaru, T. Tonomura, M. Nakasatomi, Development of the PEC-1000 composite membrane for single stage sea water desalination and the concentration of dilute aqueous solutions containing valuable materials, *Desalination* 38 (1981) 449-460.
- [14] A.K. Ghosh, V. Ramachandhran, M.S. Hanra, B.M. Misra, Synthesis, characterization, and performance of sulfonated polyethersulfone nanofiltration membranes, *J. Macromol. Sci. Pure Appl. Chem.* A39 (3) (2002) 199.
- [15] F. G. Donnan, Theory of membrane equilibria and membrane potentials in the presence of non-dialysing electrolytes. A contribution to physical-chemical physiology, *J. Membr. Sci.* 100 (1995) 45-55.
- [16] J. R. Bontha, P. N. Pintauro, Water orientation and ion solvation effects during multicomponent salt partitioning in a nafion cation exchange membrane, *Chem. Eng. Sci.* 49 (1994) 3835-3851.
- [17] E. Glueckauf, The distribution of electrolytes between cellulose acetate membranes and aqueous solutions, *Desalination* 18 (1976) 155-172.
- [18] M.H.V. Mulder, Basic Principles of Membrane Technology, Kluwer, London, 1996.
- [19] J. Smid, J.H.M. Albers, A.P.M. Kusters, The formation of asymmetric hollow fiber membranes for gas separation, using PPE of different intrinsic viscosities, *J. Membr. Sci.* 64 (1991) 121.
- [20] C. Wu, S. Zhang, D. Yang, J. Wei, C. Yan, X. Jian, Preparation, characterization and application in wastewater treatment of a novel thermal stable composite membrane, *J. Membr. Sci.* 279 (2006) 238-245.

- [21] P.S. Singh, S.V. Joshi, J.J. Trivedi, C.V. Devmurari, A.P. Rao, P.K. Ghosh, Probing the structural variations of thin film composite RO membranes obtained by coating polyamide over polysulfone membranes of different pore dimensions, *J. Membr. Sci.* 278 (2006) 19–25.
- [22] N.-W. Oh, J. Jegal, K.-H. Lee, Preparation and Characterization of nanofiltration composite membranes using polyacrylonitrile (PAN). II. preparation and characterization of polyamide composite membranes, *J. Appl. Polym. Sci.* 80 (2001) 2729-2736.
- [23] M. Hirose, H. Ito, Y. Kamiyama, Effect of skin layer surface structures on the flux behaviour of RO membranes, *J. Membr. Sci.* 121 (1996) 209-215.
- [24] T.-S. Chung, L. Shao, P.S. Tin, Surface modification of polyimide membranes by diamines for H<sub>2</sub> and CO<sub>2</sub> separation, *Macromol. Rapid Commun.* 27 (2006) 998.
- [25] K. Fujimoto, Y. Takebayashi, H. Inoue, Y. Ikada, Ozone-induced graft polymerization onto polymer surface, *J Polym Sci Part A: Polym Chem* 31 (1993) 1035.
- [26] R.A. Hayes, Polyimide gas separation membranes, US Patent 4717393, 1988.
- [27] N. Hilal, O.O. Ogunbiyi, N.J. Miles, R. Nigmatullin, Methods employed for control of fouling in MF and UF membranes: a comprehensive review, *Sep. Sci. Technol.* 40 (2005) 1957–2005.
- [28] W. Shan, P. Bacchin, P. Aimar, M.L. Bruening, V.V. Tarabara, Polyelectrolyte multilayer films as backflushable nanofiltration membranes with tunable hydrophilicity and surface charge, *J. Membr. Sci.* (2009), doi:10.1016/j.memsci.2009.11.059.
- [29] J. Wang, Y. Yao, Z. Yue, J. Economy, Preparation of polyelectrolyte multilayer films consisting of sulfonated poly(ether ether ketone) alternating with selected anionic layers, *J. Membr. Sci.* 337 (2009) 200–207.
- [30] C. Ba, D.A. Ladner, J. Economy, Using polyelectrolyte coatings to improve fouling resistance of a positively charged nanofiltration membrane, *J. Membr. Sci.* 347 (2010) 250–259.
- [31] S.H. Kim, S.-Y. Kwak, T. Suzuki, Positron annihilation spectroscopic evidence to demonstrate the flux-enhancement mechanism in morphology-controlled thin-film-composite (TFC) membrane, *Environ. Sci. Technol.* 39 (2005) 1764.
- [32] J. Glater, S. Hong, M. Elimelech, The search for a chlorine-resistant reverse osmosis membrane, *Desalination* 95 (1994) 325-345.

- [33] M.J.H. Snow, D. de Winter, R. Buckingham, J. Campbell, J. Wagner, New techniques for extreme conditions: high temperature reverse osmosis and nanofiltration, *Desalination* 105 (1996) 57–61.
- [34] M. Manttari, A. Pihlajamaki, E. Kaipainen, M. Nystrom, Effect of temperature and membrane pre-treatment by pressure on the filtration properties of nanofiltration membranes, *Desalination* 145 (2002) 81–86.
- [35] P. Vandezande, L. Gevers, I. Vankelecom, Solvent resistant nanofiltration: separating on a molecular level, *Chem. Soc. Rev.* 37 (2008) 365-405.
- [36] A.I. Schöer, A.G. Fane, T.D. Waite (Eds.), *Nanofiltration—Principles and Applications*, Elsevier Ltd., 2005.
- [37] U. Razdan, S.V. Joshi, V.J. Shah, Novel membrane processes for separation of organics, *Curr. Sci. India* 85 (2003) 761-771.
- [38] E.S. Tarleton, J.P. Robinson, S.J. Smith, J.J.W. Na, New experimental measurements of solvent induced swelling in nanofiltration membranes, *J. Membr. Sci.* 261 (2005) 129-135.
- [39] J.A. Whu, B.C. Baltzis, K.K. Sirkar, Nanofiltration studies of larger organic microsolute in methanol solutions, *J. Membr. Sci.* 170 (2000) 159-172.
- [40] S.S. Han, S.S. Im, J.C. Won, J.H. Lee, K.Y. Choi, Y.S. Kim, Synthesis and characterization of new polyimides containing ethynylene linkages, *Eur. Polym. J.* 43 (2007) 1541-1548.
- [41] Y. Liu, C. Pan, M. Ding, J. Xu, Effects of crosslinking distribution on gas permeability and permselectivity of crosslinked polyimides *Eur. Polym. J.* 35 (1999) 1739-1741.
- [42] Y.H. See Toh, F.W. Lim, A.G. Livingston, Polymeric membranes for nanofiltration in polar aprotic solvents, *J. Membr. Sci.* 301 (2007) 3-10.
- [43] K. Vanherck, A. Cano-Odena, G. Koechelberghs, T. Bedroog, I. Vankelecom, A simplified diamine crosslinking method for PI nanofiltration membranes, *J. Membr. Sci.* 353 (2010) 135-143.
- [44] Y.H. See Toh, X.X. Loh, K. Li, A. Bismarck, A.G. Livingston, In search of a standard method for the characterization of organic solvent nanofiltration membrane, *J. Membr. Sci.* 291 (2007) 120-125.
- [45] X.J. Yang, A.G. Livingston, L. Freitas dos Santos, Experimental observations of nanofiltration with organic solvent, *J. Membr. Sci.* 190 (2001) 45-55.

- [46] T. Shintani, H. Matsuyama, N. Kurata, Effect of heat treatment on performance of chlorine-resistant polyamide reverse osmosis membranes, *Desalination* 249 (2009) 370-377.
- [47] J.M.M. Peeters, J.P. Boom, M.H.V. Mulder, H. Strathmann, Retention measurements of nanofiltration membranes with electrolyte solutions, *J. Membr. Sci.* 145 (1998) 199-209.
- [48] X. Qiao, T.-S. Chung, Diamine modification of P84 polyimide membranes for pervaporation dehydration of isopropanol, *AIChE* 52 (2006) 3462-3472.
- [49] B. Van der Bruggen, J. Schaep, D. Wilms, C. Vandecasteele, Influence of molecular size, polarity and charge on the retention of organic molecules by nanofiltration, *J. Membr. Sci.* 156 (1999) 29-41.
- [50] Y.H. See-Toh, F.C. Ferreira, A.G. Livingston, The influence of membrane formation parameters on the functional performance of organic solvent nanofiltration membranes, *J. Membr. Sci.* 299 (2007) 236-250.
- [51] R.K. Iler, Multilayers of colloidal particles, *J. Colloid Interface Sci.* 21 (1966) 569-594.
- [52] G. Decher, J. D. Hong, Buildup of ultrathin multilayer films by a self-assembly process. 1. Consecutive adsorption of anionic and cationic bipolar amphiphiles on charged surfaces, *Makromolekulare Chemie, Macromolecular Symposia* 46 (1991) 321-327.
- [53] G. Decher, J. D. Hong, Buildup of ultrathin multilayer films by a self-assembly process: II. Consecutive adsorption of anionic and cationic bipolar amphiphiles and polyelectrolytes on charged surfaces, *Berichte der Bunsen-Gesellschaft* 95 (1991) 1430-1434.
- [54] S. K. Tripathy, J. Kumar, H. S. Nalwa, Handbook of Polyelectrolytes and Their Applications, American Scientific Publishers, 2002.
- [55] O. A Evers, G. J. Fleer, J. M. H. M. Scheutjens, J. Lyklema, Adsorption of weak polyelectrolytes from aqueous solution, *J. Colloid Interface Sci.* 111 (1986) 446-454.
- [56] M. A. Cohen Stuart, G. J. Fleer, J. Lyklema, W. Norde and J. M. H. M. Scheutjens, Adsorption of ions, polyelectrolytes and proteins, *Adv. Colloid Interface Sci.* 34 (1991) 477-535.
- [57] H. G. M. Van de Steeg, M. A. Cohen Stuart, A. De Keizer, B. H. Bijsterbosch, Polyelectrolyte adsorption: a subtle balance of forces, *Langmuir* 8 (1992) 2538-2546.

- [58] P. Bertrand, A. Jonas, A. Laschewsky, R. Legras, Ultrathin polymer coatings by complexation of polyelectrolytes at interfaces: suitable materials, structure and properties, *Macromol. Rapid Commun.* 21 (2000) 319-348.
- [59] A.S. Michaels, H.J. Bixler, R. W. Hausslein and S. M. Fleming, Polyelectrolyte complexes as reverse osmosis and ion-selective membranes, *Research and Development Progress Report for Office of Saline Water*, US Department of the Interior, 149 (1965).
- [60] B. W. Stanton, J. J. Harris, M. D. Miller, M. L. Bruening, Ultrathin, multilayered polyelectrolyte films as nanofiltration membranes, *Langmuir* 19 (2003) 7038-7042.
- [61] M. D. Miller, M. L. Bruening, Controlling the nanofiltration properties of multilayer polyelectrolyte membranes through variation of film composition", *Langmuir* 20 (2004) 11545-11551.
- [62] W. Jin, A. Toutianoush, B. Tieke, Use of polyelectrolyte layer-by-layer assemblies as nanofiltration and reverse osmosis membranes, *Langmuir* 19 (2003) 2550-2553.
- [63] W. Cui, J. A. Kerres, G. Eigenberger, Development and characterization of ion exchange polymer blend membranes, *Sep. Purif. Tech.* 14 (1998) 145-154.
- [64] C. Bailly, D. J. Williams, F. E. Karasz, W. J. MacKnight, The sodium salts of sulphonated poly (aryl-ether-ether-ketone)(PEEK): preparation and characterization, *Polymer* 28 (1987) 1009-1016.
- [65] A. Asatekin, A. Menniti, S. Kang, M. Elimelech, E. Morgenroth, A. M. Mayes, Antifouling nanofiltration membranes for membrane bioreactors from self-assembling graft copolymers, *J. Membr. Sci.* 285 (2006) 81-89.
- [66] H. G. M. van de Steeg, M. A. Cohen Stuart, A. de Keizer, B. H. Bijsterbosch, Polyelectrolyte adsorption: a subtle balance of forces, *Langmuir* 8 (1992) 2538-2546.
- [67] W. Lenk, J. Meier-Haack, Polyelectrolyte multilayer membranes for pervaporation separation of aqueous-organic mixtures, *Desalination* 148 (2002) 11-16.
- [68] S. Jousset, H. Bellissent, J. C. Galin, Polyelectrolytes of high charge density in organic solvents. synthesis and viscosimetric behavior, *Macromolecules* 31 (1998) 4520-4530.
- [69] M. Steinhart, Supramolecular organization of polymeric materials in nanoporous hard templates, *Advances in Polymer Science*, 2008.



## CHAPTER 4

### CONCLUSIONS

This research has led to the generation of a broad knowledge base relating to the use of chemically activated carbon fibers for mercury removal and nanofiltration membranes for water purification. The following text enumerates the significant findings of this work.

- We have successfully prepared activated carbon fibers (ACFs) on a glass fabric substrate, the main component of a fabric filter system. This combined system may adsorb Hg and fly ash simultaneously while still remaining competitive cost and the quality of fly ash.
- We have developed various chemical treatments of ACFs including sulfur impregnation, chloride impregnation and bromination. These moieties show strong affinity to elemental mercury, facilitate interactions between carbon matrix with mercury and hence improve mercury removal efficiency.
- Besides the effects of chemical structure, pore properties associated with adsorbents also play an important role on mercury adsorption. Micropores are mainly responsible for mercury adsorption while mesopores act as transport routes.
- We have successfully crosslinked P84 copolyimide asymmetric membranes using branched polyethylenimine (PEI) at different reaction temperatures. The resultant membranes have a positively charged surface and a crosslinked structure. The membranes prepared at 70°C show over 90% rejection for solutes with a molecular weight higher than 226 g/mol, especially the positively charged solutes.

Additionally, the crosslinked structure make membranes stable even in harsh aprotic solvent such as dimethyl formamide (DMF).

- We have prepared polyelectrolyte multilayer (PEM) films consisting of sulfonated poly (ether ether ketone) (sPEEK) alternating with polyethyleneimine (PEI) on polyacrylonitrile (PAN) substrate for fouling resistant properties. Two novel variables are introduced in our approach, a) the use of pressure and b) organic solvents, during the alternating physisorption of oppositely charged polyelectrolytes on porous supports through the electrostatic self-assembly. It is shown that the use of pressure could increase the salt rejection of the PEMs by one to two times. The rejection of the PEMs can be further improved by using methanol as the dip solution and the optimized rejection could reach as high as 89%. The PEMs also had a better antifouling property in comparison with NTR 7450, a commercial NF membrane with a sulfonated surface.